Imperial College London

Department of Physics

New Frequencies and Geometries for Plasmonics and Metamaterials

A thesis submitted in partial fulfillment for the degree of Doctor of Philosophy

Author:
Yan Francescato

Supervisor:
Prof. Stefan A. Maier

July 28, 2014

Declaration of Authorship

I, Yan Francescato, declare that this thesis titled 'New Frequencies and Geometries for Plasmonics and Metamaterials' and the work presented in it are my own. I confirm that:

- This work was done wholly or mainly while in candidature for a research degree at this University.

- Where any part of this thesis has previously been submitted for a degree or any other qualification at this University or any other institution, this has been clearly stated.

- Where I have consulted the published work of others, this is always clearly attributed.

- Where I have quoted from the work of others, the source is always given. With the exception of such quotations, this thesis is entirely my own work.

- I have acknowledged all main sources of help.

- Where the thesis is based on work done by myself jointly with others, I have made clear exactly what was done by others and what I have contributed myself.

Contributions

Publications

- K. Hur, **Y. Francescato**, V. Giannini, S. A. Maier, R. G. Hennig, and U. Wiesner. Three-dimensionally isotropic negative refractive index materials from block copolymer self-assembled chiral gyroid networks. *Angewandte Chemie International Edition*, 50(50):11985–11989, 2011.
- V. Giannini, **Y. Francescato**, H. Amrania, C. C. Phillips, and S. A. Maier. Fano resonances in nanoscale plasmonic systems: A parameter-free modeling approach. *Nano Letters*, 11(7):2835–2840, Jul 2011.
- R. Rehammar, **Y. Francescato**, A. I. Fernández-Domínguez, S. A. Maier, J. M. Kinaret, and E. E. B. Campbell. Diffraction from carbon nanofiber arrays. *Optics Letters*, 37(1):100–102, Jan 1 2012.
- **Y. Francescato**, V. Giannini, and S. A. Maier. Plasmonic systems unveiled by fano resonances. *ACS Nano*, 6(2):1830–1838, 2012.
- Y. Xiao, **Y. Francescato**, V. Giannini, M. Rahmani, T. R. Roschuk, A. M. Gilbertson, Y. Sonnefraud, C. Mattevi, M. Hong, L. F. Cohen, and S. A. Maier. Probing the dielectric response of graphene via dual-band plasmonic nanoresonators. *Physical Chemistry Chemical Physics*, 15(15):5395–5399, 2013.
- **Y. Francescato**, V. Giannini, and S. A. Maier. Strongly confined gap plasmon modes in graphene sandwiches and graphene-on-silicon. *New Journal of Physics*, 15, Jun 14 2013.
- J. D. Caldwell, O. J. Glembocki, **Y. Francescato**, N. Sharac, V. Giannini, F. J. Bezares, J. P. Long, J. C. Owrutsky, I. Vurgaftman, J. G. Tischler, V. D. Wheeler, N. D. Bassim, L. M. Shirey, R. Kasica, and S. A. Maier. Low-Loss, Extreme Subdiffraction Photon Confinement via Silicon Carbide Localized Surface Phonon Polariton Resonators. *Nano Letters*, 13(8):3690–3697, Aug 2013.
- M. Rahmani, A. E. Miroshnichenko, D. Y. Lei, B. Luk'yanchuk, M. I. Tribelsky, A. I. Kuznetsov, Y. S. Kivshar, **Y. Francescato**, V. Giannini, M. Hong, and S. A. Maier. Beyond the hybridization effects in plasmonic nanoclusters: Diffraction-induced enhanced absorption and scattering. *Small*, pages n/a–n/a, 2013.

Conferences

- Nanophotonics summer school, Erice (IT): Strongly Confined Gap Modes in Graphene Sandwiches and Graphene-on-Silicon, poster, July 2013.
- Imperial College Postgraduate Symposium, London (UK): New Frequencies and Geometries for Plasmonics and Metamaterials, talk, June 2013.
- Graphene Nanophotonics conference, Benasque (SP): Strongly Confined Gap Modes in Graphene Sandwiches and Graphene-on-Silicon, talk, March 2013.
- National Physics Laboratory (NPL) Graphene conference, Teddington (UK): Graphene Sensing with IR Plasmonics, talk, October 2012.
- Near Field Optics (NFO) conference, San Sebastian (SP): Graphene Sensing with IR Plasmonics, poster, September 2012.
- Imperial College Postgraduate Symposium, London (UK): New Frequencies and Geometries for Plasmonics and Metamaterials, poster, June 2012. **Prize for best poster.**
- European-Materials Reasearch Society (E-MRS) conference, Strasbourg (FR): Fano Resonances in Plasmonic Systems, talk, May 2012.
- Institute of Photonics and Electronics (UFE), Prague (CZ): Fano Resonances in Plasmonic Systems, talk, August 2011.
- Swiss Association for Materials Science and Technology (SVMT) Student Day, Fribourg (CH): Mid-IR nanoantennae for SEIRA, talk, March 2011. **Prize for best Master thesis in Materials Science at EPFL.**

Abstract

The manipulation of light at the nanoscale has become a fascinating research field called nanophotonics. It brings together a wide range of topics such as semiconductor quantum dots or molecular optoelectronics and the study of metal optics, or plasmonics, on one hand and the development of finely designed structures with specifically engineered optical properties called metamaterials on the other. As is often the case, it is at the boundary of these two domains that most novel effects can be observed. Plasmonics has for instance enabled the detection of single molecules due to the large field enhancement which exists in the vicinity of nanostructured metals. Thanks to the confinement of electromagnetic waves below the diffraction limit plasmonic systems are also foreseen as ideal conduits connecting electronic and photonic systems. On another hand, when a material is patterned on a scale smaller than the wavelength, its optical properties are reflections of the structure of the patterned material rather than the material itself, a concept known as metamaterial. This has allowed researchers to obtain exotic optical properties such as negative refractive indices and can be implemented in devices acting like invisibility cloaks or perfect lenses. While the prospects for nanophotonics are far-reaching, real-life applications are severely limited by the intrinsic absorption of metals and the current fabrication methods mostly based on electron-beam lithography which is slow and costly.

In this thesis, we investigate these issues by considering the potentials of other polaritonic materials such as semiconductors, silicon carbide and graphene for field confinement applications. This is achieved through the combination of both numerical studies and sample fabrication and testing with the help of international collaborators. Our results show much improvement over the metallic structures typically used, with an operating range covering the near- and mid-infrared as well as the terahertz. The field compression can also be much greater compared to conventional plasmonic materials, with near-field enhancements reaching four orders of magnitude. Furthermore, we analyse theoretically the optical properties of metallic gyroids which are obtained by self-assembly - a promising chemical route for fabricating large-scale 3D structures with molecular sized resolution. These materials exhibit unexpected properties such as negative refraction and could in consequence be used as thin lenses or waveplates. Last, we develop and apply a theoretical formulation of Fano theory for the case of plasmonics. It allows a clear and simple physical understanding of the interference spectra which are commonly encountered in nanooptics.

Acknowledgements

I would like to thank everyone who helped me throughout my time as a PhD student and I apologize in advance for those in this long list who I might forget. First of all, I thank my supervisor Prof. Stefan A. Maier, who gave me the opportunity to participate to fascinating projects with collaborators at the vanguard of the nanophotonic community. He gave me a great freedom over the way I was managing my work and his trust made my experience all the more rewarding. He also supported my attendance to several international conferences which contributed to an overall very positive graduate experience and gave me the amazing opportunity to spend my last six months in a research group in China. To Dr. Vincenzo Giannini I am probably most in debt, as he shared his passion for physics and contaminated me with his intellectual curiosity. The time we spent together along these years, devising on new ideas, deciphering complex results or while discussing my stupid questions, never ceased to be fun and enriching at the same time. I would like to thank all the members of the Plasmonic group at Imperial College who were always very approachable and helpful. In particular, Drs. Antonio Fernández-Domínguez, Yannick Sonnefraud, Tyler Roschuk, Stéphane Kéna-Cohen, Mohsen Rahmani, Adam Gilbertson and Stephen Hanham. My fellow colleagues Binghao Ng, Tarik Abdelmoula, Ned Yoxall, Antonio Lupi, Roberto Fernández Garciá, Kyle McEnery, Giuliana Di Martino and Enrico Massa I must also thank. I owe a double thanks to Binghao who also proof-read some parts of the present thesis.

During my thesis I have been involved in several collaborations and I would like to thank all my collaborators with whom I learned a lot: Dr. Kayhun Hur and 'Cathy' Zihui Li at Cornell University for our work on metallic gyroids; Dr. Robert Rehammar at Chalmers University of Technology for our work on carbon nanofibre photonic crystals; Dr. Karol Miszta at IIT for our work on octapods; Michael Saliba at Oxford University for our work on dye-sensitized solar cells; and finally Drs. Joshua Caldwell, Orest Glembocki and Igor Vurgaftman for our work on SiC and hBN nanopillars.

For the last part of my thesis I was lucky enough to be welcomed by Profs. Ming Huang and Jiaqiang Wang at Yunnan University in Kunming, China. Dr. Jingjing Yang proved there a very helpful and inestimable colleague. In addition, a new PhD student at Imperial College, Yiguo Chen, took the lead of ongoing projects I was involved in and made my leave much easier. Our work together at distance was a great experience and I am much indebted to his reliance and hard work.

I should thank my father for “forcing” me into science as I never regretted this choice and my parents for their support all along my (long) studies. I would not have pursued so far in physics either if I had not mixed with great students and friends at university with whom I shared a common passion for the subject, therefore I am grateful to have known Oggier, Vava, Tamago, Olive, Max and Etiennou during my years at EPFL. Finally, I would like to thank Prof. Anna Fontcuberta i Morral for her supervision and help during my Master thesis in the group of Prof. Stefan A. Maier. Thank you also Prof. Libero Zuppiroli for introducing me to the wonders of light.

For her constant support, boundless (or as close as it can get) patience and for always giving me a good reason to respect decent working hours I would like to conclude by acknowledging the important contribution to this thesis of my wife, Melody, without whom I might have quitted more than once.

This thesis has been funded by the UK Engineering and Physical Sciences Research Council (EPSRC) and the National Science Foundation (NSF).

Contents

List of Figures

Outline of the Thesis

Chapter 1 recalls the electromagnetic theory of light and the origin of the complex refractive index and permittivity which describe the interaction of light with matter. We also derive the Drude-Lorentz model for the case of metals and polar crystals in order to discuss the properties of surface polaritons and their localized counterpart. Next, the theoretical and experimental methods which were used are presented. Finally, the motivation for this work is discussed.

Chapter 2 describes our investigations on alternative materials with plasmonic-like behaviour. We start by reviewing the history and applications of traditional plasmonics. Then we focus on one hand on our work on localized surface plasmons in semiconductor nanocrystals and on another hand on the strongly confined surface phonons found in silicon carbide nanostructures.

Chapter 3 relates our studies on graphene plasmons. After discussing briefly the optical properties of graphene, we introduce our results on the gap modes in graphene ribbon sandwiches. We then devise on a new broadband sensing scheme based on those same modes. In the end, we present an optical method to determine the doping of a graphene sample.

Chapter 4 is concerned with our exploration of self-assembled gyroid metamaterials. Following a brief survey of metamaterials and their applications, we show that metallic double gyroids are promising as a negative refraction medium.

Chapter 5 consists in our recast of Fano theory into a simple analytic formula by considering a Lorentzian lineshape for the modes which are causing the interference. This derivation allowed us to revisit typical problems of nanophotonics such as surface-enhanced spectroscopy, electromagnetically induced transparency, lattice modes and hybridization while providing a complete and clear physical picture of the coupling mechanisms at play.

Chapter 6 gives some general conclusions and prospects on the advances in the fields of plasmonics and metamaterials and summarizes our main results.

1. Introduction

1.1. General Introduction

The field of optics has experienced considerable progress since the revolutionary synthesis of the governing equations of classical electrodynamics by Maxwell more than 150 years ago describing light as an electromagnetic field. The theory of light scattering by small objects as described first by Lord Rayleigh and Mie at the beginning of the 20^{th} century together with the pioneering work in the 50's of Ritchie on thin metal foils led to what is called nowadays as nanophotonics. It refers to the ability of manipulating light at the nanoscale and by extension to control light-matter interactions at those scales. Plasmonics, which is mainly concerned with the nanooptics of metals, has enabled for instance single molecule detection due to the high local fields present in the vicinity of metal nanoparticles and is envisioned as a possible interface between electronics and photonics for information processing. From a completely different perspective, metamaterials, which are man-made materials in which the properties are governed by the structure, are exciting media to create exotic phenomena such as negative refraction. Among the concepts which emerged from the electromagnetic metamaterial community, the most striking ones are probably the perfect lens and the invisibility cloak proposed by Pendry and Leonhardt in the wake of the new millennium.

As we can see, nanophotonics holds a lot of promises but unfortunately its advances are hampered by the significant losses of the constituting materials as well as the limited range of innovative structures accessible by current nanofabrication technologies. In this thesis, we report on our investigations of alternative materials for applications in plasmonics and metamaterials. In particular, we consider geometries obtained by self-assembly as an alternative route to lithography-prepared nanostructures. Our initial theoretical results suggest exciting opportunities bringing nanophotonics closer to commercial applications. Complimentary to this approach, we have studied both experimentally and theoretically the use of polaritonic materials other than metals to achieve strong field localization and guiding for molecular sensing and nanocircuitry with comparable or improved performances at lower frequencies. Finally, due to the presence of multiple resonances in sub-wavelength structures, complex lineshapes are commonly observed in nanophotonics. We studied those in details by applying our analytical development of Fano theory.

In this introductory chapter we provide an overview of the theoretical description of the interaction of light with matter. Starting from Maxwell's equations, we describe the origin and effect of the permittivity of materials on electromagnetic radiation. We then derive the conditions for the existence of surface polaritons and give an account of their most important properties. Next, we describe briefly the working

principle of the finite-difference time domain and finite-element numerical methods from which most results presented in what follows were obtained. The main experimental techniques used to characterize the samples (Fourier-transform infrared, dark field and Raman spectroscopies) are also presented. Lastly, we present the background motivation for this work explaining in detail the challenges faced by researchers in the fields of plasmonics and metamaterials. In particular, we focus on the need for alternative geometries and extending the range of frequencies at which plasmonic effects can be achieved. Chapter 2 starts with a historical review of plasmonics and its (potential) applications. This is followed by a detailed account of our work on localized plasmons in semiconductor nanocrystals and surface phonon modes in silicon carbide nanopillars. In Chapter 3 we relate our investigations on graphene starting with a brief introduction on the optical properties of this fascinating material. Our results on the modes supported by graphene sandwiches and their use for a new type of sensor are presented subsequently. Chapter 4 focuses on a short history of metamaterials and the exciting opportunities they offer. We then describe our investigations on metallic gyroids which exhibit strong chirality and negative refraction in the visible range. Chapter 5 is a report of our work on Fano resonances, beginning with a reminder on the original theory of Fano and followed by our derivation of an analytical formula and its use to explain the spectral response of nanophotonic systems. Finally, we conclude with some general conclusions on and prospects for nanophotonics drawing on our results in Chapter 6.

1.2. Theoretical Background

All the findings presented here originates at the intersection between the realm of electromagnetism and material science. Therefore it seems important to review on one hand Maxwell's equations which are the basis of the electromagnetic theory and on another hand the permittivity (or dielectric function) which together with the permeability fully describes the interaction of materials with light. Subsequently, we will summarize the main properties of polaritons, and in particular plasmons, which are responsible for most of the extraordinary results emerging from the field of nanophotonics.

1.2.1. Maxwell's Equations

The electromagnetic theory of light is one of the greatest successes of physics, describing the behaviour of electromagnetic radiations across all scales from radio waves up to X-rays and passing by visible light by solely four extremely concise equations known as Maxwell's equations. These relate spatial and temporal changes of the electric field $\mathbf{E}$ and magnetic induction $\mathbf{B}$ to each other, explaining the existence of self-sustained electromagnetic waves and describing their behaviour in the presence of charge ρ and current $\mathbf{J}$ densities. These equations can take slightly different forms depending on the treatment of the charges and currents; for example in the macroscopic formulation, the charges and currents are separated into bound and free contributions, resulting in two additional fields: the displacement vector $\mathbf{D}$ and the magnetization field $\mathbf{H}$. The differential forms of Maxwell's equations in both the microscopic and macroscopic formulation are presented in Tab.1.1 with the vacuum permeability $\mu_0 = 4\pi \times 10^{-7}\,\mathrm{H{\cdot}m^{-1}}$, vacuum permittivity $\varepsilon_0 = 1/\mu_0 \mathrm{c}^2 \sim 8.845 \times 10^{-12}\,\mathrm{F{\cdot}m^{-1}}$ (with c the speed of light in vacuum) and where $\partial_t = \partial/\partial t$. It can be seen that Gauss's laws imply the generation of electric fields due to free charges

Table 1.1: Maxwell's equations formulation

	Microscopic	Macroscopic
Gauss's law (electric)	$\boldsymbol{\nabla} \cdot \mathbf{E} = \rho/\varepsilon_0$	$\boldsymbol{\nabla} \cdot \mathbf{D} = \rho_f$
Gauss's law (magnetic)	$\boldsymbol{\nabla} \cdot \mathbf{B} = 0$	$\boldsymbol{\nabla} \cdot \mathbf{B} = 0$
Faraday's law	$\boldsymbol{\nabla} \times \mathbf{E} = -\partial_t \mathbf{B}$	$\boldsymbol{\nabla} \times \mathbf{E} = -\partial_t \mathbf{B}$
Ampère's law	$\boldsymbol{\nabla} \times \mathbf{B} = \mu_0 (\mathbf{J} + \varepsilon_0 \partial_t \mathbf{E})$	$\boldsymbol{\nabla} \times \mathbf{H} = \mathbf{J}_f + \partial_t \mathbf{D}$

as well as the absence of magnetic monopoles. At the same time Faraday's and Ampère's laws describe the electromotive force and induction by time varying magnetic and electric fields respectively. Both the microscopic and macroscopic formulations are equivalent in free space and are linked by the constitutive relations

$$\mathbf{D} = \varepsilon_0 \mathbf{E} + \mathbf{P} \quad = \varepsilon \mathbf{E} \tag{1.1}$$

$$\mathbf{H} = \frac{1}{\mu_0}\mathbf{B} - \mathbf{M} = \frac{1}{\mu}\mathbf{B} \tag{1.2}$$

where $\mathbf{P}$ and $\mathbf{M}$ are the polarization and magnetization of the medium defined by the bound charge and current densities as

$$\rho_b = -\boldsymbol{\nabla} \cdot \mathbf{P} \tag{1.3}$$

$$\mathbf{J}_b = \boldsymbol{\nabla} \times \mathbf{M} + \partial_t \mathbf{P} \tag{1.4}$$

ε and μ are the permittivity and permeability of the material[1]. The physical interpretation of the permittivity as well as its general behaviour and particularities will be explored further in Sec.1.2.2.3.

If we come back to Maxwell's equations and apply the vector identity

$$\boldsymbol{\nabla} \times (\boldsymbol{\nabla} \times \mathbf{E}) = \boldsymbol{\nabla}(\boldsymbol{\nabla} \cdot \mathbf{E}) - \boldsymbol{\nabla}^2 \mathbf{E} \tag{1.5}$$

to Faraday's law, we obtain

$$\begin{aligned}
\boldsymbol{\nabla} \times (\boldsymbol{\nabla} \times \mathbf{E}) &= -\partial_t(\boldsymbol{\nabla} \times \mathbf{B}) = -\partial_t \boldsymbol{\nabla} \times (\mu_0 \mathbf{H} + \mu_0 \mathbf{M}) = -\mu_0 \partial_t \boldsymbol{\nabla} \times \mathbf{H} \\
&= -\mu_0 \partial_t (\mathbf{J}_f - \partial_t \mathbf{D}) = -\mu_0 \partial_t \mathbf{J}_f - \mu_0 \partial_t^2 \mathbf{D} \\
&= -\mu_0 \partial_t \mathbf{J}_f - \mu_0 \partial_t^2 (\varepsilon_0 \mathbf{E} + \mathbf{P}) \\
\boldsymbol{\nabla}(\boldsymbol{\nabla} \cdot \mathbf{E}) - \boldsymbol{\nabla}^2 \mathbf{E} &= -\mu_0 \varepsilon_0 \partial_t^2 \mathbf{E} - \mu_0 \partial_t \mathbf{J}_f - \mu_0 \partial_t^2 \mathbf{P} \\
\boldsymbol{\nabla}^2 \mathbf{E} - \mu_0 \varepsilon_0 \partial_t^2 \mathbf{E} &= \mu_0 \partial_t \mathbf{J}_f + \mu_0 \partial_t^2 \mathbf{P}
\end{aligned} \tag{1.6}$$

where we have considered a non-magnetic material ($\mathbf{M}$=0) in the absence of external charges ($\boldsymbol{\nabla} \cdot \mathbf{E} = 0$). The last equation shows that an external current or the polarization of a material will create electromagnetic waves; they are source terms which will interfere with the original incoming wave. In addition, non-linear polarizations will create additional waves at frequencies $N \times \omega_0$. If we take the case of vacuum these source terms disappear and we arrive at a typical d'Alembert wave equation:

$$\boldsymbol{\nabla}^2 \mathbf{E} - \frac{1}{\mathrm{c}^2} \partial_t^2 \mathbf{E} = 0 \tag{1.7}$$

where we have used the fact that $\mathrm{c}^2 = 1/\varepsilon_0 \mu_0$. One very important results of the laws of electromagnetism is that in vacuum any radiation travels at the speed of light c, irrespective of its frequency.

The simplest solutions to this equation is provided by a harmonic dependence of the type

$$\begin{cases} \mathbf{E}(\mathbf{r}, t) &= \mathbf{E}_0 \cos(\omega t - \mathbf{k} \cdot \mathbf{r}) = \Re\left\{\mathbf{E}_0 \mathrm{e}^{\mathrm{i}(wt - \mathbf{k} \cdot \mathbf{r})}\right\} \\ \mathbf{H}(\mathbf{r}, t) &= \mathbf{H}_0 \cos(\omega t - \mathbf{k} \cdot \mathbf{r}) = \Re\left\{\mathbf{H}_0 \mathrm{e}^{\mathrm{i}(wt - \mathbf{k} \cdot \mathbf{r})}\right\} \end{cases} \tag{1.8}$$

which corresponds to plane waves. Indeed at any moment in time, $\mathbf{k} \cdot \mathbf{r}$ is a constant, defining a plane perpendicular to the propagation direction $\mathbf{k}$. These solutions are called transverse electromagnetic waves (TEM) because the electric and magnetic fields are perpendicular to the wavevector $\mathbf{k}$ and to each other.

[1]Note that SI units are used throughout the thesis and that we assume here uniform, local and isotropic materials.

More generally, monochromatic waves can be described by the Helmoltz equation for propagation in media with a slowly varying permittivity

$$\boldsymbol{\nabla}^2\mathbf{E}(\mathbf{r}) + k^2(\mathbf{r})\mathbf{E}(\mathbf{r}) = 0 \tag{1.9}$$

where the angular frequency ω, frequency ν, wavevector $k = |\mathbf{k}|^2$ and wavelength λ are linked by the following relations

$$\omega = 2\pi\nu \qquad \lambda = 2\pi/k \tag{1.10}$$

$$\omega = k_0\mathrm{c} \qquad \lambda_0 = \mathrm{c}/\nu \tag{1.11}$$

Last, it is important to define the energy which is carried by an electromagnetic wave. From the energy conservation law known as Poynting's theorem, changes in the electromagnetic energy density are caused by energy flow and dissipation, reading

$$\partial_t u + \boldsymbol{\nabla}\cdot\mathbf{S} = -\mathbf{J}\cdot\mathbf{E} \tag{1.12}$$

where u, the energy density, is given by

$$u = \frac{1}{2}\left(\mathbf{E}\cdot\mathbf{D} + \mathbf{B}\cdot\mathbf{H}\right) \tag{1.13}$$

for a linear medium with no dispersion nor loss. The Poynting vector $\mathbf{S} = \mathbf{E}\times\mathbf{H}$ is the central quantity here defined as the energy flux vector. It describes the direction of energy propagation, being therefore collinear with the wavevector of the electromagnetic wave, while its magnitude is related to the intensity transported $I = \langle\mathbf{S}\rangle$.

From the above equations, one can conclude that plane waves would carry an infinite amount of energy, underlining the fact that these are a mathematical construction with no true physical meaning [1–5].

1.2.2. Optical Properties of Matter

1.2.2.1. Molecules Response to Light (Polarizability)

When a molecule is bathed in an electromagnetic (EM) wave two phenomena can occur which depend on the wavelength. First, if the incoming radiation energy is far from any resonances of the molecule, non-resonant or elastic scattering will take place. That is, the electric field will simply drive the electron "cloud" out of equilibrium, inducing a dipole that will then be a source of radiation at the same frequency than the incident wave until it turns back to rest. But at any time the molecule stays in its ground-state.

In the second case, where the energy is close to a molecular resonance, resonant or dissipative absorption is going to happen. In this case, the EM field will cause a molecular transition which type and energy will depend on the frequency. The transitions are between vibrational or rotational states in the infrared while they rely on electronic transitions in the visible. All these processes consist of energy absorption, the molecule is therefore in an excited state which will relax to its ground state after a certain time. In most cases, molecules or atoms are surrounded by a lot of other molecules or atoms even in the case of low pressure gases. As a result, an excited molecule will generally reduce its energy primarily by collision transforming the incoming photon into thermal energy.

An important parameter accounts for all the interaction of a molecule with light which is its polarizability $\boldsymbol{\alpha}$. It describes the ability of a molecule to acquire a dipole moment $\boldsymbol{\mu}$ under the influence of an electric field $\mathbf{E} = \hat{z}\mathcal{E}$. It can be written as the sum of permanent and induced dipoles

$$\langle \mu_z \rangle = \mu_{0z} + \alpha_{zz}\,\mathcal{E} + \frac{1}{2}\beta_{zzz}\,\mathcal{E}^2 + \dots \tag{1.14}$$

where μ_{0z} denotes the permanent dipoles, α_{zz} the polarizability and β_{zzz} the first hyperpolarizability, all along the z-direction. The polarizability can be expressed as the sum of all the transitions that may occur which gives for the z-direction

$$\alpha_{zz} = \frac{2}{\hbar}\sum_n \frac{\omega_{n0}\mu_{z,0n}\,\mu_{z,n0}}{\omega_{n0}^2 - \omega^2} \tag{1.15}$$

where $\mu_{z,if}$ is the matrix element $\langle i|\mu_z|f\rangle$ of the transition dipole moment for the z-direction. If we consider a random arrangement of molecules, we can easily derive a mean polarizability $\alpha = \frac{1}{3}(\alpha_{xx} + \alpha_{yy} + \alpha_{zz})$ and therefore

$$\alpha(\omega) = \frac{2}{3\hbar}\sum_n \frac{\omega_{n0}|\mu_{n0}|^2}{\omega_{n0}^2 - \omega^2} \tag{1.16}$$

In conclusion, we see that the polarizability will depend on the probability and energy of each transition and the dipole moment amplitude obtained. The total dipole moment of the molecule is therefore the sum of the permanent dipoles if there are any and the dipoles caused by the field which are given, as

we have just seen, by the polarizability[2]. Finally it is important to note that $\boldsymbol{\alpha}$ is a second rank tensor which means it is direction dependent. In consequence, the respective orientation between the field and the molecule does have a strong and direct effect on the response of the latter [2, 6].

1.2.2.2. Dense Medium (Susceptibility)

In dense media, scattering also occurs as described above but this time atoms are closely packed in an organized way. As a result, the scattered waves will average to zero laterally. Instead, the scattering by atoms only produces constructive interferences in the forward and backward direction which are the familiar refracted and reflected waves. The phase shift that arises due to the absorption and re-emission of photons by atoms results in a change of the wave phase velocity; this effect is summarized by assigning a macroscopic refractive index to the medium as we will see in the next section.

The optical response of non-magnetic materials is fully described by their dielectric function, or permittivity[3]. As we have seen in Sec.1.2.1, the electric field induces a charge separation in the medium generally called the electric displacement field

$$\mathbf{D} = \varepsilon \mathbf{E} \tag{1.17}$$

ε can be rewritten in terms of relative (ε_r) and vacuum (ε_0) permittivity that allows to separate between the field itself and the polarization of the medium

$$\mathbf{D} = \varepsilon_0 \varepsilon_r \mathbf{E} = \varepsilon_0 (1 + \chi)\mathbf{E} = \varepsilon_0 \mathbf{E} + \mathbf{P} \tag{1.18}$$

where $\chi = \mathbf{P}/\varepsilon_0 \mathbf{E}$ is the electric susceptibility which represents the ratio between bound and free charge densities. [Note that, later on, we will always talk about dielectric function, permittivity or ε, but actually we will always only refer to the relative permittivity ε_r.] To link the macroscopic polarization to the molecules polarizability it is necessary to access the local electric field $\mathbf{E}^*$ experienced by them. This is usually done using the Lorentz local field approximation which states that

$$\mathbf{E} = \mathbf{E}^* \left(1 - \frac{\alpha N}{3\varepsilon_0}\right) \tag{1.19}$$

then it is easy to express the polarization in terms of molecules polarizability since

$$\mathbf{P} = \alpha N \mathbf{E}^* = \left(\frac{3\alpha N}{3\varepsilon_0 - \alpha N}\right) \varepsilon_0 \mathbf{E} \tag{1.20}$$

and therefore

$$\chi = \frac{\alpha N/\varepsilon_0}{1 - \alpha N/3\varepsilon_0} \qquad \text{and} \qquad \varepsilon_r = \frac{1 + 2\alpha N/3\varepsilon_0}{1 - \alpha N/3\varepsilon_0} \tag{1.21}$$

[2]There are also non-linear effects which depend on the field intensity $\mathcal{E}^2$ and higher order $\mathcal{E}^3$, $\mathcal{E}^4$... These ones are described by the hyperpolarizabilities.

[3]Since we only consider non-magnetic materials here $\mu_r(\omega) = 1$.

Generally, the permittivity and susceptibility are second-rank tensors; in the case of isotropic media which we consider here they reduce to simple scalar. Going back to Eq.1.16 we can rewrite the permittivity as a sum of oscillators which strength directly corresponds to the transition probabilities and which natural frequencies depend on the transition type

$$\varepsilon_r = 1 + \frac{2N}{3\hbar\varepsilon_0} \sum_n \frac{\omega_{n0} |\mu_{n0}|^2}{\omega_{n0}^2 - \omega^2} \tag{1.22}$$

where we have used the relations $1/(1-x) \approx 1+x$ and dropped the quadratic term considering α very small. Other terms can be added to this permittivity in the same way, namely as oscillators, to account for other polarization mechanisms. This formulation allows a more straight-forward interpretation. Indeed, all materials are composed out of atoms, some of them are ionic crystals, possess permanent dipoles or are composed of interfaces which may act as condensers. Each of these charged species can affect and be affected by the electric field of EM waves; however since their inertia (an electron cloud can deform much faster than a molecule rotate) vary considerably each of them will be active in a specific frequency range and have a natural resonance at a particular frequency, see Fig.1.1. As can be seen the response of the material to light depends on the wavelength; this phenomenon is called dispersion.

If we look closer at Eq.1.22 we see that the permittivity goes to infinity at resonance; this is clearly non-physical. In fact, until now we have neglected damping which comes from the many interactions that the excited atoms or dipoles have with their surrounding. These cause the transformation of the incoming wave into heat, that is dissipation. A damping term $\mathrm{i}\,\gamma_n\,\omega$ can therefore be added at the denominator of Eq.1.22 which induces the permittivity to become a complex function. Now, when at resonance, the coupling between the field and the oscillators is still maximum but almost all the energy is converted into heat. Fig.1.1 shows a typical dispersion curve of a dielectric medium plotting both the real and imaginary part of the permittivity. As one can see the absorption is maximum when the driving field matches with the resonant frequency of a polarization mechanism. At the same time, we see that all charged species contribute to the material polarizability (*i.e.* to its dielectric constant) at very low frequency, and as the driving field frequency increases, only those mechanisms with a small inertia will continue to react until we reach the UV regime at which even the electrons become too slow to contribute [7]. The next section will discuss the complex permittivity in more details as well as two widely used models to describe it [1–3, 5, 6].

1.2.2.3. Permittivity and Refractive Index

We discussed earlier the concept of dispersion, i.e. the property of all materials to have an optical response dependent on the wavelength of the light. This arises due to causality requirements which state that a material, or similarly any optical system, cannot affect a single frequency without causing phase shifts to neighbouring frequencies if one wants to maintain destructive interferences for times preceding the arrival of the wave. In addition, the permittivity is a complex function, with a real part defining the phase shift and an imaginary part related to dissipation. An alternative point of view is to realize that the response

of a medium cannot be instantaneous, hence the dispersive and complex character of the permittivity. These effects are also often referred to as Kramers-Kronig relations; the imaginary and real part are then intimately linked by causality and so one can be deduced from the other by an integration in Fourier space. Those relations read for the susceptibility $\chi = \chi_1 + \mathrm{i}\chi_2$

$$\chi_1(\omega) = \frac{2}{\pi}\mathcal{P}\int_0^\infty \frac{\omega'\chi_2(\omega')}{\omega'^2 - \omega^2}\,\mathrm{d}\omega' \tag{1.23}$$

where $\mathcal{P}$ indicates the Cauchy principal part of this undefined integral.

To understand the effect of the permittivity of a medium on the propagation of an EM wave, let us go back to Eq.1.6, dropping the external current density source term $\mu_0\partial_t\mathbf{J}_f$, and using the definition of the susceptibility $\chi = \mathbf{P}/\varepsilon_0\mathbf{E}$:

$$\begin{aligned}
\boldsymbol{\nabla}^2\mathbf{E} - \mu_0\varepsilon_0\partial_t^2\mathbf{E} = \mu_0\partial_t^2\mathbf{P} = \mu_0\varepsilon_0\chi\partial_t^2\mathbf{E} \\
\boldsymbol{\nabla}^2\mathbf{E} - \mu_0\varepsilon_0(1+\chi)\partial_t^2\mathbf{E} = 0 \\
\boldsymbol{\nabla}^2\mathbf{E} - \frac{\tilde{n}^2}{\mathrm{c}^2}\partial_t^2\mathbf{E} = 0
\end{aligned} \tag{1.24}$$

where we have used the definition $\varepsilon = 1 + \chi = \tilde{n}^2$, $\tilde{n}$ being the refractive index. [Note that we are now using ε instead of ε_r to depict the dielectric function.] The permittivity and the refractive index are both complex and frequency dependent quantities which relate to each other as shown in Tab.1.2. Eq.1.24 is

Table 1.2: Relations between the complex permittivity and index of refraction

Permittivity	Refractive Index
$\varepsilon = \varepsilon_1 + \mathrm{i}\varepsilon_2$	$\tilde{n} = n + \mathrm{i}k$
$\varepsilon = 1 + \chi = \tilde{n}^2$	$\tilde{n} = \sqrt{\varepsilon}$
$\varepsilon_1 = n^2 - k^2$	$2n^2 = \sqrt{\varepsilon_1^2 + \varepsilon_2^2} + \varepsilon_1$
$\varepsilon_2 = 2nk$	$2k^2 = \sqrt{\varepsilon_1^2 + \varepsilon_2^2} - \varepsilon_1$

again a d'Alembert wave equation, but comparing with light propagation in vacuum (Eq.1.7), its phase velocity is now reduced to $v = \mathrm{c}/n$. Similarly the actual wavelength $\lambda = \lambda_0/n$ and wavevector $k = nk_0$ are modified compared to their value in free space λ_0 and k_0. When the medium is absorbing, i.e. the index of refraction is complex, the intensity of the wave I_0 will in addition be reduced as it propagates along x following a Beer-Lambert's relation

$$I(x) = I_0\mathrm{e}^{-\alpha x} \qquad \text{with} \qquad \alpha = \frac{2k\omega}{\mathrm{c}} = \frac{4\pi k}{\lambda} \tag{1.25}$$

where k, the imaginary part of the refractive index, is called the extinction coefficient, and α is the absorption coefficient. The latter is directly related to the absorption spectrum of the medium, mirroring

its band structure. Kramers-Kronig relations can be expressed for the refractive index as

$$n(\omega) = n_\infty + \frac{\mathrm{c}}{\pi}\mathcal{P}\int_0^\infty \frac{\alpha(\omega')}{\omega'^2 - \omega^2}\,\mathrm{d}\omega' \tag{1.26}$$

Furthermore, the refractive index provides also a direct knowledge of the reflectivity of a surface at normal incidence. In the case of an interface with air, the reflectivity is given by

$$R = \left|\frac{\tilde{n}-1}{\tilde{n}+1}\right|^2 \tag{1.27}$$

which leads to an absence of reflection for $\tilde{n} = 1$ as expected. As we can see, the refractive index describes the properties of the EM wave inside the medium. At the opposite, the permittivity is linked to the response in the complex plane of the electrons to the driving field. The real part is linked to how much energy is stored while the imaginary part represents the amount of energy dissipated [2–5, 8].

1.2.2.4. The Drude-Lorentz model

In order to describe the physics behind the behaviour of the dielectric function, the Drude-Lorentz model is widely used. It is based on a classical approach, relating the polarization of a material to the displacement of its electrons induced by an electric field. By summing all the forces acting on the electrons

$$\mathrm{m_e}\ddot{\mathbf{x}} = \sum_i \mathbf{F}_i = \mathbf{F}_{electric} - \mathbf{F}_{friction} - \mathbf{F}_{spring} \tag{1.28}$$

we can then derive a simple equation of motion

$$\mathrm{m_e}\ddot{\mathbf{x}} + \mathrm{m_e}\gamma\dot{\mathbf{x}} + k\mathbf{x} = -\mathrm{q_e}\mathbf{E} \tag{1.29}$$

where γ quantifies the resistance to the movement of the electrons and kx is the restoring force of a harmonic oscillator which natural frequency is $\omega_0 = \sqrt{k/\mathrm{m_e}}$. $\mathrm{m_e}$ and $\mathrm{q_e}$ are the mass and charge of the electron respectively. If we consider the action of an EM wave, a harmonic time dependence of the type $\mathbf{E}(t) = \mathbf{E}_0\mathrm{e}^{-\mathrm{i}\omega t}$ can then be assumed for the electric field. As a result, the displacement will follow a similar periodicity and $\mathbf{x}(t) = \mathbf{x}_0\mathrm{e}^{-\mathrm{i}\omega t}$. Taking the time derivatives of $\mathbf{x}$ in the above equation and rearranging the terms we get for the displacement

$$\mathbf{x} = -\frac{\mathrm{q_e}}{\mathrm{m_e}(\omega_0^2 - \omega^2 - \mathrm{i}\gamma\omega)}\mathbf{E} \tag{1.30}$$

which leads to a total electronic polarization

$$\mathbf{P}_e = -N\mathrm{q_e}\mathbf{x} \tag{1.31}$$

with N the density of electrons. We can now use the definition of the displacement field, Eq.1.1, to deduce the permittivity associated with such a system

$$\mathbf{D} = \varepsilon\varepsilon_0\mathbf{E} = \varepsilon_0\mathbf{E} + \mathbf{P}_{ion} + \mathbf{P}_{electron} \tag{1.32}$$

where $\mathbf{P}_{ion} = (\varepsilon_\infty - 1)\varepsilon_0\mathbf{E}$ is the polarization created by the static ion cores background. This finally results in the Drude-Lorentz permittivity

$$\varepsilon = \varepsilon_\infty + \frac{N{\mathrm{q_e}}^2}{\varepsilon_0 \mathrm{m_e}} \frac{1}{(\omega_0^2 - \omega^2 - \mathrm{i}\gamma\omega)} \tag{1.33}$$

which has the typical form of a damped harmonic oscillator, also called Lorentz oscillator, which we described earlier in Eq.1.16 and 1.22 [2, 3, 8, 9].

There are two particular cases that will be of interest to us, on the one hand the response of conduction electrons in metals and semiconductors and on the other hand the effect of optical phonons on the permittivity of polar crystals.

Conduction Electrons in Metals and Semiconductors

The dielectric function of metals and semiconductors can be well approximated by considering free, non-interacting electrons. This implies the absence of a resonant frequency ω_0 in Eq.1.33 leading to the well-known Drude model

$$\varepsilon = \varepsilon_\infty - \frac{\omega_p^2}{(\omega^2 + \mathrm{i}\Gamma\omega)} \tag{1.34}$$

where we defined the plasma frequency $\omega_p^2 = N{\mathrm{q_e}}^2/\varepsilon_0{\mathrm{m_e}}^*$ with ${\mathrm{m_e}}^*$ the effective mass of the electron. ε_∞ is the high frequency dielectric constant and $\Gamma = 2\pi/\tau$ the collision frequency (τ being the mean collision time). Fig.1.2 shows the permittivity, index and reflectivity of gold as measured by ellipsometry alongside a Drude model with $\varepsilon_\infty = 5$, $\omega_p = 1.33 \times 10^{16}$ rad/s and $\Gamma = 8.38 \times 10^{13}$ rad/s. As it can be seen, at energies smaller than the plasma frequency a metal is highly reflecting characterized by a negative permittivity and an index smaller than unity. Above ω_p, the field oscillates too fast for the conduction electrons and the system behaves like a dielectric. Compared to the experimental data, it is clear that the Drude model is an accurate description of a metal, except in the range of interband transitions (above 2.5 eV for the case of gold). There the strong damping of the conduction electrons impairs their screening of the incident electric field hence reducing the metal reflectivity. In semiconductors, the carrier density N and therefore ω_p can easily be tuned by chemical doping, temperature or electrical injection giving a great degree of control over their optical properties. This can prove very useful for nanophotonic applications as we will see later on.

Last, conductors are often described by their conductivity rather than their permittivity. In a similar way that we derived the dielectric function, the conductivity σ can be obtained through the definition of the carrier density

$$\mathbf{j} = \sigma\mathbf{E} = -N\mathrm{q_e}\mathbf{v} \tag{1.35}$$

with the velocity $\mathbf{v} = \dot{\mathbf{x}}$ leading to

$$\sigma = \frac{\sigma_0}{1 - \mathrm{i}\omega\tau} \qquad \text{where} \qquad \sigma_0 = \frac{N{\mathrm{q_e}}^2\tau}{{\mathrm{m_e}}^\star} \tag{1.36}$$

is the DC conductivity. This allows us to relate the permittivity to the conductivity via

$$\varepsilon = \varepsilon_\infty + \frac{\mathrm{i}\sigma}{\varepsilon_0\omega} \tag{1.37}$$

Collective oscillations of the conduction electrons, which can be visualized as charge density fluctuations, and known as plasmons, exhibit fascinating properties which we will discuss in details in Sec.1.2.3.

Optical Phonons in Polar Crystals

Any crystal with more than one atom per unit cell will have two types of vibration modes, see Fig.1.3. At low energies, the whole crystal moves in phase as a sound wave hence the name of acoustic phonons (LA and TA). At higher energies (LO and TO), neighbouring atoms belong to different sub-lattices and their displacements are out of phase. These modes can be excited optically in ionic crystals hence their designation as optical phonons. Fig.1.4 shows the dispersion of these vibrational modes in polar (GaAs) and non-polar (Si, Ge) crystals. Phonons can be either longitudinal (LA and LO) waves, where the displacement of the atoms is parallel to the wavevector, or transverse (TA and TO) if their movement is perpendicular to the wave propagation direction, as sketched in Fig.1.3. Optical phonons in crystals with polar bonds, *i.e.* ionic and partially covalent crystals alike such as GaAs, will carry a charge and can interact with the electric field of light. The interaction of the TO modes with the transverse electric field of EM waves lifts their degeneracy from the LO phonons which cannot interact with a transverse field, see Fig.1.3. This splitting results in the permittivity of the material exhibiting the strongly reflective Reststrahlen band which we will describe in the following.

Coming back once again to the Drude-Lorentz model (Eq.1.33) and replacing the mass and charge of the electrons by the effective values for the polar bond of the phonons $-\mathrm{q_e} \to Q$ and $\mathrm{m_e} \to \mu$, we obtain

$$\varepsilon = \varepsilon_\infty + \frac{NQ^2}{\varepsilon_0\mu}\frac{1}{\omega_{TO}^2 - \omega^2 - \mathrm{i}\gamma\omega} \tag{1.38}$$

where following the above discussion we used $\omega_0 = \omega_{TO}$. We can also define a static permittivity

$$\varepsilon(0) = \varepsilon_{st} = \varepsilon_\infty + \frac{NQ^2}{\varepsilon_0\mu\omega_{TO}^2} \tag{1.39}$$

which simplifies the dielectric function to

$$\varepsilon = \varepsilon_\infty + (\varepsilon_{st} - \varepsilon_\infty)\frac{\omega_{TO}^2}{\omega_{TO}^2 - \omega^2 - \mathrm{i}\gamma\omega} \tag{1.40}$$

This could be enough but it is interesting to observe what is happening when the permittivity is null since it allows to rewrite the previous equation in a more meaningful fashion. Indeed Gauss's law states that $\boldsymbol{\nabla} \cdot \mathbf{D} = 0 = \varepsilon\varepsilon_0 \boldsymbol{\nabla} \cdot \mathbf{E}$ which implies that $\mathbf{k} \cdot \mathbf{E} = 0$. Therefore in general the electric field must be perpendicular to the propagation direction and only transverse waves can exist. However, if the permittivity equals zero, this condition does not need to be fulfilled any more and the material can support longitudinal waves. This allows us to naturally associate the zero in the permittivity to the frequency of the LO phonons, *i.e.* $\varepsilon(\omega_{LO}) = 0$. Considering that $\gamma << \omega_{TO}$ we obtain the Lyddane-Sachs-Teller relationship

$$\frac{\omega_{LO}^2}{\omega_{TO}^2} = \frac{\varepsilon_{st}}{\varepsilon_\infty} \tag{1.41}$$

which gives the final form for the permittivity of optical phonons

$$\varepsilon = \varepsilon_\infty \left(1 + \frac{\omega_{LO}^2 - \omega_{TO}^2}{\omega_{TO}^2 - \omega^2 - \mathrm{i}\gamma\omega}\right) \tag{1.42}$$

Fig.1.5 plots the permittivity, index and reflectivity of silicon carbide (SiC) with $\varepsilon_\infty = 6.56$, $\omega_{LO} = 969.9\,\mathrm{cm}^{-1}$, $\omega_{TO} = 797\,\mathrm{cm}^{-1}$ and $\gamma = 4.76\,\mathrm{cm}^{-1}$ [11]. Between the LO and TO frequencies, which generally lies in the mid infrared, the material exhibits a very high reflectivity known as the Reststrahlen band.

Due to the absence of electric transport, optical phonons do not suffer from Ohmic losses and present very sharp and strong resonances which show great promises for nanophotonic applications as we will see in Sec.2.3 [3, 8, 9].

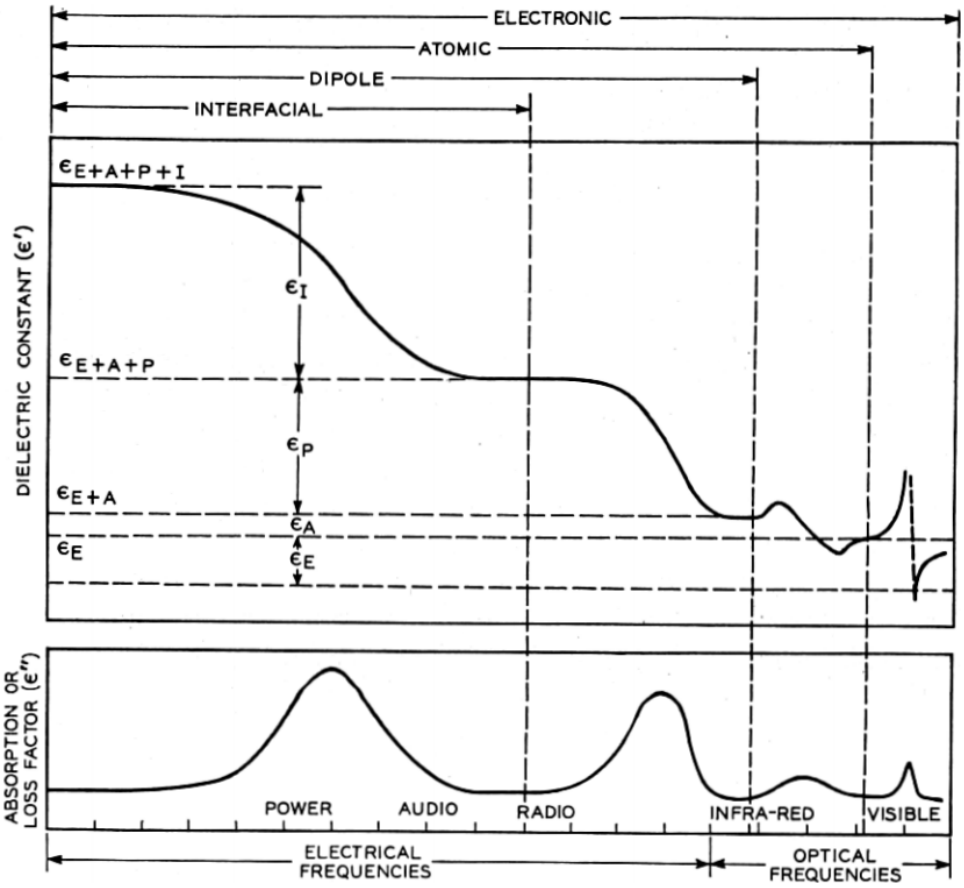

Figure 1.1: A typical dispersion behaviour, here the permittivity $\varepsilon_r = \chi + 1$ for a material exhibiting all main polarization mechanisms. The top panel shows the real part of the permittivity or dielectric constant and the lower panel its corresponding imaginary part which is related to the absorption within the medium. At very high frequencies, only the electronic excitations are fast enough to react to and screen the driving field resulting in the optical response of the materials. As the frequency is reduced, additional polarization mechanisms contribute to the dielectric constant when their inertia (or natural resonant frequency) becomes comparable or larger than the driving field frequency. Within the infra-red, polar bonds (here referred to as the atomic contribution) in ionic and partially covalent crystals can interact with light in the form of optical phonons. Within the far-infrared and microwave regime, one can observe the flipping of the permanent dipoles of molecules or crystallites and in the low gigahertz regime, the field is slow enough to allow for the reorganization of charges at grain boundaries in ceramics, also known as interfacial configuration (Reprinted from [7]).

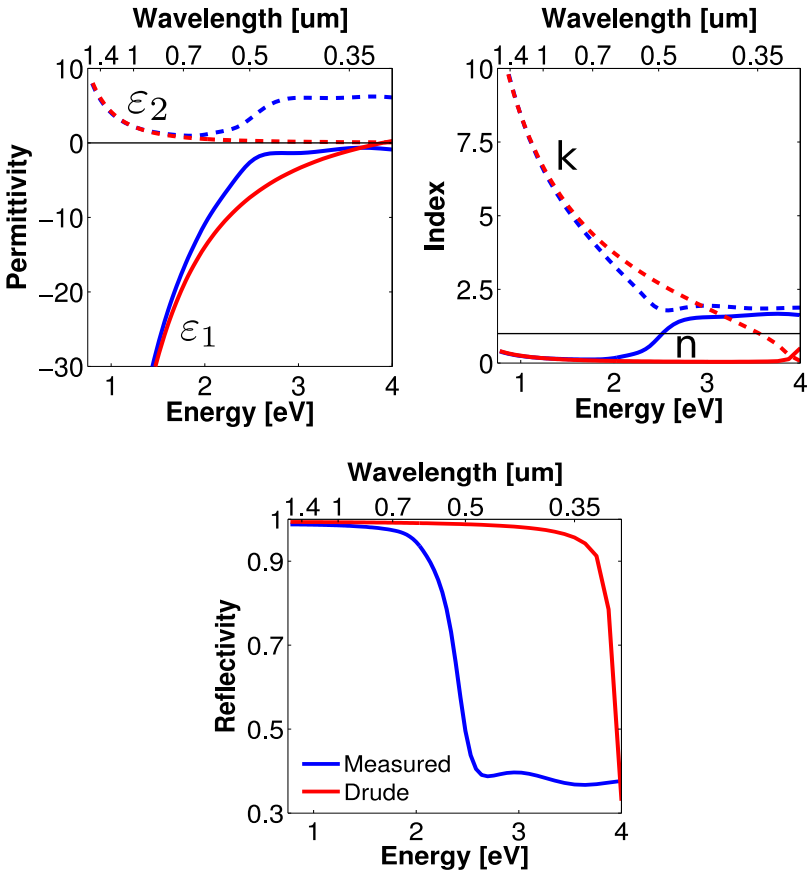

Figure 1.2: Optical properties of gold as measured by ellipsometry (blue lines) or described by a Drude model ($\omega_p = 1.33 \times 10^{16}$ rad/s, $\Gamma = 8.38 \times 10^{13}$ rad/s and $\varepsilon_\infty = 5$, red lines). Left: real (full lines) and imaginary part (dashed lines) of the permittivity; right: real (full lines) and imaginary part (dashed lines) of the refractive index; bottom: the reflectivity of a semi-infinite gold under normal incidence as calculated from Eq.1.27.

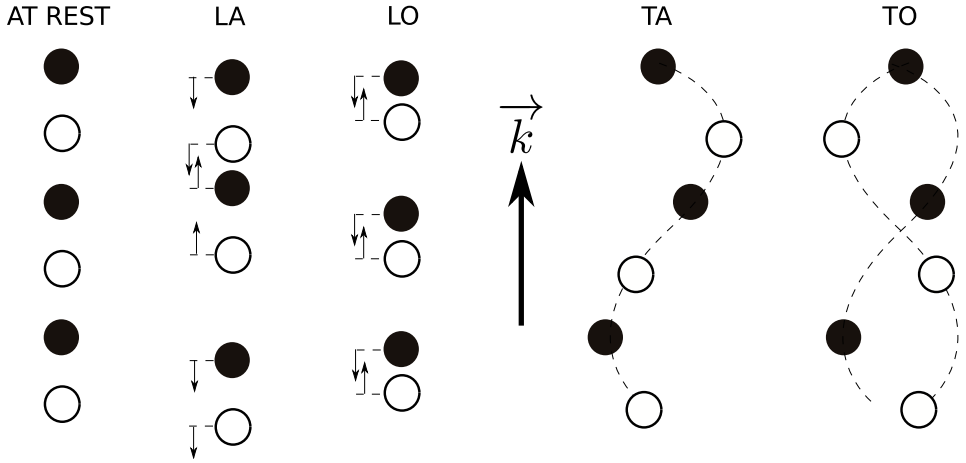

Figure 1.3: Example of phonon modes for a linear chain composed of two different atoms. Longitudinal acoustic (LA) and optical (LO) modes have a displacement of the atoms parallel to the wave propagation direction $\overrightarrow{k}$ while for transverse acoustic (TA) and optical (TO) modes the movement is perpendicular to the wavevector. In acoustic phonons (LA and TA), neighbouring atoms oscillate in phase while they are out of phase in the case of optical phonons (LO and TO).

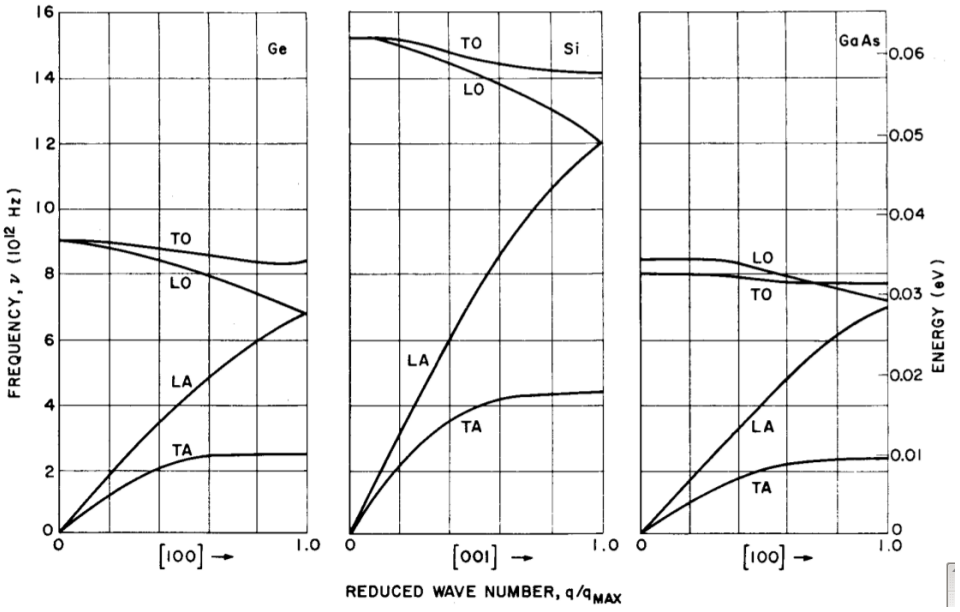

Figure 1.4: Dispersion relations of optical (TO and LO) and acoustic (TA and LA) phonons in Ge, Si and GaAs along the main crystal axis. The optical phonons are located within the mid-infrared range and are degenerated for non-polar materials (Ge, Si) at the Γ-point. In the case of polar crystals (such as GaAs) the lifting of the degeneracy between the TO and LO phonons at $(0, 0, 0)$ gives rise to a Reststrahlen band (Reprinted from [10]).

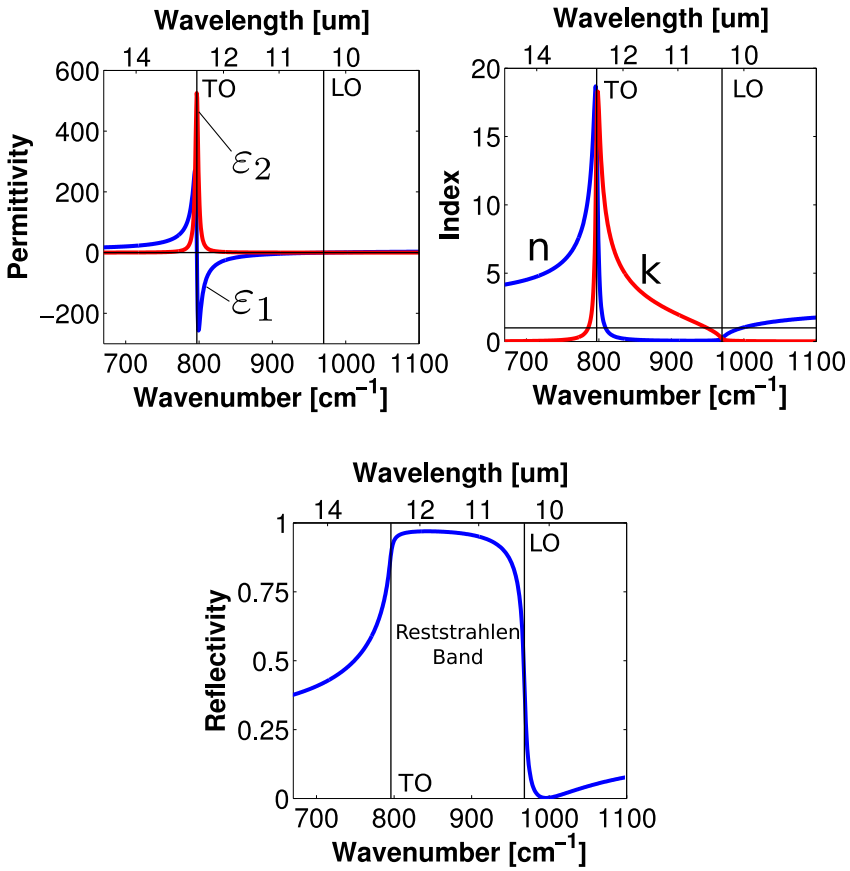

Figure 1.5: Optical properties of SiC as described by a Drude-Lorentz model ($\varepsilon_\infty = 6.56$, $\omega_{LO} = 969.9\,\mathrm{cm}^{-1}$, $\omega_{TO} = 797\,\mathrm{cm}^{-1}$ and $\gamma = 4.76\,\mathrm{cm}^{-1}$). Left: real (blue line) and imaginary part (red line) of the permittivity; right: real (blue) and imaginary part (red) of the refractive index; bottom: the reflectivity of a semi-infinite SiC under normal incidence as calculated from Eq.1.27. One can observe the strong absorption peak at the TO position, the flip of sign of the real permittivity at the LO frequency and the strongly reflecting Reststrahlen band in between these two modes.

1.2.3. (Localized) Surface Polaritons

1.2.3.1. Polaritons

Polaritons are those mixed quasiparticles which form when photons hybridize with charged excitations in solids such as plasmons, optical phonons, excitons, etc. In the polariton picture, the dispersions of the photon and quasiparticle experience an anti-crossing due to strong coupling resulting in two distinct modes called upper and lower polariton branches, as shown in Fig.1.6. This is similar to a system of

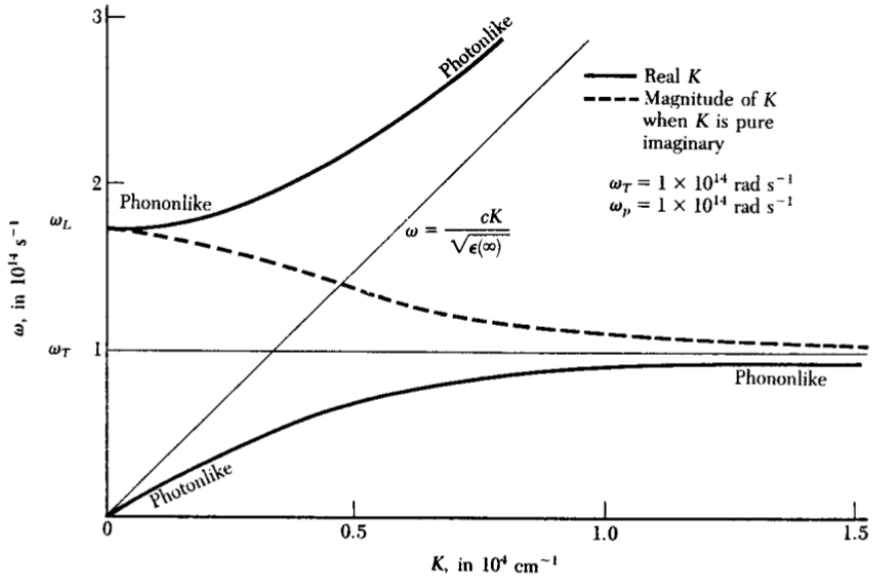

Figure 1.6: Typical dispersion relation of polaritons: the hybridization between the photons with dispersion $\omega \propto kc$ and the transverse optical phonons at ω_T results in a splitting into upper (radiative states) and lower (confined states) polaritonic branches. The dashed line corresponds to the magnitude of the attenuation when the wavevector k is purely imaginary (Reprinted from [9]).

two coupled oscillators where two new eigenfrequencies arise due to the interaction. The upper branch is located at wavevectors smaller than that of light and therefore describes radiative or unbound modes - the medium is transparent at these energies. At the opposite, the lower branch is composed by surface polariton modes. These possess a wavevector bigger than light in free space and in consequence are bound as we will see below.

Before investigating further these modes, let us remind that, as we saw in the previous section, these excitations are strongly resonant and therefore highly absorbing. In consequence, an EM wave impinging on such a material will be damped within a characteristic skin depth

$$\delta = \frac{1}{\alpha} = \frac{\lambda}{4\pi k} = \frac{\mathrm{c}}{2k\omega} \sim \frac{1}{\sqrt{2\sigma_0 \omega \mu_0}} \tag{1.43}$$

where the last expression is valid for the Drude model at low frequencies where the real and imaginary parts of the refractive index have similar magnitude. It implies that all the physics is being confined to the interface which is the subject of the next section.

1.2.3.2. Surface Polaritons (SPP)

Let us consider a wave which is travelling in the XZ plane close to an interface at $z = 0$ between a metal ($z < 0$) and a dielectric ($z > 0$), see Fig.1.7 for a schematic. First of all, it is practical to decompose the

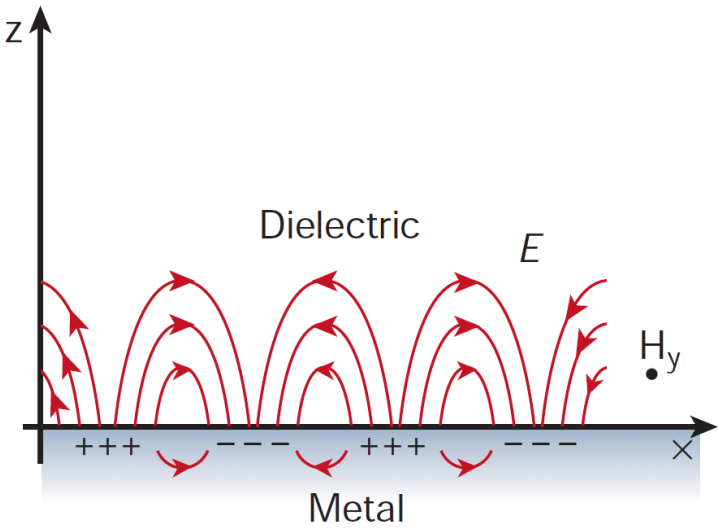

Figure 1.7: SPP field profile at the interface between a dielectric and a metal. This TM-polarized mode travelling along the x direction and confined at the interface at $z = 0$ arises from the charge fluctuations (noted by '+' and '−' signs) within the skin depth of the metal known as surface plasmons (Reprinted from [12]).

light into a superposition of two polarizations where the orientation of the electric field is parallel (s or transverse electric TE) or perpendicular (p or transverse magnetic TM) to the interface. Then we see that the non-zero components of the electric and magnetic fields are

$$s, TE \begin{cases} H_x \\ E_y \\ H_z \end{cases} \qquad \text{and} \qquad p, TM \begin{cases} E_x \\ H_y \\ E_z \end{cases} \tag{1.44}$$

where s (p) polarization only has a transverse electric (magnetic) field hence its name. The wave considered here has the form $\mathbf{E}(x, y, z) = \mathbf{E}(z)\mathrm{e}^{\mathrm{i}\beta x}$ where $\beta = k_x$ is called the propagation constant and is a complex wavevector. Furthermore, the harmonic time dependence of the electric field leads $\partial/\partial t = -\mathrm{i}\omega$ so that we can rewrite our d'Alembert wave equation (Eq.1.7) as the Helmholtz equation

$$\nabla^2\mathbf{E} + k_0^2\varepsilon\mathbf{E} = 0 \qquad \text{or} \qquad \nabla^2\mathbf{H} + k_0^2\varepsilon\mathbf{H} = 0 \tag{1.45}$$

For TM and TE polarized light, respectively, the generic wave equation will therefore read as

$$\partial_z^2 H_y + (k_0^2\varepsilon - \beta^2)H_y = 0 \qquad \text{and} \qquad \partial_z^2 E_y + (k_0^2\varepsilon - \beta^2)E_y = 0 \tag{1.46}$$

We are interested in studying here the surface waves, that is, those with an evanescent decay away from the interface. If we take the case of TM waves, the transverse magnetic field of such confined waves is

$$H_y(x,z) = A_2 \mathrm{e}^{\mathrm{i}\beta x}\mathrm{e}^{-k_2 z} \qquad \text{for z>0} \tag{1.47a}$$
$$H_y(x,z) = A_1 \mathrm{e}^{\mathrm{i}\beta x}\mathrm{e}^{k_1 z} \qquad \text{for z<0} \tag{1.47b}$$

Since continuity requires $H_y(0,0_+) = H_y(0,0_-)$, we find $A_1 = A_2 = A$. Looking now at the E_x component[4]

$$E_x(x,z) = \mathrm{i}A\tfrac{1}{\omega\varepsilon_0\varepsilon_2}k_2\mathrm{e}^{\mathrm{i}\beta x}\mathrm{e}^{-k_2 z} \qquad \text{for z>0} \tag{1.48a}$$
$$E_x(x,z) = -\mathrm{i}A\tfrac{1}{\omega\varepsilon_0\varepsilon_1}k_1\mathrm{e}^{\mathrm{i}\beta x}\mathrm{e}^{k_1 z} \qquad \text{for z<0} \tag{1.48b}$$

where again continuity implies $E_x(0,0_+) = E_x(0,0_-)$ and thus

$$\frac{1}{\omega\varepsilon_0\varepsilon_2}k_2 = -\frac{1}{\omega\varepsilon_0\varepsilon_1}k_1 \implies \frac{k_2}{k_1} = -\frac{\varepsilon_2}{\varepsilon_1} \tag{1.49}$$

k_1 and k_2 are both positive for a confinement along z so ε_1 and ε_2 must be of opposite signs to guarantee this condition. As a consequence, surface polaritons (SPP) only exist at the interface between dielectrics and materials with negative permittivity such as metals below their plasma frequency or polar crystals in between their LO and TO phonon lines. For TE mode, continuity implies $A_1 = A_2 = A$ as well, however, the condition on H_x is $A(k_1 + k_2) = 0$ which is only fulfilled for $A = 0$ for confinement. As a result, there are no surface modes for TE polarization. Indeed, a wave close to a material with a negative permittivity with an electric field parallel to its surface will be reflected due to the mirror image.

Finally, if we insert the boundary condition Eq.1.49 inside Eq.1.46 we arrive at the dispersion relation for SPP supported by a single interface

$$\beta = k_0\sqrt{\frac{\varepsilon_1\varepsilon_2}{\varepsilon_1 + \varepsilon_2}} \tag{1.50}$$

An example of such dispersion is presented at Fig.1.8 for a metal modelled by a Drude model and air ($\varepsilon_2 = 1$) or silica ($\varepsilon_2 = 2.25$) as dielectric interfaces. As we discussed earlier, this dispersion curve exhibits two branches, an upper and a lower one. The upper polariton branch is inside the dielectric light cone and therefore corresponds to radiative states. At the opposite, the lower polariton branch consists of bound states, in this case surface plasmon polaritons (SPP). Between these two extremes lies a forbidden

[4] $E_x = -\partial_z H_y \frac{\mathrm{i}}{\omega\varepsilon_0\varepsilon}$ and $H_x = \partial_z E_y \frac{\mathrm{i}}{\omega\mu_0\mu}$ as provided from the curls of Maxwell's equations for a wave propagating along x.

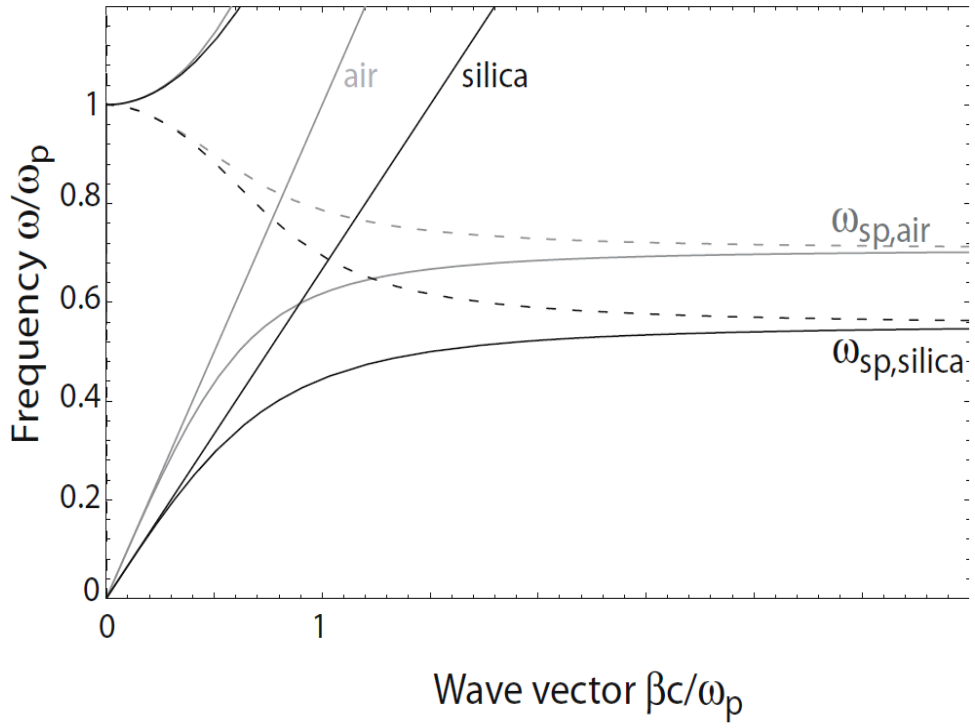

Figure 1.8: Dispersion curve of the propagation wavevector of SPP at the interface between a lossless Drude metal and air (grey lines) or silica (black lines). The interrupted lines are the imaginary part of the propagation wavevectors when they are purely imaginary, that is within the forbidden gap between the bulk ω_p and surface ω_{sp} plasmon frequencies. The frequency and propagation constant are normalized by the plasma frequency ω_p of the Drude function defined in Eq.1.34 (Reprinted from [3]).

gap for which the propagation wavevector is mainly imaginary. An important property of SPP is that since their wavevector is bigger than that of light the momentum mismatch needs to be compensated if one wants to stimulate them with EM waves. There are two main matching techniques, on one hand, prism coupling in which the wavevector of light is increased by the index of the prism [13, 14], and on the other hand, grating-assisted excitation where the periodicity Λ provides an additional momentum $G = 2\pi/\Lambda$. The dispersion curve for a real metal, here silver, is shown in Fig.1.9. One can observe two main differences with the ideal case, first, the existence of quasi-bound leaky states within the gap and second, a finite maximum wavevector which means a finite maximum confinement [3, 12, 15].

Two particular regimes are interesting for SPP: at low frequencies, the dispersion curve is close to k_0 which implies a low confinement, SPP behave thus as grazing-incidence light, also called *Sommerfeld-Zenneck waves*; at large wavevectors, the slope approaches zero and so does the group velocity, as a consequence SPP become electrostatic in nature at the frequency where $|\varepsilon_m + \varepsilon_d| \mapsto 0$. As an example, Tab.1.3 shows the characteristic lengths for the case of SPP at an interface between gold and air in the visible ($\lambda = 500$ nm) and in the infrared ($\lambda = 5\mu m$) where we have used the following relations (see Fig.1.10 for the definitions):

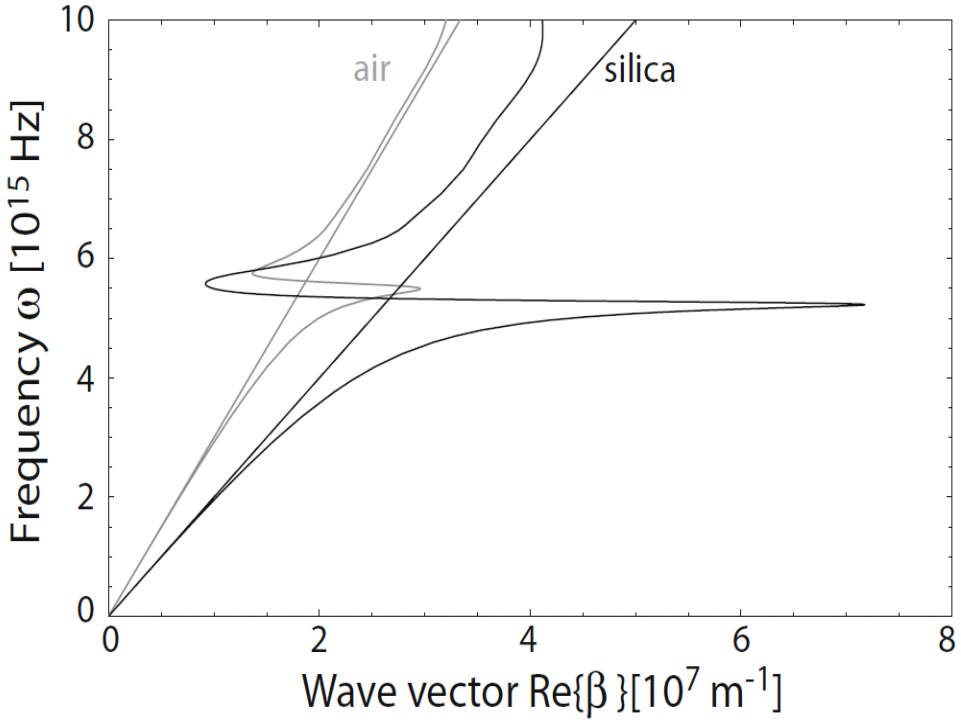

Figure 1.9: Dispersion curve of the propagation wavevector of SPP at the interface between silver and air (grey lines) or silica (black lines). Compared to the idealized dispersion plotted in Fig.1.8, one can note the finite maximum value of the wavevector for the case of a real metal and the presence of quasi-bound (because highly attenuated) states within the gap region (Reprinted from [3]).

	Visible	Mid-IR
Propagation length	10λ	1000λ
Confinement	$\lambda/5$	10λ
Skin depth	$\lambda/2$	$\lambda/100$

Table 1.3: Comparison of the characteristic lengths of SPP between the optical and mid-IR regimes

$$\text{Confinement:} \quad \delta_d = 1/\Im(k_z) \text{ with } k_z = \sqrt{k_0^2 - \beta^2} \tag{1.51a}$$

$$\text{Skin depth:} \quad \delta_m = 1/\Im(-\varepsilon_m k_z) \tag{1.51b}$$

$$\text{Propagation length:} \quad L = 1/\Im(\beta) \tag{1.51c}$$

SPP are very interesting because they are able to confine light in the direction perpendicular to the interface between the metal and the dielectric to a fraction of the wavelength. It permits thereby to design subwavelength waveguides which may be of particular interest for a new kind of computer chip technology for instance [3, 12, 15–17].

1.2.3.3. Localized surface polaritons (LSPP)

Compared to the large flat interfaces we discussed before, nanostructures exhibit large curvature as well as sharp features which induce scattering and thus can enable the coupling between EM waves and polaritons. Therefore there is no need of phase-matching techniques as in the case of SPP to excite LSPP. But before moving to the fascinating properties of localized SPP, we should briefly look at the more general problem of light scattering by a particle.

This problem has been addressed for more than one hundred years with the first theory by Lord Rayleigh concerned with small particles and later with the exact calculations of Mie for the case of homogeneous spheres. The latter's development is known as "Mie theory" which in turn has become a generic name for the phenomenon of light scattering by particles. Let's consider the situation where the particle is smaller than the wavelength, it allows to take the EM wave as a static electric field which greatly simplifies the problem, this is called the "quasi-static approximation". In addition, we will restrict the discussion to a sphere the symmetry of which removes meaningless complications. Since we are in an electrostatic situation, we can write the Laplace equation for the potential: $\Delta\Phi = 0$, from which the field can be calculated by $\mathbf{E} = -\nabla\Phi$. Assigning accurate boundary conditions we finally get

$$\Phi_{in} = -\frac{3\varepsilon_m}{\varepsilon + 2\varepsilon_m} E_0 r \cos\theta \tag{1.52a}$$

$$\Phi_{out} = -E_0 r \cos\theta + \frac{\varepsilon - \varepsilon_m}{\varepsilon + 2\varepsilon_m} E_0 a^3 \frac{\cos\theta}{r^2} \tag{1.52b}$$

with ε the dielectric function of the particle of radius a and ε_m the one of the surrounding medium. Recognizing in the second term of Eq.1.52b the dipole of the particle we can write

$$\Phi_{out} = -E_0 r \cos\theta + \frac{\mathbf{p}\cdot\mathbf{r}}{4\pi\varepsilon_0\varepsilon_m r^3} \tag{1.53a}$$

$$\mathbf{p} = 4\pi\varepsilon_0\varepsilon_m a^3 \frac{\varepsilon - \varepsilon_m}{\varepsilon + 2\varepsilon_m}\mathbf{E}_0 \tag{1.53b}$$

which gives for the polarizability defined as $\mathbf{p} = \varepsilon_0\varepsilon_m\alpha\mathbf{E}_0$

$$\alpha = 4\pi a^3 \frac{\varepsilon - \varepsilon_m}{\varepsilon + 2\varepsilon_m} \tag{1.54}$$

The interaction between light and a particle can then be described by the scattering, absorption and extinction cross sections of the particle. The scattering cross section describes the amount of light which is re-radiated by the particle and the absorption how much of it is dissipated mainly through heat. The extinction which quantifies the strength of the interaction between the light and the particle is the sum of the two former. At first order and for a spherical particle much smaller than the wavelength, the cross

sections read

$$C_{sca} = \frac{k^4}{6\pi}|\alpha|^2 = \frac{8\pi}{3}k^4a^6\left|\frac{\varepsilon-\varepsilon_m}{\varepsilon+2\varepsilon_m}\right|^2 \tag{1.55a}$$

$$C_{abs} = k\Im[\alpha] = 4\pi ka^3\Im\left[\frac{\varepsilon-\varepsilon_m}{\varepsilon+2\varepsilon_m}\right] \tag{1.55b}$$

$$C_{ext} = C_{sca} + C_{abs} \tag{1.55c}$$

For small particles, absorption is generally bigger than scattering while for big particles the contrary usually occurs.

Looking back at Eq.1.54, we note the resonance is achieved when $|\varepsilon + 2\varepsilon_m|$ is minimum. At best, it is zero leading to the Fröhlich condition for the case of a small or slowly-varying $\Im[\varepsilon]$ close to the resonance

$$\Re[\varepsilon(\omega)] = -2\varepsilon_m \tag{1.56}$$

we see it can be fulfilled for metals. The mode associated with this resonance is called a localized surface polariton; it is a non-propagating excitation. Changes in shape and size will affect the resonance spectral position and width.

The LSPP can be assigned a dephasing time – or in other words a lifetime – $\frac{1}{T_2} = \frac{1}{2T_1} + \frac{1}{T_2^*}$ which is related to the linewidth of its resonance by $\Gamma = 2\hbar/T_2$ where T_1 describes the decay time or population relaxation by both radiative and non-radiative path while T_2^* is a "pure dephasing time" accounting for the elastic collisions. Note the factor 2 in front of T_1 which arises because of the difference in definition between decay time (related to population relaxation) and lifetime (related to the quality factor). Apart from very small particle size, $T_2^* >> T_1$ and therefore $T_2 = 2T_1$. As the size increases, the radiative damping, which is the decay of LSPP into photons, raises due to retardation effects. These are due to a more and more pronounced phase delay across the particle volume which weakens the LSPP oscillations coherence and shrinks their lifetime consistently. The lifetime reduction leads eventually to a broadening of the resonance. Also, the restoring force decreases leading to a global redshift of the resonance. For very small size, there is a net increase of the absorption due to elastic scattering at the surface since the mean free path of the electrons exceeds the particle diameter. All these effects can be accounted by adding higher order terms to the polarizability. In most cases however, the first order is enough to catch the physics of the interaction.

Eventually, the occurrence of LSPP resonances give rise to the attracting property of a gigantic local electric field increase. The applications based on this near-field are numerous and range from surface-enhanced spectroscopy with SERS (surface-enhanced Raman spectroscopy) and SEIRA (surface-enhanced infrared absorption) to nonlinear optics and lasing. In addition, since the polarizability of LSPP is highly dependent on the surrounding medium, dielectric function changes in this one will shift the resonance; this effect is at the base of a new sensing technology [1, 3, 18–24].

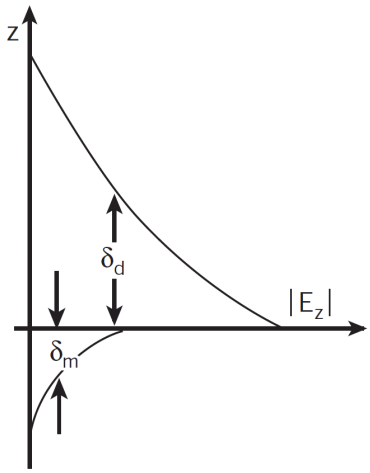

Figure 1.10: Definition of the characteristic lengths of SPP confined at the interface $z = 0$. The penetration of the field inside the metal or skin depth δ_m and the evanescent decay of the field away from the interface within the dielectric superstrate δ_d (Reprinted from [12]).

1.3. Methods

1.3.1. Numerical Algorithms

Mie theory and dispersion relations provide a basis to understand the behaviour of LSP and SP in very simple geometries, however they are far from sufficient to describe and solve more interesting and complex problems. These can only be analysed through the use of numerical techniques, which over the years and with the advances in computational power, have become essential tools in modern optics. Among those, Finite Difference Time Domain (FDTD) and Finite Element Method (FEM) are the most powerful methods in terms of flexibility despite being very demanding computationally speaking. Here, Lumerical was used as FDTD package and Comsol as FEM.

1.3.1.1. Finite Difference Time Domain (FDTD)

By far the easiest and most widely used method in computational electrodynamics, FDTD, which was developed in the 60's by Yee [25], solves numerically Maxwell's equations by discretizing the electric and magnetic fields both in space and time for the user-defined geometry, materials and boundary conditions. In this method, the electric and magnetic grids are shifted by half a grid-spacing and differences are taken at the central position in space. Then the derivatives of the fields are calculated by leapfrogs in time. First, the electric field is calculated and then after the set time-step the magnetic field is calculated and so on. This process is repeated iteratively until a steady-state solution is found. Fourier transforms can then be used to extract frequency spectra.

FDTD is a time domain method and therefore relies on the use of a pulse with a certain duration – it allows therefore to compute many wavelengths in a single run. This constitutes one of its biggest advantages, it also means that non-linearities can be implemented in a very natural fashion. However, this requires the material properties to be defined for each frequency within the pulse; the pulse being continuous a function must then be found to fit the permittivity and permeability of the media. In consequence, strong dispersion can cause troubles in FDTD and one should always assure appropriate fitting in a wavelength range larger than that of the defined pulse and avoiding poles.

Another key element which is common to both FDTD and FEM packages is that it is volume based. A source must be defined, as well as the geometry or scatterer, all this enclosed within a simulation volume. This is one of the reasons for the high computational demand, the computation power scales with the total volume not the surface. In addition, the generated wave might bounce off the simulation border which would create artefacts. Several tools exist to circumvent this problem. First, one can use Perfectly Matched Layers (PML) at the border of the simulation, which consist of widely absorbing material preventing any reflection. Other means to truncate the need for infinite space is to define scattering or impedance boundary conditions, where one can either set a specific scattered strength or the impedance of the boundary.

Last, because of the method FDTD uses to calculate the EM fields, the grid, or mesh, needs to be rectangular. This is probably the worst limitation of the technique as the presence of small geometric or contrast details will pin down the mesh size within the whole simulation volume [26, 27].

1.3.1.2. Finite Element Method (FEM)

A typical alternative to FDTD is FEM. There the electric and magnetic fields are defined by a local function for each mesh element and solutions are sought which fulfil user-defined boundary conditions as well as Gauss's law and continuity of the tangential fields. Each mesh element is a spatial discretization of Helmoltz's equation which does not impose constraints on their geometry. Therefore, FEM packages allow a great freedom during the meshing procedure, often tetrahedral based and with multi-scale refining; thus any arbitrary and complex shapes can be very accurately resolved without undermining the global simulation size. This is certainly the main appeal of finite element methods. In addition, most CAD files can be imported nowadays giving rise to unprecedented control over the geometry.

Originally, FEM were limited to frequency domain calculations. It meant that no fitting of the material properties was needed but complete spectra were very time consuming as the frequency had to be swept across the desired range and with the desired step. Since a single FEM simulation is more or less comparable to a single FDTD calculation in terms of computation power and time this still represents a major drawback of the former technique. Nevertheless, it produces markedly more accurate results than FDTD and is far more flexible.

Later developments brought time-domain capabilities to FEM packages. However, these implementations either suffer from the same mesh limitation than FDTD softwares or are extremely computationally demanding [26, 27].

1.3.2. Experimental Techniques

Three techniques have been used regularly along this thesis and most presented results were obtained through one or the other. Therefore we review here the basic mechanisms behind Fourier transform infrared spectroscopy, dark-field spectroscopy and Raman spectroscopy.

1.3.2.1. Fourier-Transform Infrared Spectroscopy (FTIR)

Fourier transform infrared spectroscopy (FTIR) is a very common and useful technique to characterize the absorption properties of a given sample in the infrared. Nowadays, it is available for far-infrared, mid-infrared and even near-infrared, the differences being mainly limited to the hardware such as the beamsplitter, the lenses, detectors, filters, etc. Indeed, the physics involved always stays the same and relies on two essential components, on one side an interferometer, and on the other side the Fourier transform computation.

The interferometer is of Michelson type, it consists of a beamsplitter (M0) and two mirrors (M1, M2), one being mobile (M1), see Fig.1.11. The displacement of the mirror induces a path difference $2x$ which leads to interferences between the two beams. As x is changed, the total intensity at the exit of the device is $I(x) = S(\bar{\nu})\cos(2\pi\bar{\nu}x)$ where the maximum is reached when $2x = n\lambda = n/\bar{\nu}$ with n integer; $S(\bar{\nu})$ is the spectral lineshape of the source. The displacement of the mirror is measured by a laser, and it is its accuracy that determines the spectral one. Then the beam is passed through a sample and the resulting spectrum is the intensity as a function of the mirror position. Obviously, the desired spectrum should be a function of the wavelength and it is at this step that the Fourier transform (FT) is used. Since the mirror positions are sampled by the laser rather than continuously measured, we make use of a discrete FT to access the spectrum

$$S(k\Delta\bar{\nu}) = \sum_{n=0}^{N-1} I(n\Delta x)\exp(\mathrm{i}2\pi nk/N) \tag{1.57}$$

where the continuous variable x and $\bar{\nu}$ have been replaced by $n\Delta x$ and $k\Delta\bar{\nu}$. Measuring the transmittance of a sample is now straight forward and is simply obtained by dividing the intensity passed through it by a background sample-free one which sets the 100% transmission; reflectance is measured in the same way apart from the background which is usually a metal mirror that sets the 100% reflection baseline. It is not necessarily clear why using such a technique rather than simply measuring the intensity via monochromator for each and single wavelength. Actually, FTIR is much faster than monochromatic measurements because it allows to probe the whole spectrum at once, it is therefore time-saving which is of great advantage when we realize that experimental spectra are usually averaged over thousands of measurements. Also as said before, the spectral resolution is set by the mirror displacement measurement so does only have the laser wavelength as a limit. Moreover, the signal-to-noise ratio is improved during a multiplex (*i.e.* broadband) measurements compared to a monochromatic measure because of the absence of a slit which limits the collected power, this is known as the Fellgett's advantage [28].

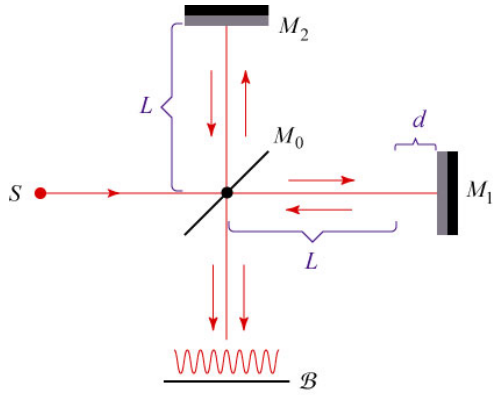

Figure 1.11: Michelson interferometer: Light originating from the source S is sent along two paths through the beamsplitter M_0 and made to interfere with itself upon reflection on mirrors M_1 and M_2. The resulting interferogram measured on detector B can then be sampled in phase via a difference in path lengths d generated by the mobile mirror M_1.

Measurements on nanostructure arrays reported here were mostly performed through a FTIR microscope (Bruker Hyperion 2000) coupled to a FTIR unit, or bench (Bruker Vertex 70). A schematic of such apparatus is shown in Fig.1.12 where the microscope is connected to output 2. A diagram for the microsope itself is presented in Fig.1.13. A microscope gives a considerable advantage over the bench as it allows measurements both in transmission and reflection mode, the use of polarizers and filters in excitation and collection and obviously the magnification which is essential for the measurement of samples prepared by lithography. Furthermore an aperture can be inserted in the back focal plane with a selection down to around $10 \times 10\mu\text{m}^2$. It is finally important to mention the fundamental elements which are the objectives. Indeed, as common as they might be, they are Cassegrain objectives which is critical for some results presented later on. Fig.1.14 presents schematically the path taken by light in such objective. As one can see, although the setup is at normal incidence, the light is not collimated but comes in a finite solid angle. For our 36× objective the weighted angular average is for instance around 25°.

Mid and near-infrared (MIR and NIR) spectra were obtained with the use of a liquid nitrogen cooled MCT (mercury-cadmium-telluride) detector, a Ge-KBr beamsplitter and a heated ceramic element as thermal source. NIR measurements could alternatively be taken by combining a Pelletier-cooled InGaAs detector with a quartz beamsplitter and a tungsten lamp. Spectra in the visible range, although at the limit of the FTIR capabilities, were measured with a Si diode.

1.3.2.2. Dark Field Spectroscopy

Very often in plasmonics, one is concerned with the extinction of single objects rather than the collective and averaged optical response of arrays. In that case, a FTIR is not helpful and one can turn to dark-field spectroscopy. This technique mostly relies on the use of a dark-field objective where the incident light

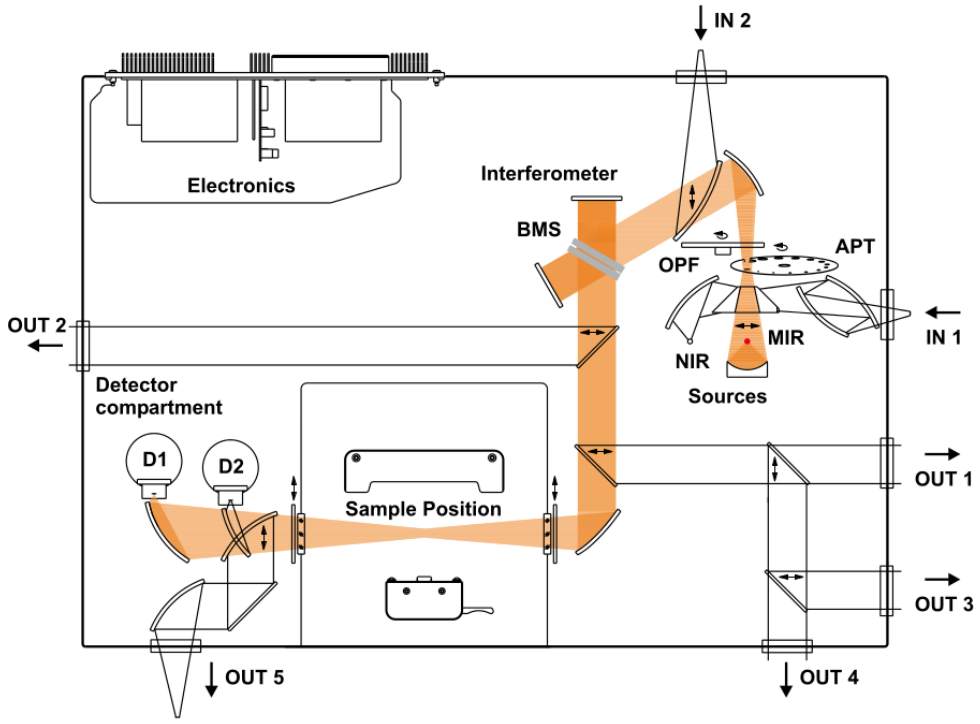

Figure 1.12: Schematic of the Bruker Vertex 70 FTIR bench. The assembly in the top right region generates an interferogram via the Michelson scheme presented in Fig.1.11 with a tunable source (near or mid-infrared) which is then passed through a sample and detected with $D1$ or $D2$ depending on the source (www.bruker.com).

comes at very large angle and only shallow angles are collected, see Fig.1.15. Flat surfaces will appear then dark while scatterers are bright. Despite being based on conventional optics and therefore limited by diffraction, dark-field setups are normally combined with an avalanche photodiode (APD). This permits to scan the sample and locate scattering objects, the collected light is then sent to a spectrometer for an integration of the intensity in function of the wavelength, *i.e.* obtain the scattering cross-section. An alternative to the dark-field objective is to use a side illumination and a normal objective for collection. This gives more freedom as both the angle of excitation and polarization can be controlled.

1.3.2.3. Raman Spectroscopy

Raman spectroscopy is often considered as being complementary to infrared spectroscopy because the selection rules for the excitation of the vibrational modes are different. In the latter, there must be a change in a the dipole moment of the molecule during the vibration in order to allow an interaction with the incident field. At the contrary, it is the polarizability which should vary for a vibrational mode to be Raman active, see Sec.1.2.2.1 and Fig.1.16. Another important difference between IR and Raman spectroscopy is that IR absorption is measured through the interaction between an incident field and the molecule (as it involves the dipole moment) while Raman scattering is an inelastic event in which the excited molecule loses or gains energy before re-radiating the incoming field. This can be more clearly

visualized by considering the energy diagram of a molecule, see Fig.1.17. There the incoming photon (in blue) can be either elastically scattered by the molecule, in which case Rayleigh scattering occurs or inelastically scattered (blue or redshifted) in which case (Anti-Stokes or Stokes) Raman scattering is taking place. Since it involves vibrational states of the molecule Raman spectroscopy can be seen as probing its phonon spectrum [6].

Raman scattering is performed with lasers (monochromatic light) as one needs to analyse the scattered light at energies close to the incident one. It therefore requires a combination of a notch filter and a spectrometer in order to detect very slight changes in energy. Due to the very low yield of the process, one is in addition often forced to use incident powers close to the damage threshold of the samples as the effect increases linearly with the intensity of the light. Raman and AFM measurements were mostly performed using a WITEC Confocal Raman Microscope alpha300R.

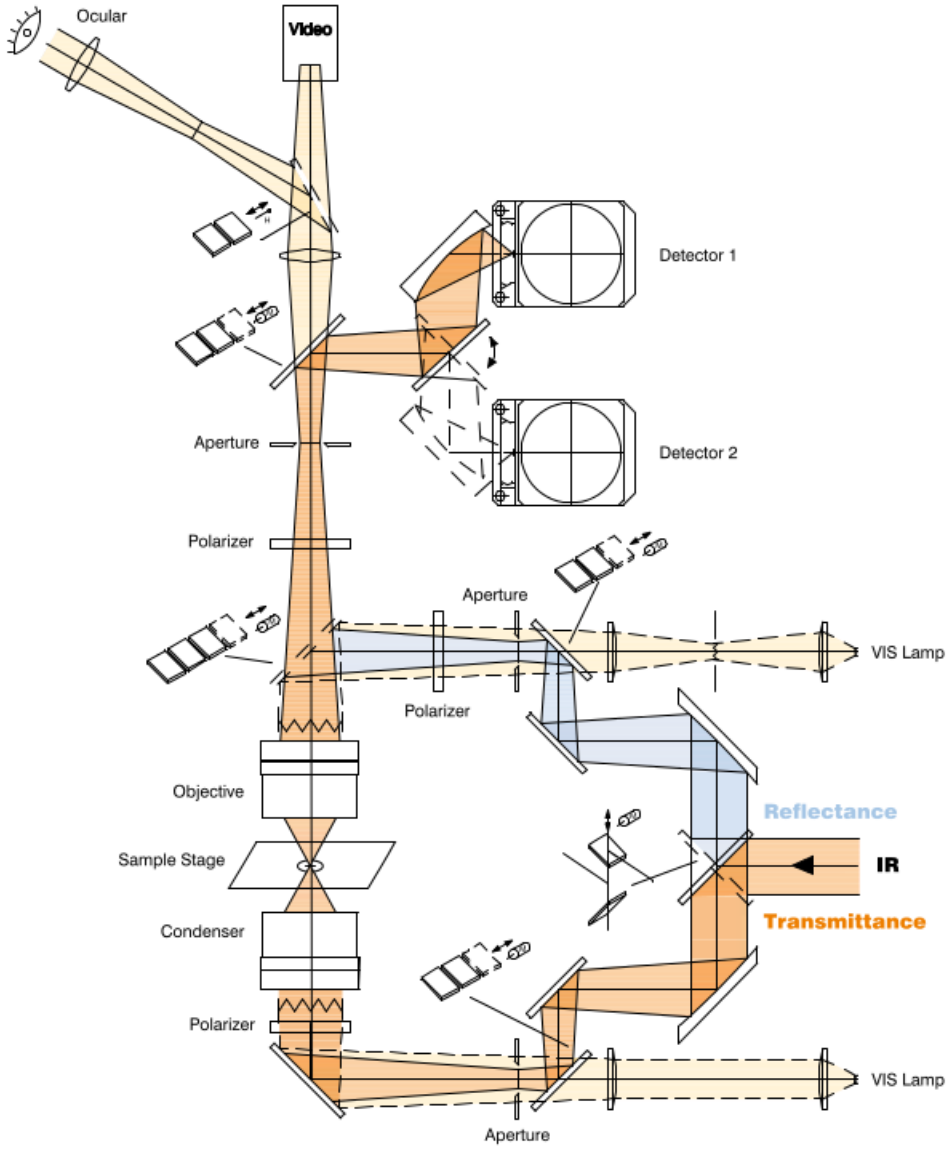

Figure 1.13: Schematic of the Bruker Hyperion 2000 FTIR microscope. The infrared interferogram generated by the FTIR bench is output through $OUT2$ in Fig.1.12 and directed within the microscope either in reflection (blue path) or transmission (orange path) towards the sample. A microscope offers the great advantage of supporting polarizers and/or filters at both illumination and collection (www.bruker.com).

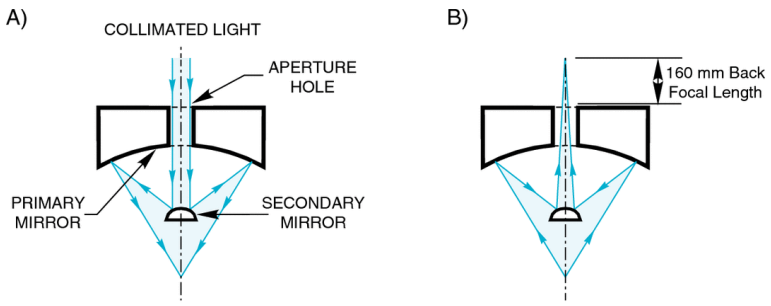

Figure 1.14: Light path in a Cassegrain type objective. One can see that both diverging and collimated light strike the object plane as a solid cone and therefore can never be considered as normal incident.

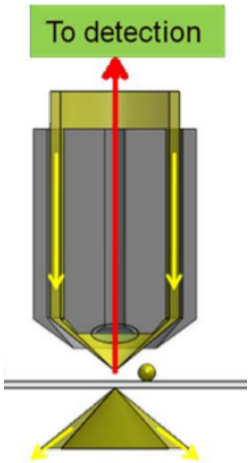

Figure 1.15: Light path in a dark-field objective. The illuminating light (yellow arrows) is incident at very large angles on the sample surface and only shallow angles (red arrow) are collected back by the objective. Therefore scatterers appear bright while flat surfaces are dark (Reprinted from [29]).

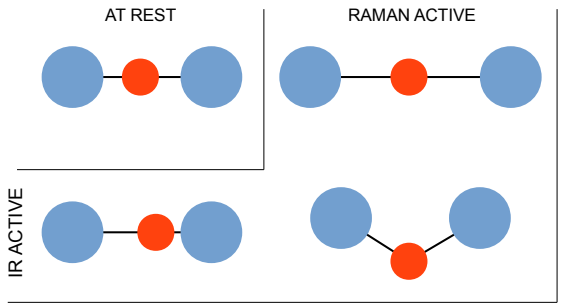

Figure 1.16: Example of IR and Raman active vibrations for a small polyatomic molecule. The molecular vibration must exhibit a change in the dipole moment to be IR active (that is if the centre of charge is displaced) while it must modify the polarizability to produce Raman scattering (that is if the electron cloud change in shape).

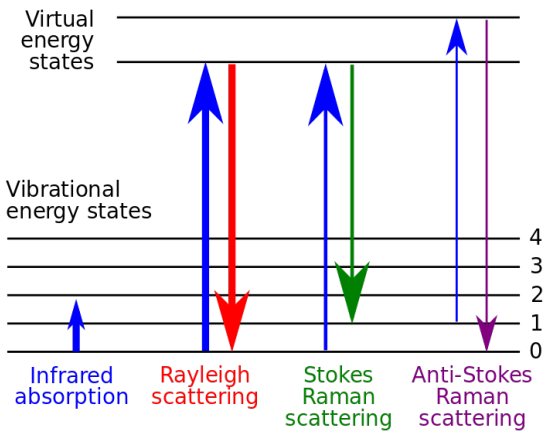

Figure 1.17: Differences between IR, Rayleigh and Raman processes. Rayleigh scattering consists in an elastic event in which the scattered wave has the same energy than the incident; infrared absorption is caused by a direct increase in vibrational energy; Raman scattering occurs if the incoming field gains or loses energy when interacting with a vibrationally excited or unexcited molecular system (en.wikipedia.org).

1.4. Motivation

The main motivation for this thesis was to investigate new materials for applications in plasmonics and metamaterials. As we will discuss below those fields, despite promising results, are strongly limited by losses and available geometries. As possible alternatives we investigated on one hand nanostructures obtained by self-assembly such as gyroids and octapods and on another hand materials with similar optical properties to metals but with reduced losses and operating at frequencies beyond the visible range such as SiC and graphene.

1.4.1. New Frequencies

Metal plasmonics has encountered considerable success in the visible range, enabling single molecule detection via surface-enhanced Raman scattering [30] and is also a key instrument in fluorescence measurements and in the control of nanoemitters [24, 31]. The visible is also crucial because of vision and in consequence its importance in modern technology should not be ignored. Nevertheless, other frequency ranges would benefit highly from the field confinement properties of metals such as microwaves to reduce the size of antennas for telecommunication, far and mid-infrared for molecular sensing, terahertz for security applications, not to mention the Telecom wavelength 1.55μm used in optical telecommunication at which fibres have minimal losses. Because of their Drude dispersion, the losses in noble metals increase rapidly away from their plasma frequency. The useful spectral range of metal plasmons is therefore limited to the visible and near-infrared.

Luckily, the plasma frequency is directly dependent on the number of free carriers, see Eq.1.34, and in consequence one simply needs to tune the carrier concentration to sweep the frequency axis. This is further illustrated in Fig.1.18, where the LSPR frequency of a spherical nanoparticle is located within the visible down to the microwave by changing the material from metal to low doped semiconductors. This

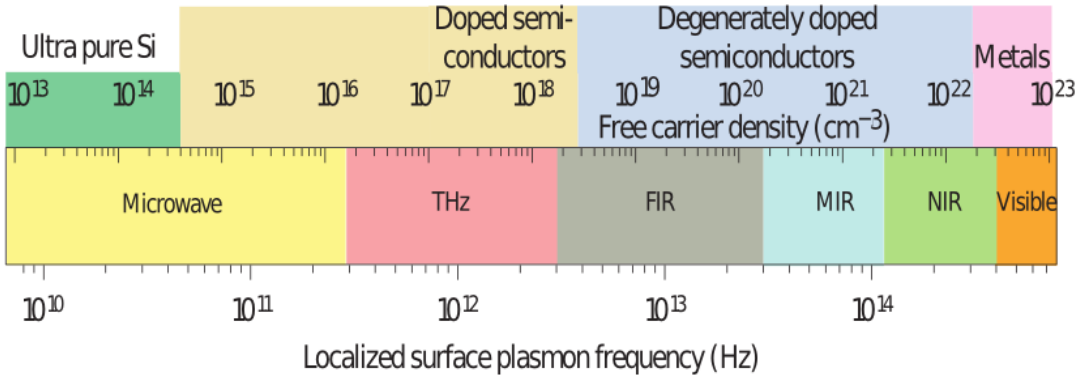

Figure 1.18: Estimated localized surface plasmon resonance (LSPR) frequency of a small spherical nanoparticle in the quasi-static limit depending on its free carrier concentration (Reprinted from [32]).

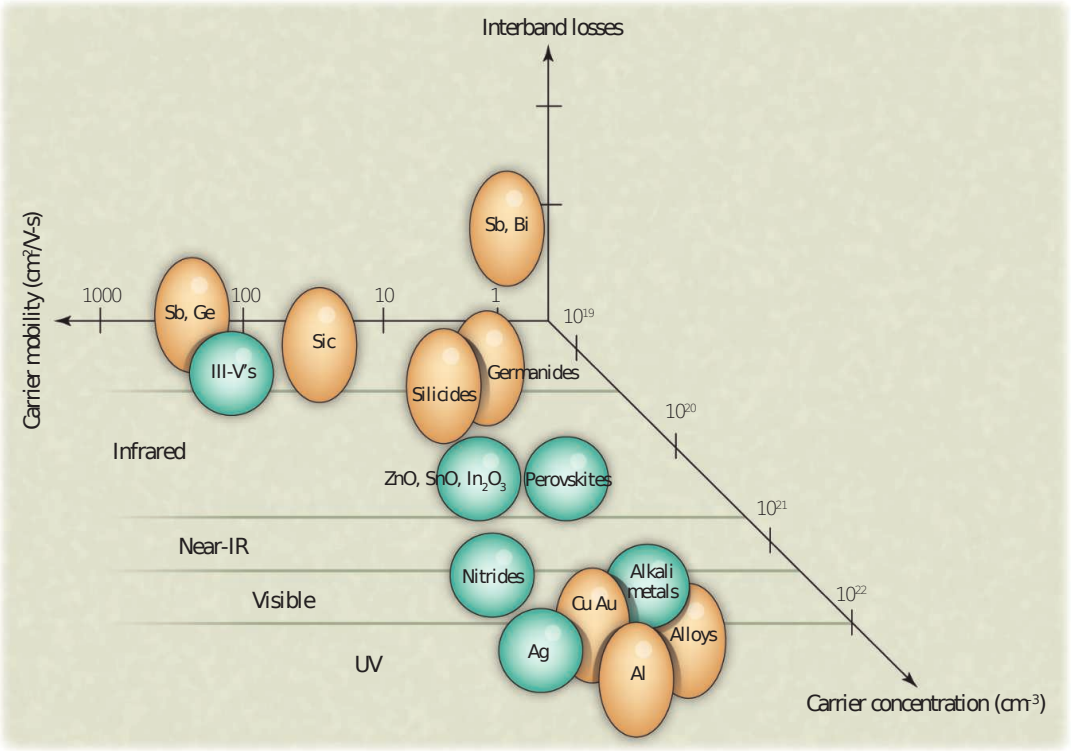

Figure 1.19: Carrier concentration, carrier mobility and interband losses for different categories of material. Elongated bubbles stand for higher interband damping (Reprinted from [33]).

discussion however does not consider the intrinsic losses of those materials, see Fig.1.19. A careful analysis considering both scattering time (or mobility) and interband absorption suggests the most promising semiconducting materials are silicon carbide, III-V semiconductors such as InSb or BN or graphene, as we will discuss later on. Semiconductors offer in addition a large tunability over metals through doping [33–35].

There is an interesting alternative to plasmons though, relying on the optical phonons existing in polar crystals. Indeed, the confinement of electromagnetic fields is in this case achieved through the interaction with the charged lattice vibrations which do not suffer from Ohmic losses. Scattering times are therefore markedly increased leading to significantly stronger resonances. Furthermore, since those excitations only exist in highly crystalline materials, the material quality tends to be dramatically better than for conductors – which tend to be highly polycrystalline in most cases – improving further the scattering rate. An example of such a material is silicon carbide, where the difference in electro-negativity between the silicon and carbon atoms results in a non-zero polar moment for transverse optical phonon modes, which we will discuss in details later. Fig.1.20 shows the strong local field which can be obtained with optical phonons in SiC compared to plasmons in Au or Ag. It is clear that optical phonons are a promising alternative to metals or semiconductors as they exhibit much larger field concentration capabilities combined with extremely narrow (and in consequence long-lived) resonances. Furthermore, these are ideally located in the mid-infrared range where most molecules have specific absorption spectrum

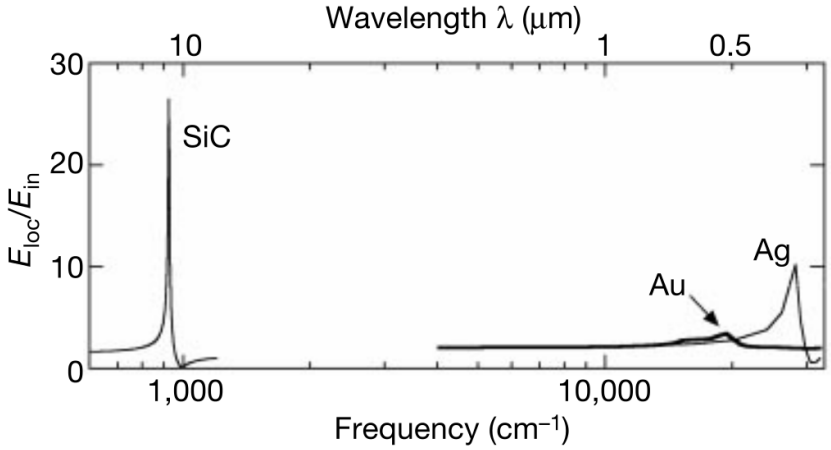

Figure 1.20: Local field enhancement from phonon polaritons in polar materials such as SiC compared to plasmon polaritons in metals, here Au and Ag (Reprinted from [36]).

and are thus appealing for molecular detection. It should be noted however, that optical phonons only exist in a limited frequency range which is fixed and given for every materials. Additionally, polar crystals are extremely hard materials, SiC in particular is the second hardest material after diamond. The implementation of nanostructures out of those is thus still experimental but the advances in growth and patterning, as the results we report here prove, are very encouraging.

1.4.2. New Geometries

Because the shape of a nanosystem has a direct influence on its properties its control is of prime importance in order to obtain a nanostructure with a desired and specific behaviour. Very often it is as much due to the use of a new physical effect or paradigm than a cleverly designed device that new functions or applications can be enabled.

So far, most proofs of concept have been obtained through nanofabrication. This ensemble of techniques including lithography and etching allows a precise design of nanostructures down to tens of nanometres. These physical methods are convenient and provide excellent control over the shape and feature size, and their use supports and governs the whole semiconductor industry. However, the sample extents are limited to $100\times100\mu\text{m}^2$ for e-beam lithography which offers the finest resolution. Another downside is the strictly planar character of the geometries achievable. Finally it is expensive to maintain and relies on costly equipment. It is rather flexible in terms of base materials, but is impossible to scale up due to the costs and is extremely time-consuming.

An alternative to physical methods is self-assembly. Deriving from colloidal chemistry, the principle is that under specific conditions it is possible to control the way molecules assemble. Two such examples are reported here, namely the self-assembly of block copolymers to produce double gyroid structures and CuS/CuSe nanocrystals, in which growth at the faces can be favoured leading to octapods. Since the building blocks are molecules, the smallest features and resolution can be sub-nanometric promising fantastic opportunities for new structures. In addition, the assembly is intrinsically three-dimensional and therefore fundamentally new ways for designing nanostructures are accessible. Despite these very attractive properties, self-assembly requires careful studies of the chemistry of a system which can take extensive efforts. Nevertheless, when the specific growth conditions are known, large numbers of samples can be fabricated and in consequence this is the most promising fabrication method in nanotechnology for industrial applications. Last, a fundamental aspect of self-assembly which is often overlooked is that it is a spontaneous process. This means it is highly subject to thermodynamic fluctuations and randomness. Because of this, the yield of self-assembly and the homogeneity of the produced samples are low and this is probably the reason for our failure to measure the properties of the octapods and gyroids fabricated by our collaborators.

2. New Materials for Surface Plasmon-like Modes

2.1. Review and Applications of Plasmonics

2.1.1. From Surface Science to Nanotechnology

The study of plasmonics started with the investigation of corrugated metallic surfaces and in particular the report of grating anomalies by Wood in 1902 [37] although this effect and the role of surface plasmons in it is still a matter of debate nowadays. Other important steps in the rise of plasmonics was the report by Ritchie in the 50's [38] of the energy spectrum of thin metallic foils and the subsequent development of methods to excite these surface waves by Otto [13] and Kretschmann and Raether [14]. This led to thorough studies of the role of corrugation on the generation of these waves and has been a powerful technique since the 70's to study the morphology and quality of surfaces [15]. With the advances in nanofabrication and specially e-beam lithography there has been a dramatic surge of activity in the past 20 years dealing with nanostructured metals [39]. While the confinement effect of plasmons was known from the 60's the ability to design nanostructures at will has permitted a variety of novel effects to be probed and for some even applied to devices. We describe below a few of those applications with a particular focus on sensing which is an important prospect in the results we present here.

2.1.2. Applications: Pregnancy Test and Beyond

Aside from stained glasses found in cathedrals, in which the colours are often caused by the plasmon resonance of metal colloids, plasmonics has been used or proposed since then for many applications.

2.1.2.1. Recurrent Sensors

Sensing is to date one of the most successful applications of plasmonics with commercial devices, such as pregnancy tests, available from the early nineties. Most of the work is focused on LSPP or SPP peak position shift though. However, the direct observation of chemical absorption spectra is also possible by the mean of surface-enhanced spectroscopies which are based on field enhancement.

Conditions for the excitation of a SPP are tight and therefore the launching of such surface waves will appear as a sharp dip in both reflection and transmission measurements. As can be seen from Eq.1.50

its spectral position depends on ε_2 the dielectric function of the adjacent medium and any change in the latter will produce significant shift in the position of the peak [3, 40–42]. The advances in colloidal chemistry have made the fabrication of nanoparticles with narrow size distribution routine procedure and the LSPP resonances are also commonly used for sensing. Indeed, the polarizability – see Eq.1.54 – of the nanoparticles is very sensitive to changes in ε_m and similarly to SPP-based sensing, the measurement is taken as a spectral shift of the resonance peak [3, 20, 43–46]. Both methods prove to be very similar in terms of efficiency when the sensitivity, linewidth and filling factor are all taken into account and therefore the use of one or another method will mainly be decided regarding practical aspects such as the device fabrication, handling and use. However, they are only sensitive to the change in the refractive index, and any chemicals spatially close will be detected. Therefore they highly rely on chemical binding at the surface for providing specificity to the sensing process. This is a main drawback since it usually requires dedicated studies of the surface chemistry between the molecules of interest and the active layer. The sensitivity is directly dependent on the width and strength of the resonance which explains why Fano resonances are studied extensively in this context [3, 20, 41–48, 48].

Based on a very different mechanism surface-enhanced spectroscopies (SES) use nanostructures or even surface roughness to concentrate locally the incident field leading to a dramatic increase of the analyte cross-section [49–52]. Surface-enhanced Raman scattering (SERS) started with the pioneering work of Fleishmann, Hendra and McQuillan on pyridine adsorbed at a silver electrode [53] in 1974. Explanations were given three years later by on one side Jeanmaire and Van Duyne for the chemical effect [54] and Albrecht and Creighton on another side for the electromagnetic mechanism [55]. First surface-enhanced infrared absorption (SEIRA) measurements were then reported by Hartstein and co-workers in 1980 [56]. SEIRA and SERS are both of technological interest since their cross-section is extremely small compared to Rayleigh scattering or fluorescence for instance. Indeed, the Raman and IR signal of molecules are genuine fingerprints and therefore central for biology but also chemical identification. Nowadays, a crucial application is that of explosives detection. Research focus then on nanostructures which exhibits strong hot spots at high densities like the ones provided through bottom-up fabrication with molecular sized features. Nanostars or their 3D equivalent the octapods are therefore highly appealing thanks to their sharp and numerous tips which act as hot spots [3, 20, 21, 31, 43, 57].

Next we briefly describe the two enhancement processes at the basis of SES. The first chemical effect is a dynamic charge transfer between the metal and the molecules which changes the vibrational polarizability of the latter. The second aspect is related to the orientation of the molecular dipole, which will be enhanced at most when it is perpendicular to the surface metal, *i.e.* directed along the electric field lines. Because the space average of $\cos^2\theta$ is $1/3$, preferentially oriented molecules will then be three times more enhanced than randomly oriented ones. Altogether, the chemical effects are several orders of magnitude lower than the electromagnetic effect and only concerns molecules that are chemisorbed on the metallic surface [51, 52, 54, 58–64]. The second mechanism is electromagnetic. On one side the lightning rod effect, that is to say the crowding of the electric field lines at the metallic surface, gives rise to an intensification of the field which becomes more and more spectacular as the particle spacing diminishes, see Fig.2.1. In addition to this process, the localized plasmon resonances in the metal nanoparticles reinforce drastically the local electric field intensity. However this last effect will decrease fast away from

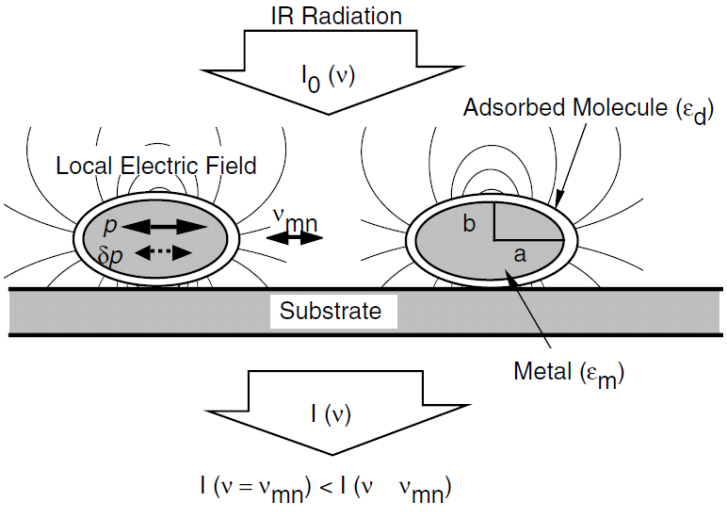

Figure 2.1: Schematic diagram of the electromagnetic effect in surface enhanced spectroscopy. An infrared radiation excites LSPP resonances in metallic nanoparticles with oscillating dipole p which generate strong local field much enhanced compared to the incident intensity; the local field is further increased because of the lightning rod effect. A molecular species adsorbed on the metal with a vibrational line at frequency v_{mn} will absorb the radiation in proportion to the local rather than incident intensity leading to a drastic decrease in the transmitted light. Moreover, the strong induced dipole moment of the molecular layer δp at v_{mn} will act as a perturbation to the metal LSPP response hence creating an additional channel for the enhancement of the molecules cross-section (Reprinted from [51]).

the metal surface due to the confinement of the LSPP. We can see that the LSPP resonance occurs in the visible but its tails extends deep into the infrared where it also contributes in SEIRA, see Fig.2.2. The huge electric field will increase the number of scattering and absorption events; above all it will perturb strongly the molecule dipole moment. In turn, the latter will be an additional perturbation for the metal dielectric function. Since the perturbation is particularly strong at vibrational frequencies, the metal will be more perturbed at these specific wavelengths than at others; the metal will therefore act as an amplifier of the molecule spectrum. Generally, reported enhancement are much higher for SERS (10^6-10^{14}) than for SEIRA (10^1-10^3) but this mainly comes from the fact that typical plasmonic resonance occurs in the visible at which range the Raman scattering takes place while IR absorption only benefits from the much weaker tails of these resonances, see Fig.2.2 [20, 43, 49, 51, 55, 58, 65, 66]. To circumvent this limitation Pucci et al. have fabricated nanorods with resonance in the infrared [67] and have indeed reported a much better SEIRA signal when covering them with molecules [68]. Further works in the infrared with antenna arrays [69] and with near-field spectroscopy [70] confirmed the interests that can present such technique.

2.1.2.2. Towards Nanoguidance

Because they are able to squeeze free space light into sub-diffraction volumes, plasmons have been proposed as an ideal mediator between photonic components such as optical fibres and electronics [12,16,17].

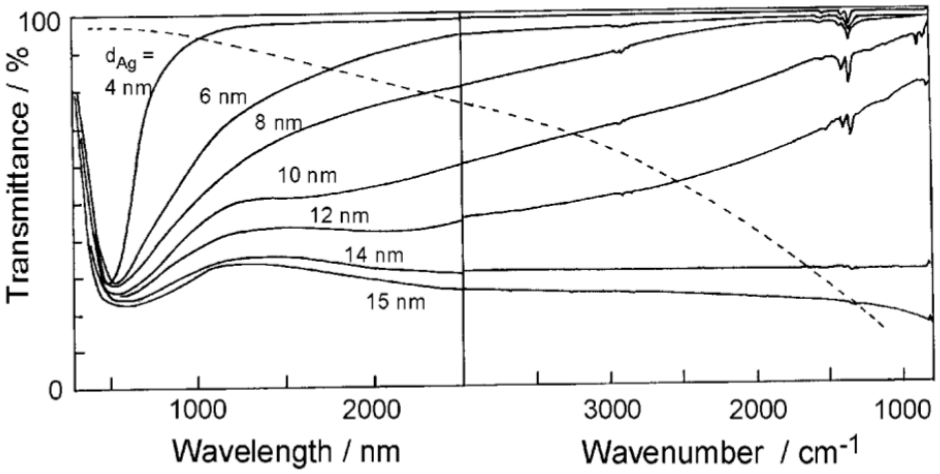

Figure 2.2: LSPP resonances of silver islands in the visible with tails extending deep into the infrared. d_{Ag} is the thickness of the metal island film (Reprinted from [51]).

They are even considered for nanosized logical elements. The proof of principle has already been demonstrated and relies for instance on nanoparticles to localize light and increase its wavevector before coupling this local field into a plasmonic waveguide, which can be a simple stripe or more complicated like gap plasmon or v-shaped waveguides, see Fig.2.3 for an example. Unfortunately, while plasmon circuitry ben-

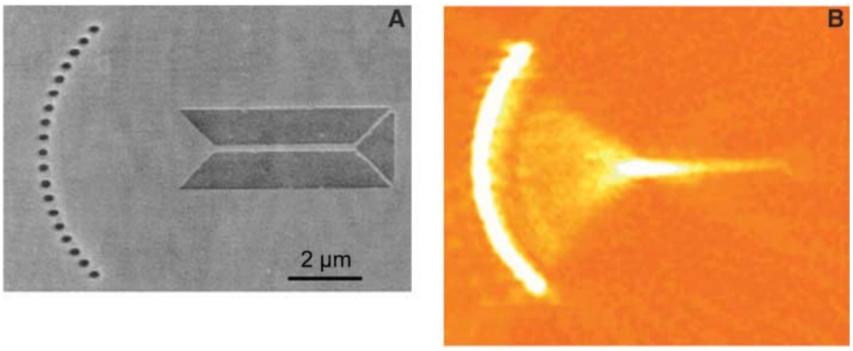

Figure 2.3: Coupling device between light and SPP. A) SEM image showing a lens composed of silver anti-dots (*i.e.* a perforated metal plate, dark is empty) and a 250 nm-wide stripe waveguide. B) Scanning near-field optical microscope (SNOM) image of the operating device. The constructive interference between the launched SPP modes originating from the individual anti-dots results in a convergent "beam" directed towards the sub-diffraction waveguide. (Reprinted from [16]).

efits from higher operating speed, which is the main limitation of current electronics, it must rival with a predominantly silicon-based technology with which it can be poorly integrated. Moreover, plasmonics suffers from its eternal trade-off between propagation and confinement.

2.1.2.3. Photothermal Therapy and Microbubbles

An interesting application for plasmonics is that of heating at the nanoscale. Indeed, although plasmons are intrinsically lossy due to Ohmic losses, this can be used to our advantage by considering the temperatures which can be reached in the vicinity of nanoparticles, see Fig.2.4. Despite the small increase in

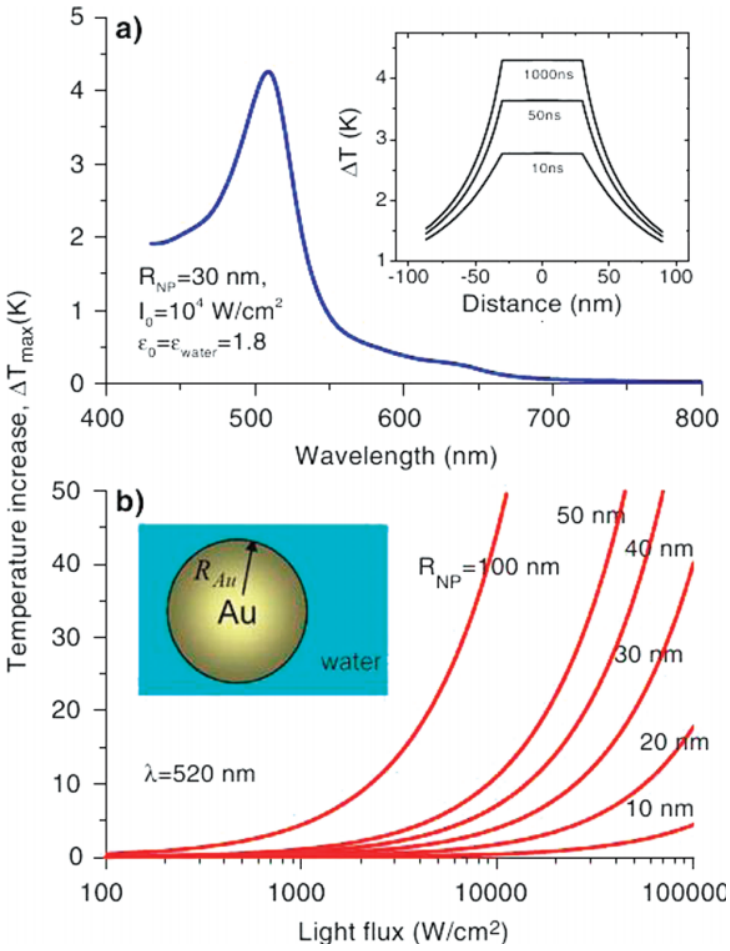

Figure 2.4: a) Spectral and b) size dependence of the local temperature increase near gold nanoparticles in water. The inset in a) shows the increase of temperature over time (Reprinted from [31]).

temperature, this proves an effective way of killing cancer cells as those are more fragile than normal ones. It helps in addition to decrease the radiation dose needed for photothermal treatments [31]. The strong absorption of core-shell nanoparticles placed in water can even be combined with a solar concentrator to produce steam which can be used for sterilization purposes [71–73].

2.1.2.4. Emerging Technologies?

It was proposed back in 2003 by Stockman and Bergman [74] that a plasmonic nanoparticle embedded in a gain medium could act as a nanolaser with almost no threshold. Results presented by Noginov, Shalaev

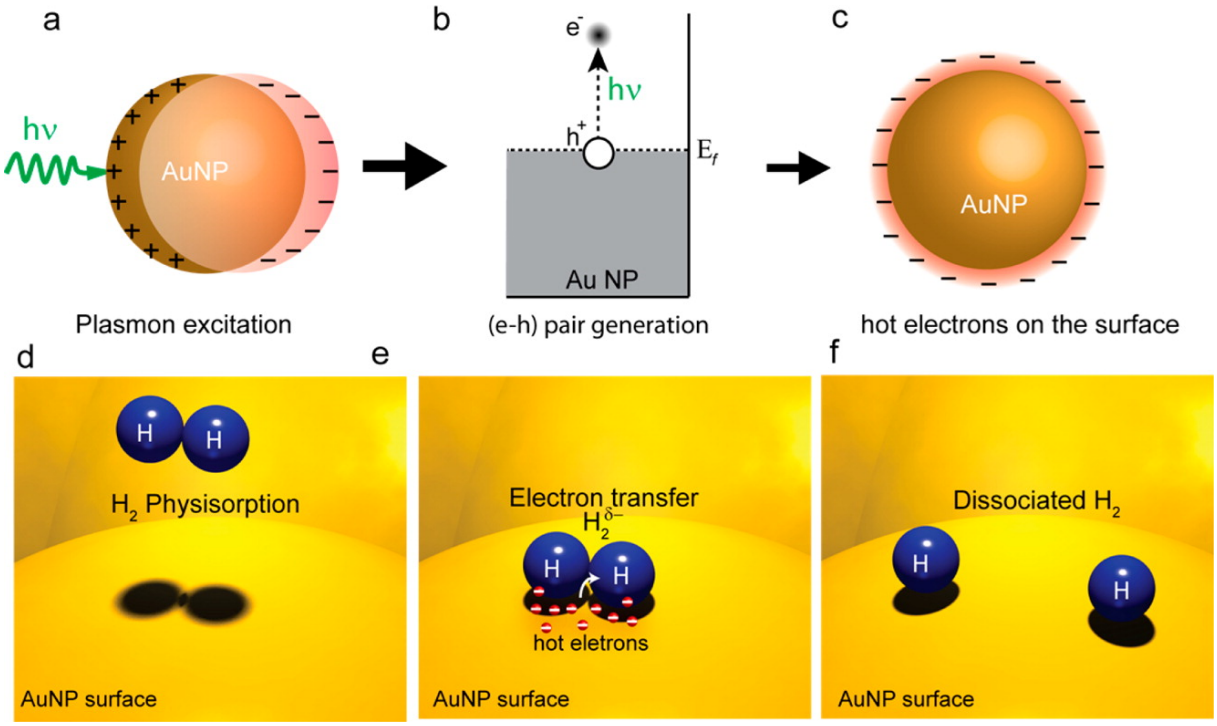

Figure 2.5: Scheme of a hot electron being transferred from an excited NP leading to hydrogen dissociation. a) The incident light excites a LSPP b) which will decay in part through electron-hole pair formation c) creating thereof a distribution of hot carriers at the surface of the metal for a very short time. d) If a molecule happens to physorb at the surface, such as H_2, during that period of time e) the hot carriers can tunnel to the molecule affecting its chemical potential f) which could lead to dissociation (Reprinted from [76]).

and Wiesner [75] tend to confirm such a device could be made and operate as expected. Potential applications are vast if fabrication and control of such a system is achieved ranging from medicine to nanotechnology.

It has been known for a long time that metallic ions can affect considerably chemical reactions. However, with the ability to tune plasmonic particles finely, researchers are reporting their strong photocatalytic properties. It is still unclear however if this activity is due to simple near-field heating which would decrease the activation energy of the reactions or hot electron transfer which would lead to molecular energies reorganization, see for instance Fig.2.5. Whatever its origin, the photocatalytic effect due to the presence of metallic nanoparticles exist, and while still under intense study, it could prove a totally new axis of research for plasmonics with fascinating prospects [77–80].

2.2. Semiconductor Nanocrystals

While gyroids seem very promising as building blocks for metamaterials, the ability to fabricate particles with original geometries is equally important. Indeed the field confinement provided by LSPR in plasmonic NP is largely dependent on sharp features which are hardly accessible by physical synthesis. Manna's group at IIT in Genoa has developed a new method to fabricate semiconductor nanocrystals resulting in appealing nanostructures [81–83]. The kind of NP we investigated together were octapods with a $Cu_{2-x_1}Se$ core and $Cu_{2-x_2}S$ arms, see Fig.2.6. Simulated optical cross-sections are also shown

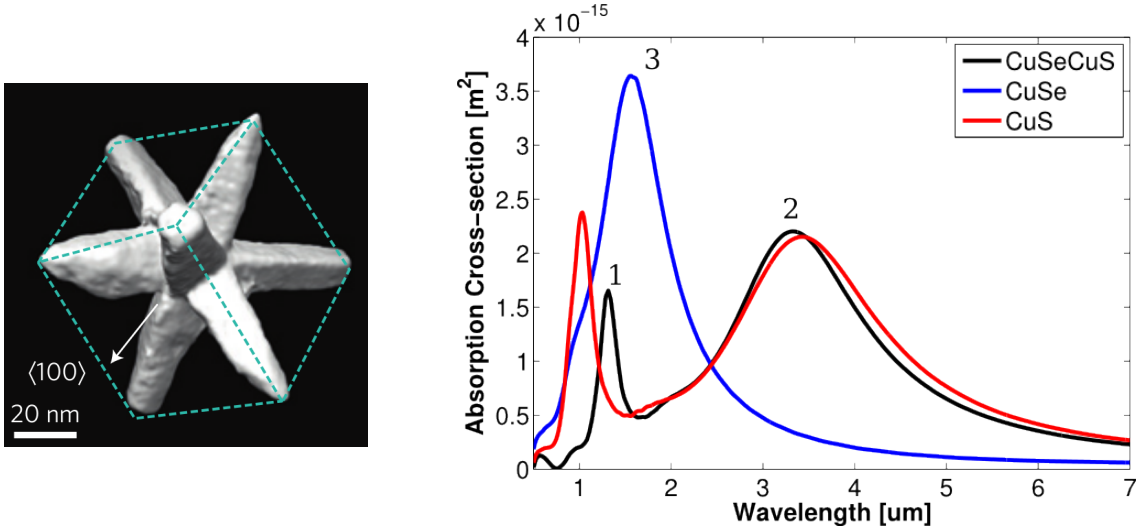

Figure 2.6: Left) 3D reconstruction of an octapod nanocrystal from STEM projections (Reprinted from [83]). Right) Absorption cross-sections calculated by FDTD of $Cu_{2-x}S$(arms)$Cu_{2-x}Se$(core) (black) and plain $Cu_{2-x}S$ (red) and $Cu_{2-x}Se$ (blue) octapods taking the geometrical parameters from the 3D reconstruction shown on the left hand side.

and predict two peaks at ∼1 and 3μm for $x_1 = 15\%$ and $x_2 = 7\%$ (optical models derived from [84]). In order to get some insight into these resonances, plain $Cu_{2-x}S$ and $Cu_{2-x}Se$ octapods were also simulated. It is seen that the core has little effect on the overall spectrum and only one peak is observed for plain $Cu_{2-x}Se$ octapods. This originates from the difference in the dielectric functions of $Cu_{2-x}S$ and $Cu_{2-x}Se$ where the latter presents much more absorption [84]. This is further elucidated by looking at near-field cuts at the various peaks which reveal the field distribution for each mode, Fig.2.7. The peak at ∼1μm consists in a resonance within the arms while the peak at 3μm is rather of tip character. Since the arms are strongly absorbing in the case of plain $Cu_{2-x}Se$ octapods, the first mode is therefore killed. It is also interesting to note that the near-field intensity can reach two orders of magnitude enhancement compared to the incident light.

Such structures hold a lot of promises for photothermal therapy, sensing or nanofocusing because, unlike metallic nanoparticles, they can exhibit strong hotspots at near- and mid-infrared frequencies

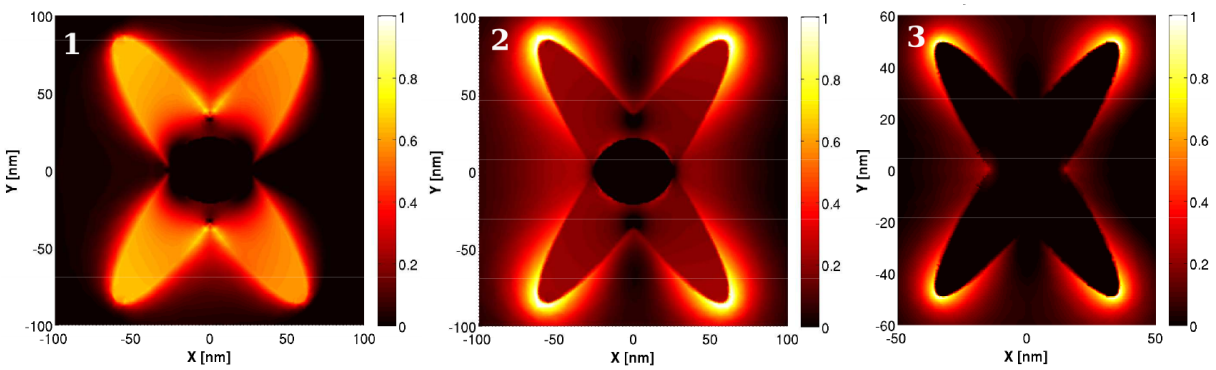

Figure 2.7: Near-field maps $|E|$ obtained by FEM in log scale at the peaks marked in Fig.2.6 within the incident plane [110]. 1) Arm and 2) tip modes of CuSe/CuS octapods and 3) tip mode for CuSe/CuSe octapods. The arm mode disappears in the case of a CuSe core due to its increased absorption compared to CuS, as attested by the almost complete absence of field within the structure. The 2 orders intensity enhancement located right at the $< 20\,\text{nm}$ tips (2 and 3) is highly promising for sensing applications.

while keeping a size below a hundred nanometres [32, 85, 86]. For comparison, a gold nanorod would need to be thirty times bigger to support resonances at similar wavelengths. Despite numerous efforts, our collaborators did not manage to obtain nanocrystals with a sufficiently narrow property distribution. First of all, the exact copper stoichiometry is strongly affected by oxidation. This translates into a dielectric function which could sweep from dielectric to metallic character across the sample, see Fig.2.8 for an example of this effect [83, 86, 87]. A second peculiarity of these systems is the anisotropy of the permittivity [88]. Indeed, although not taken into account in any work until now, the nanocrystals present a different conductivity depending on the orientation of the electric field relative to the crystal axis. In addition, the oxidation process might proceed preferentially along certain crystallographic planes. All these aspects complicate dramatically the overall response of a given sample consisting of a statistical distribution of colloids and prevented our investigations to reach any reproducible results.

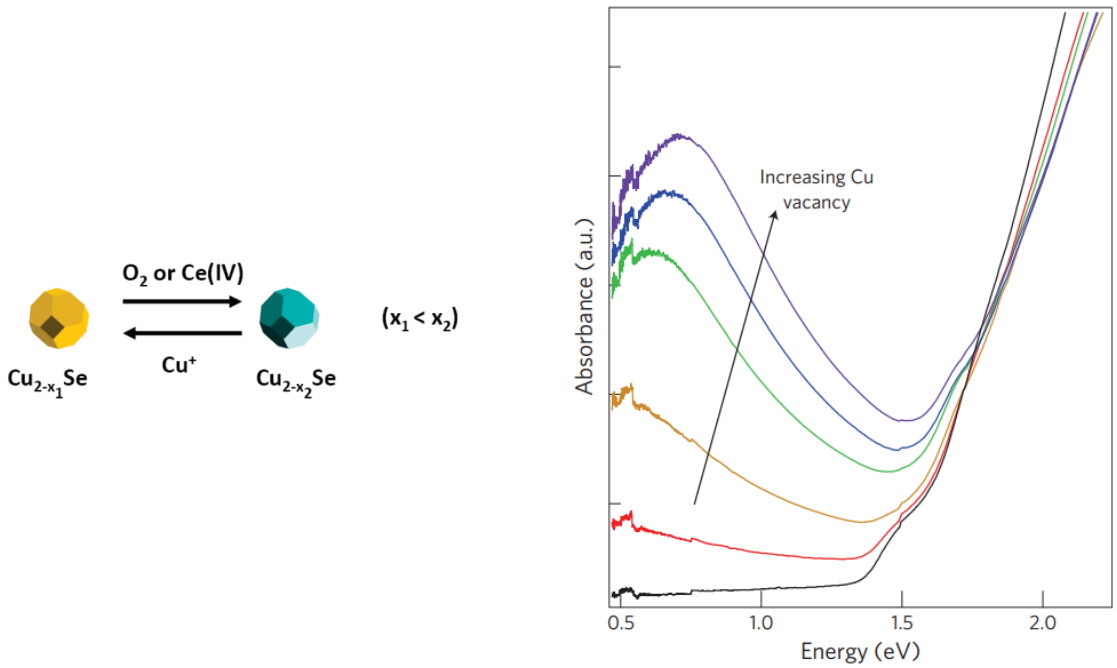

Figure 2.8: Left) Oxidation scheme of CuSe nanocrystal (Reprinted from [82]). Right) Evolution of the LSPR peak of CuS nanorods with oxidation (Reprinted from [32]).

2.3. Localized Phonons in Silicon Carbide

We discussed in Sec.1.2.2.4 the form of the permittivity in polar crystals. There, the presence of optical phonons leads to a negative permittivity within the Reststrahlen band and therefore enables similar field localization effects than one can achieve with metals. We focused our attention on silicon carbide (SiC) which held a lot of promises following the pioneering works of Greffet [89–91] on thermal emission and extraordinary transmission, Hillenbrand [36, 92–94] in surface phonons propagation and nanofocusing and Shvets [95–100] on SiC for superlensing and sensing applications. Other works also investigated SiC nanoparticles for thermal emission [101] and field localization [102–105]. The interest in these materials lies in the fact that the resonances are much stronger than those found in nanostructured metals, be it in the infrared but also in the visible. This is due in part to the small negative permittivities at large wavelengths enabling strong sub-diffraction localization and to the absence of charge transport, limiting the loss channels to phonon-phonon scattering.

2.3.1. SiC Nanoparticles

Our initial efforts consisted in SiC nanoparticles placed on dielectric substrates. The growth of SiC can be complicated as it can form many different polytypes. Among the most common, the cubic zinc-blende 3C, and the hexagonal forms 4H (50% hexagonal) and 6H (33.3% hexagonal) present good "plasmonic" properties as can be seen in Fig.2.9. The use of optical phonons for nanophotonics presents several problems. First of all, the operating frequency range is limited to the Reststrahlen band and even though the energies of optical phonons match with many chemical absorption bands sensing capabilities over an extended mid-IR window will automatically require the use of different polar materials. This is a serious drawback as growth and fabrication techniques are strongly material dependent and necessitate extensive studies. At the opposite, metals are extremely versatile and nanostructures can be easily scaled up in order to span operating frequencies from the visible up to the mid-infrared. Secondly, the large wavelengths involved mean that micrometric particle size must be achieved to allow a decent interaction with the field. However, this tends to induce a redshift of the resonance towards the strong asymptotic absorption band at the TO position. Therefore one must carefully design the particles to mitigate the loss but allow sufficient radiative efficiency. This has consequences for the type of substrate that can be used in conjunction with SiC nanostructures. Indeed, the epitaxial growth of SiC is challenging but possible on binary semiconductors such as InP or GaAs, however, those have high index of refraction in the mid-infrared which are highly detrimental to the localized surface phonon polaritons (LSPhP), as clearly visible in Fig.2.9. There, the high-index substrate induces a redshift of the resonance, pushing it closer to the strong TO absorption band resulting in a markedly reduced cross-section. In addition, semiconductor substrates can be quite absorbing, with complex phonon spectra in the mid-infrared which could overlap with the SiC ones. Lower index dielectrics such as fluorides could solve some of these issues, first, by minimizing the redshift of the LSPhP and second, by allowing transmission measurements. Unfortunately, they exhibit a strong lattice mismatch with SiC resulting in disordered or amorphous films which do not show negative permittivities.

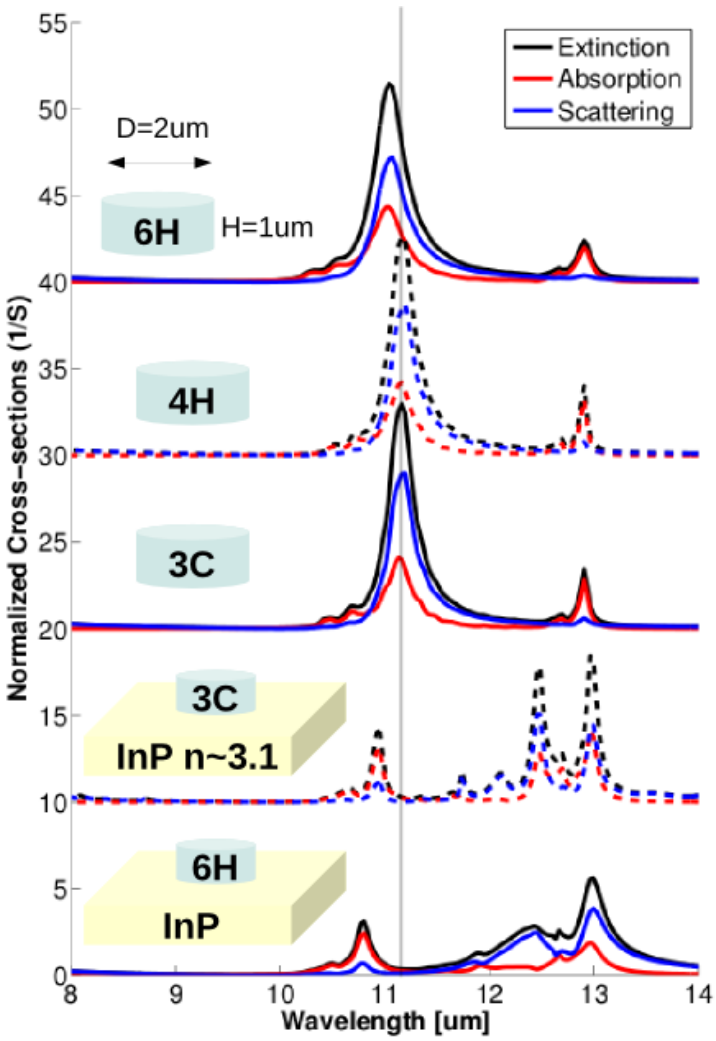

Figure 2.9: Normalized (by the disk area $\pi D^2/4$) extinction (black), scattering (blue) and absorption (red) cross-sections spectra of a SiC disk depending on its polytype (6H, 4H or 3C) [11] and the effect of a high refractive index substrate such as InP (n$\sim$ 3.1). As can be seen, the substrate induces an important redshift of the modes (we therefore observe higher order modes as the first order is completely damped) towards the strongly absorbing TO frequency leading to a markedly reduced and broader extinction spectra with a dominating absorption contribution. The various polytypes present similar optical properties with slight spectral shifts and variations in the absorption/linewidth. Note that the peaks at $\lambda > 12\,\mu$m originate from the high refractive index of SiC close to its Reststrahlen band and not the optical phonons.

2.3.2. SiC Nanopillars

Following the unsuccessful attempts of our first collaborators at the A*STAR Institute of Materials in Singapore to fabricate SiC nanostructures we started another collaboration with Caldwell's group at NRL in Washington D.C. Thanks to their expertise in the growth and patterning of high-index materials we were able to revise our approach. Instead of trying to grow SiC on a substrate, they proposed to etch down a thick SiC substrate with as final target a complete removal of the underlayer of SiC or at worst leave only a very fine webbing underneath the structures to guarantee a certain mechanical stability. Wire-bonding to a low-index substrates and complete etching of the remaining SiC substrate was also suggested. The main reason for achieving unconnected nanostructures is to enable the LSPhP as it was expected those would be strongly damped by a conducting substrate and not different from a mere grating. Surprisingly, the mode spectrum of patterned SiC was much richer than expected and differed markedly from typical periodic plasmonic nanostructures. The results presented below were published in Ref. [106].

Initial patterning of the plain SiC substrate was obtained by a fluorine reactive ion etching (RIE) which resulted in well defined nanopillars still covered with metallic caps coming from the e-beam write, see Fig.2.10b. Those caps were subsequently removed by H_2 etching leaving out pillars with missile-like shapes, see Fig.2.10c. This last fabrication step allowed to remove the detrimental effects of the metal cap which caused strong damping of the modes and their significant broadening as can be seen in Fig.2.10a and reduced the surface damage induced by the RIE process. All the nanostructures described here were patterned out from single-crystalline 6H-SiC thick substrates resulting in pillars with height $H \sim 800$nm, inter-pillar gap $G \sim 150$nm and diameters in the range $D = 150 - 260$nm. The diameter is $D = 250$nm when not specified. It may seem particular to investigate a fixed gap rather than a fixed unit cell, nevertheless due to the deeply sub-wavelength nature of the geometry studied ($D < \lambda_0/10$) the coupling is uniquely due to near-field interaction and no diffraction order contribute to the reflection spectra. This has been further confirmed by our current investigations on a large range of unit cell size and diameter range. It is seen that when a plain SiC substrate is patterned into the nanopillars the reflection spectrum exhibits a set of dips (which correspond to peaks of extinction, i.e. modes). In particular, two distinct modes can be identify and are well-reproduced by FEM simulations, see Fig.2.11a. Note also the stimulation of LO phonons which are enabled by the patterning of the SiC surface but are not localized modes. As we already mentioned in Sec.1.3.2.1, the FTIR objectives have a weighted average incidence angle around $\theta = 25°$ which was used in the simulations. A comparison with a normal incidence excitation shows this is necessary to excite the monopole mode, see Fig.2.11b. The first mode corresponds to a transverse dipole (TD) excitation with an oscillation of the field mainly along the x-axis, see Fig.2.12a. It derives from the dipolar resonance of a free-standing particle and is modified due to the height of the pillar and the presence of the SiC conductive underlayer. Furthermore, it was observed that for heights smaller than 800nm the local field intensity and strength of the resonance were significantly decreased. Besides a strong localization of the field at the bottom of the pillar due to geometric effects, there is a strong hot spot at the tip of the pillar. At the contrary, the monopole mode (M) cannot be supported by a single particle due to charge neutrality. It corresponds to a zero-order oscillation along

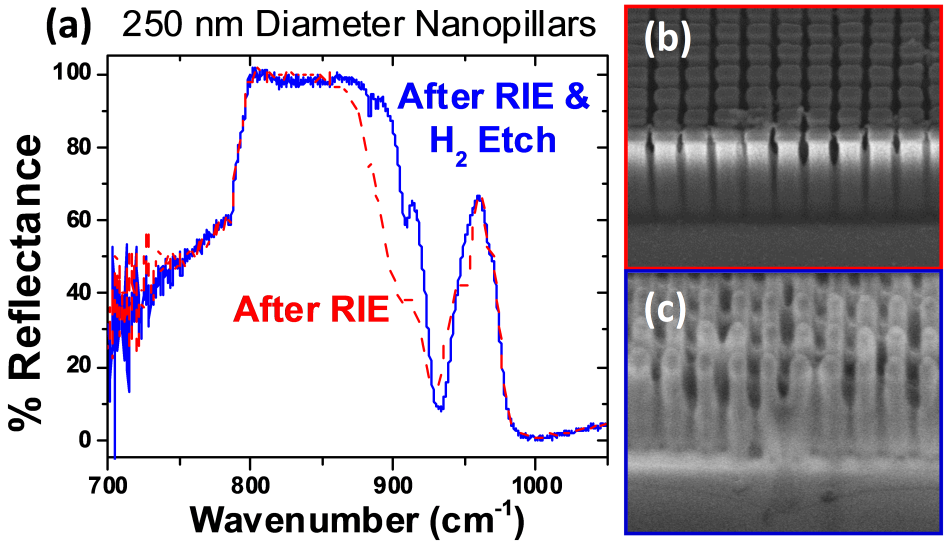

Figure 2.10: a) Reflectance spectra of RIE patterned SiC before and after H_2 etch. SEM images of the sample are shown before b) and after c) this process. It is seen that both modes (dips) around 950 cm^{-1} have a notably reduced linewidths after the H_2 etch while the rest of the spectrum is mostly unaffected. The effect of the etch is to change the nanopillars from a rectangular cross-section to a missile-like shape (Reprinted from [106]).

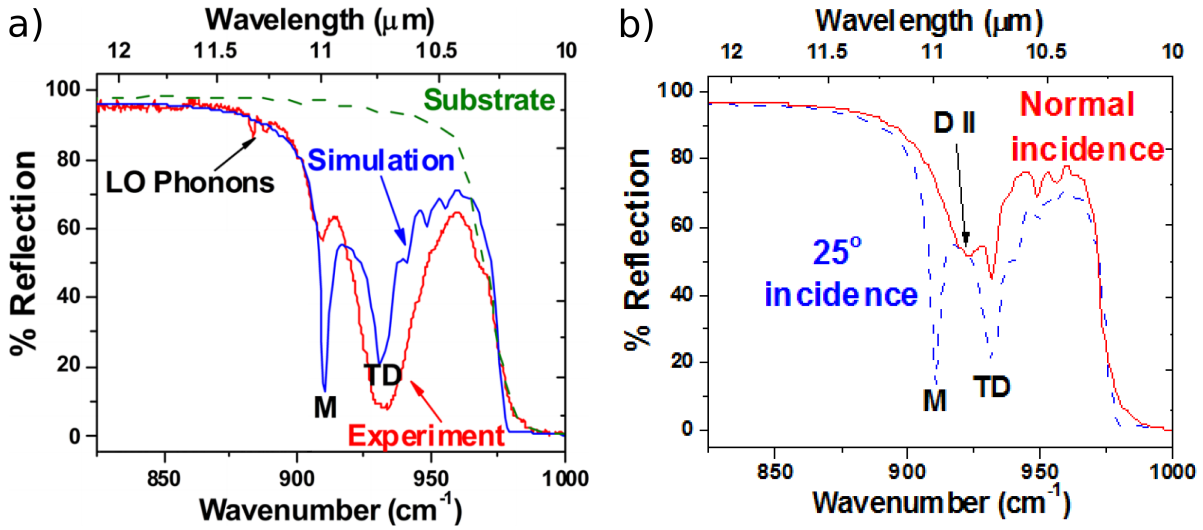

Figure 2.11: a) Comparison of the reflection spectra of SiC nanopillars as obtained by FTIR (red) or FEM (blue) along with the spectrum of an unpatterned substrate (green, FTIR). The two main modes (TD for transverse dipole and M for monopolar) are well captured by the simulation model. b) FEM simulations showing that the monopole mode can only be excited with an off-normal incidence angle because of its symmetry. We also note a general decrease in the nanopillars response at normal incidence (*i.e.* shallower dips) as well as the appearance of a second dipole mode (DII, reprinted from [106]).

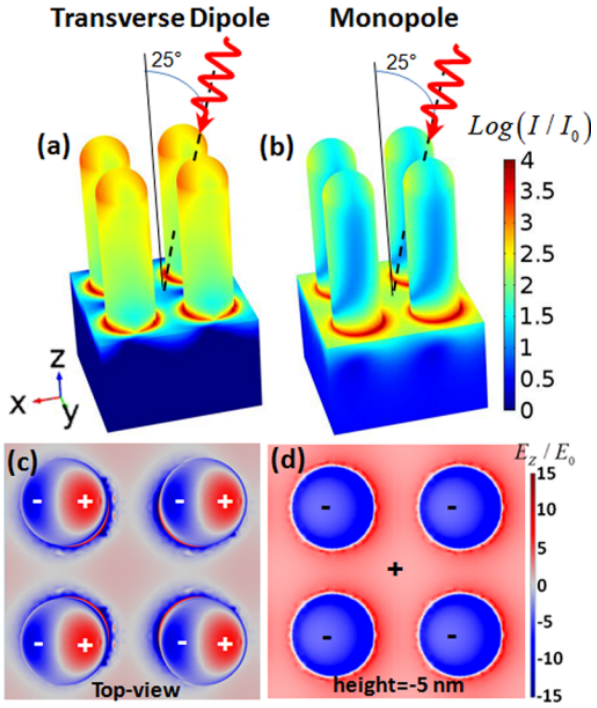

Figure 2.12: Intensity profile (a,b) in log scale and z-component of the electric field (c,d) for a,c) the transverse dipole and b,d) monopole modes as calculated by FEM. One can identify strong hot spots (up to 4 orders of magnitude higher than the incident field) at the tip of the pillars for the case of the dipolar mode and at their base for both modes which can be attractive for molecular sensing. The E_z field is proportional to the charge density at interfaces and we can therefore draw the charges located at the tip (c, dipolar mode) and directly underneath the surface of the substrate (d, monopolar mode) showing the clear dipolar oscillations of the TD mode located mainly near the tip of the pillars; at the contrary, the monopolar mode excitation is enabled through counter-charges within the substrate providing for the charge neutrality requirements (Reprinted from [106]).

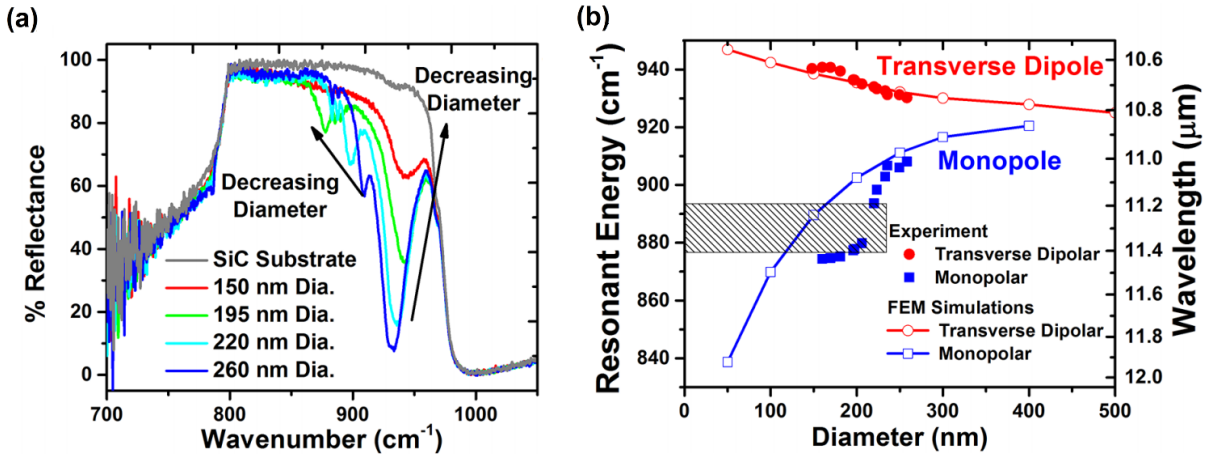

Figure 2.13: Dependence of the modes on the diameter of the pillars. a) Measured reflection spectra and b) peak positions for both modes obtained by FTIR and simulations. We observe a very good quantitative agreement between the measurements and simulations except in the region where the monopole interferes with the LO phonons at 880 cm^{-1} (shaded area) affecting considerably its lineshape and rendering its exact position difficult to identify. The opposite trends (redshift for the TD and blueshift for the M) with the diameter size are consistent with changes in the aspect ratio of small particles in the quasi-static limit for transverse and longitudinal modes respectively (Reprinted from [106]).

the height of the pillar and therefore requires a non-zero component of the field in the vertical direction. This explains why a normal incidence field is not able to stimulate this mode as shown in Fig.2.11b. In terms of charge distribution, it is apparent in Fig.2.11d that it is the presence of a conducting substrate which allows the existence of this mode [107,108]. The field is mostly localized at the bottom of the pillar in that case with intensities reaching four orders of magnitude enhancement compared with the incident field. We report on Fig.2.13 the effect of the diameter on those two peaks. As one would expect the dipole mode redshifts for increasing size and the monopole blueshifts similar to longitudinal modes. The grey area in Fig.2.13b denotes the region where the monopole interacts with the LO phonons producing a Fano interference and making its precise spectral position difficult to extract. Both trends are also recovered by FEM calculations and provide a simple method to identify the nature of modes measured experimentally.

Thanks to their ideal spectral location at most molecular vibration energies, the SiC nanopillars presented here could be highly appealing platforms for surface-enhanced infrared absorption. Indeed the huge field compression which is predicted in the vicinity of the pillars could prove beneficial for gas detection or biomedical sensing. In order to prove the viability of those structures for SEIRA we are currently trying with the group of Prof. Schlücker in Essen to functionalize the surface of SiC to assess what kind of sensitivity can be achieved. Even more striking, we find that the reported modes not only show a strong infrared activity but are also Raman-active, as is apparent in Fig.2.14. Indeed, along the expected TO and LO phonons of a plain unpatterned SiC, see red trace in Fig.2.14a, the Raman signal of SiC nanopillars (red line in Fig.2.14b) presents additional peaks (marked by the black arrows) which spectrally match with the infrared modes we investigated earlier (blue line in Fig.2.14b). This is a very exciting result which suggests one could use SiC nanostructures for both SERS and SEIRA

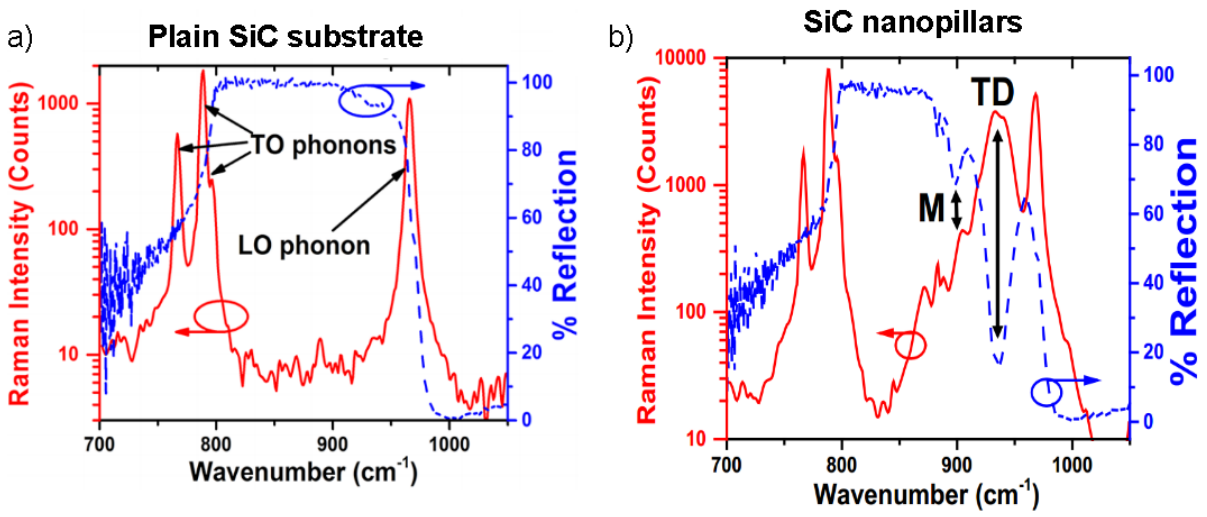

Figure 2.14: Comparison between IR (blue) and Raman (red) spectra for a) a plain SiC substrate and b) a patterned sample. One can observe, along the TO and LO phonons supported by a SiC substrate, the appearance of additional peaks in the Raman spectrum (marked by the black arrows in b) upon patterning which spectrally match the infrared peaks which we identified as the TD and M modes (Reprinted from [106]).

simultaneously. The small wavelengths involved in Raman scattering also mean that the investigation of the modes could be performed with a much higher spatial resolution with micro-Raman. At the moment, we are studying more in depth the relation between the infrared and Raman fingerprints of these nanostructures with changes in geometry, probing the effect of size and coupling.

3. Plasmonics with Graphene

3.1. Graphene Photonics

Since its discovery in 2007 by Geim and Novoselov [109], graphene has experienced an unprecedented gold rush in research. There are many reasons for such activity around graphene. Indeed, it is for instance the first true 2D crystal ever obtained experimentally, ending a long debate on the existence of such materials due to thermodynamics considerations. Following this breakthrough, researchers are now studying other 2D materials like boron nitride a field which the group of Novoselov pioneered. Furthermore, the mechanical strength of this one-atom thick layer of graphite is beyond anything known, apparently, one would need to sit an elephant on a pencil to pierce through the sheet. Its elasticity is also extremely high (about 20%) for a crystal. Chemically speaking, its stability is excellent as well, as one might expect from a pure layer of carbon, and in consequence it can stand relatively high temperature. Graphene is in addition a formidable membrane, impermeable even to hydrogen, and therefore can prevent corrosion and oxidation. However, it is electrically and optically that the true wonders of graphene can really be observed [110–115].

The band diagram of graphene has become famous because of the Dirac cone it forms at the Γ-point. It translates into a linear dispersion relation along the light cone with no gap at zero-energy. This remarkable feature means that the carriers in graphene behave like mass-less particles, from which follows an extremely long scattering time and a gigantic mobility; this is particularly true for undoped graphene where the absence of a gap allows a conversion of the carriers between electrons and holes without energy. As we can see, graphene is the best conductor known to date, but in addition it has a strong quantum character, with $\hbar$ entering most of its properties even at room temperature, like in quantum Hall experiments. Last, the ability to modify the carrier concentration in graphene by chemical doping [116], electrostatic gating [117–121] or electrical injection gives rise to a fantastic tunability of its properties for transistor applications. Moreover, this allows to control finely the frequency range in which interband and intraband processes occur as we will see in what follows [122].

The surface conductivity of graphene can be well described by a semi-classical model based on the Kubo formula in the local random-phase approximation (RPA), that is ignoring the dependence of the response to the wavevector and assuming the electron system to be governed by an averaged electric potential [123, 123–125]. In this frame, the interband and intraband contributions read

$$\sigma_{intra} = \frac{2\mathrm{i}e^2 T}{\hbar^2 \pi(\omega + \mathrm{i}\Gamma)} \ln\left[2\cosh(\frac{\mu}{2T})\right] \tag{3.1}$$

$$\sigma_{inter} = \frac{e^2}{4\hbar}\left[\frac{1}{2} + \frac{1}{\pi}\arctan\left(\frac{\hbar\omega - 2\mu}{2T}\right) - \frac{\mathrm{i}}{2\pi}\ln\frac{(\hbar\omega + 2\mu)^2}{(\hbar\omega - 2\mu)^2 + (2T)^2}\right] \tag{3.2}$$

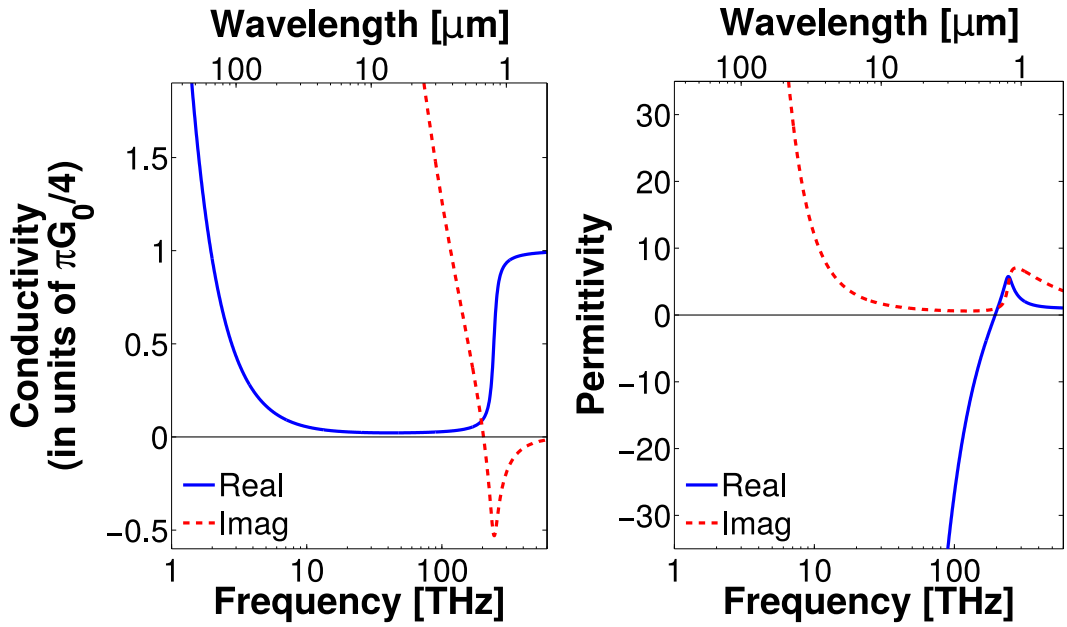

Figure 3.1: Real (full blue lines) and imaginary (dashed red lines) parts of the conductivity (left) and permittivity (right), for graphene at $T = 300\text{K}$ with $\mu = 0.5\,\text{eV}$ and $\hbar\Gamma = 0.1\,\text{meV}$. The conductivity is given in units of $\pi\text{G}_0/4 = 6.08 \times 10^{-5}\,\text{S}$ and the permittivity is calculated for an effective thickness of 0.5 nm. At high frequencies, the normalized conductivity is equal to the universal absorbance of graphene $A/\pi\alpha = 4\Re[\sigma]/\pi\text{G}_0 = 1$ (Reprinted from [127]).

where $T = \kappa_B T$ is the temperature energy, Γ the charge carriers scattering rate, μ the chemical potential (or Fermi level) and $\hbar\omega$ the photon energy. The intraband response is characterized by a Drude-like term $1/(\omega + \text{i}\Gamma)$ and will depend on the carrier concentration n_0 which is related to the chemical potential by [126]

$$n_0 = \frac{2}{\pi(\hbar v_F)^2}\int_0^\infty \mathcal{E}(f_{0-} - f_{0+})\text{d}\mathcal{E} \qquad \text{with}$$
$$f_{0\pm} = \frac{1}{\exp([\mathcal{E} \pm \mu]/\text{k}_\text{B}T) + 1} \qquad \text{and} \qquad v_F = 10^6\text{m/s} \tag{3.3}$$

Interband transitions can also occur for $\hbar\omega \geq 2\mu$ and will result in a strong absorption. In order to calculate numerically the response of graphene, an approach first proposed by Vakil and Engheta is often used [124]. The idea is to represent the monolayer by an effective medium with finite thickness, th, and to assign it an effective bulk conductivity $\sigma_G = \sigma_g/th$ where σ_g is the surface conductivity of graphene. For thicknesses small enough (compared with the wavelength), the results are comparable with simulations defining the layer through a boundary condition and agree with experiments. Based on this method, it is insightful to plot an effective permittivity $\varepsilon_G = 1 + \text{i}\sigma_G/\varepsilon_0\omega$ to illustrate the

behaviour of graphene, see Fig.3.1 where σ_g is plotted along ε_G. One can see that at energies below $\sim 2\mu$ the intraband response dominates, graphene behaves there like a metal with a negative real permittivity (positive imaginary conductivity) and can therefore support surface plasmons. A control over the chemical potential allows in consequence to tune the frequency range at which a plasmonic behaviour is enabled. Above the threshold $\hbar\omega = 2\mu$, there is an interband absorption characterised by a rise in the imaginary permittivity (real conductivity). Furthermore, the absorbance at high energies saturates to the now famous $A/\pi\alpha = 4\Re[\sigma]/\pi G_0 = 1 = 2.3\%/\pi\alpha$ where $G_0 = 2e^2/h$ is the quantum of conductance and $\alpha = e^2/\hbar c$ the fine-structure constant [128, 129]. At energies $1.667\mu < \hbar\omega < 2\mu$ the permittivity can get extremely high (this is the region where $\Im[\sigma] < 0$), especially at low temperatures, and graphene can support weakly bound TE modes which derive from the TE guided modes in a dielectric slab [130].

3.2. Graphene Plasmonics

Plasmons in graphene have offered a second birth to plasmonics [115] with a wide range of structures already explored [131–145] as well as schemes combining metals [146, 147] or metamaterials [148, 149] with graphene. This is due in part to the tunability of graphene plasmons which is absent in metal but most of all because of their extraordinary confinement [150–153]. The latter can easily be visualized if one considers an insulator-metal-insulator (IMI) configuration in which the metal thickness tends to zero. In such a system, the surface plasmons on both side will couple and form two new supermodes being symmetric and antisymmetric, see Fig.3.2. One can see that for a very small thickness, as is the

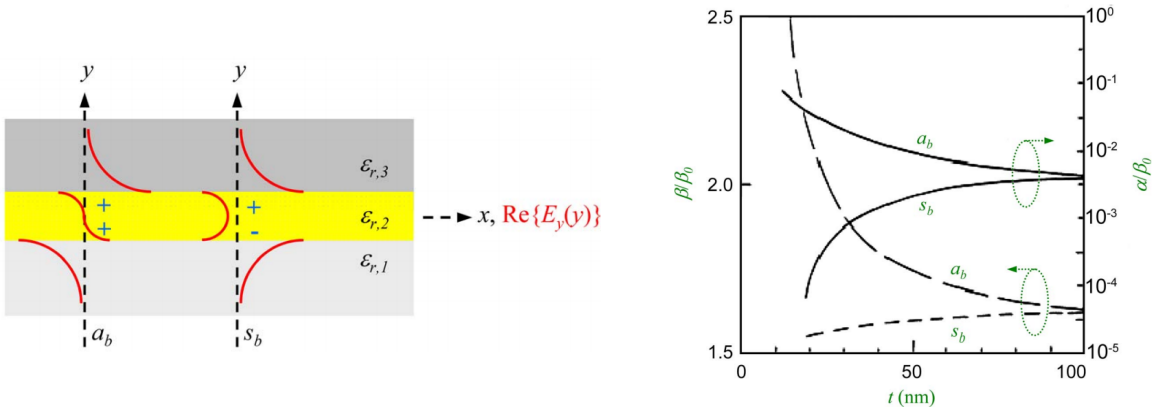

Figure 3.2: Left) Field profiles for the asymmetric (a_b) and symmetric (s_b) surface plasmon supermodes in an IMI propagating along the z direction where the symmetry is ascribed following that of the vertical, evanescent component of the electric field E_y. Right) Evolution of the normalized propagation constant (β/β_0) and attenuation (α/β_0) with the metal thickness t where $\beta_0 = \omega/c$ is the wavevector of light in free space (Reprinted from [42]).

case for graphene, the symmetric mode tends to the unbound TEM wave of the background while the antisymmetric mode becomes extremely confined. However, this is accompanied by a huge increase in the attenuation which is one of the main limitations of graphene plasmonics [154].

The dispersion relations for the asymmetric and symmetric modes can be derived similarly to that for a single interface, Sec.1.2.3.2, with the evanescent fields on both sides adding together within the film.For a symmetric environment it reads [3, 15]

$$a_b(w_-) : \tanh k_{z,m}d = -\frac{k_{z,m}\varepsilon_d}{k_{z,d}\varepsilon_m} \qquad \text{and} \qquad s_b(w_+) : \tanh k_{z,m}d = -\frac{k_{z,d}\varepsilon_m}{k_{z,m}\varepsilon_d} \tag{3.4}$$

with d the thickness of the film, $k_{z,m} = \sqrt{\varepsilon_m k_0^2 - \beta^2}$ and $k_{z,d} = \sqrt{\varepsilon_d k_0^2 - \beta^2}$. The asymmetric surface plasmons mode supported by graphene can be obtained by replacing ε_m by the effective permittivity ε_G and taking the limit $th \to 0$ and we obtain [124, 153]

$$\beta = k_0\sqrt{1 - \left(\frac{2}{\eta_0\sigma_g}\right)^2} \sim 2\mathrm{i}\omega\varepsilon_0/\sigma_g \tag{3.5}$$

with $\eta_0 = \mu_0 \mathrm{c} = 1/\varepsilon_0 \mathrm{c}$ the impedance of free space.

By confining the plasmons along the transverse direction as in nanoribbons, the graphene can act as a waveguide with modes corresponding to the ones found in metallic stripes [42]. At first intriguing, the highly localized edge modes one can find in graphene ribbons originate from the corner modes in plasmonic waveguides in the limit of vanishing thickness [42]. Nanoribbons are more attractive than plain sheets because they can serve as building blocks for nanocircuitry for instance. They can be easily fabricated by lithography and plasmonic resonances were recently measured [119–121]. Theoretically, they were studied by Nikitin and co-workers [155] and paired ribbons were also considered by Christensen *et al.* revealing a rich mode spectrum caused by lifting of degeneracy and hybridization [156]. In what follows, we will consider the modes which exist in wide vertically paired ribbons, referred to as sandwiches from now on, investigating carefully the hybridization mechanism. This will allow us to understand thoroughly the nature of these modes and propose appealing and experimentally accessible geometries for applications in circuitry and sensing. The results shown below were published in Ref. [127].

3.3. Gap Modes in Graphene Sandwiches

3.3.1. General Properties of Graphene Guided Modes

As stated above, a graphene ribbon can support guided TM plasmon modes, like any metallic stripe, the physics of which is equivalent to a dielectric slab guiding TE modes [157]. When two ribbons are placed on top of each other the plasmons can hybridize and due to the transparency of graphene result in strongly confined modes with field localized either within the gap or at the external faces. The understanding of

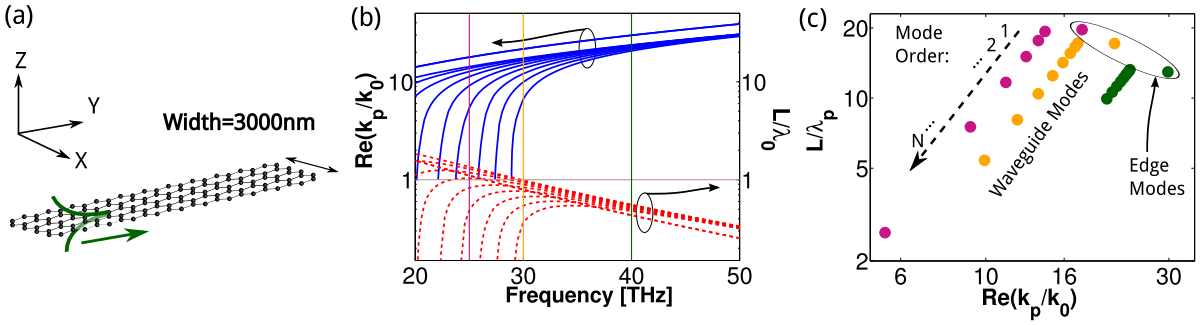

Figure 3.3: (a) Axis convention and geometry of a graphene ribbon with a chemical potential $\mu = 0.5\,\mathrm{eV}$ and charge carrier scattering rate $\hbar\Gamma = 0.1\,\mathrm{meV}$. (b) Normalized wavevector $\Re[k_p/k_0]$ (blue lines) of the 10 first modes and propagation length L/λ_0 (red dashed curves) in log scale versus the frequency for a 3000 nm wide graphene nanoribbon. (c) The same modes as in (b) at 25 (violet), 30 (orange) and 40THz (green) plotted as L/λ_p versus $\Re[k_p/k_0]$ on a log-log scale (Reprinted from [127]).

the nature of these modes starts with the modal behaviour within a single ribbon. If we consider guided plasmons propagating along Y on a graphene ribbon perpendicular to Z and with a finite width along X, see Fig.3.3a for a schematic, their dispersion will follow the behaviour of the surface plasmons in an infinite sheet at high frequencies, *i.e.* Eq.3.5. This is illustrated in Fig.3.3b for the first 10 modes found in a 3μm wide ribbon with $\mu = 0.5$eV and $\hbar\Gamma = 0.1$meV where the normalized propagation constant and propagation length are plotted as a function of the frequency. These define the plasmon mode wavelength $\lambda_p = 2\pi/k_p = \lambda_0/\Re[q]$ and 1/e intensity decay along the propagation direction by $L = \lambda_0/4\pi\Im[q]$ with the normalized wavevector $q = k_p/k_0$. One can see that as the frequency is reduced the modes approach their respective cut-offs at which they cease to be supported as witnessed by their increasing attenuation. At large wavelengths, or for a narrower ribbon, no waveguide mode will be supported. The two lines observed at higher wavevectors represent the dispersion relation of the two coupled edge modes. Their symmetric combination has virtually no cut-off.

We propose here a different representation of the modes, selecting single frequencies (25, 30 and 40THz or alternatively 12, 10 and 7.5μm), and plotting the two critical parameters that are the propagation and wavevector against each other, see Fig.3.3. In this fashion, one can clearly distinguish between the waveguide modes (WG) distributed along a line in log-log scale and the edge modes located at slightly larger q. The propagation length is now normalized to the plasmon wavelength and one can note

that although the modes hardly propagate more than a free space wavelength this is due to the strong compression as they still travel tens of optical cycles. Nevertheless, L/λ_0 is easily accessible by dividing L/λ_p by the corresponding $\Re[q]$. Similarly, the confinement within the surrounding dielectric δ/λ_0 is close to $1/4\pi\Re[q]$. Indeed, $\delta/\lambda_0 = k_0/4\pi\Im[k_z]$ but due to the large wavevectors of plasmon modes in graphene $k_z = \sqrt{k_0^2 - k_p^2} \sim \mathrm{i}k_p$. As always in plasmonics, this implies that for a given mode order a stronger confinement is accompanied by a lesser propagation [127].

3.3.2. Single versus Sandwiched Ribbons

Let us now limit ourselves to $\nu = 30$THz ($\lambda_0 = 10\mu$m) in order to avoid the intrinsic dispersion of the material properties and compare two single ribbons of width 3 and 0.3μm, see top panel in Fig.3.4. As is apparent in Fig.3.4b, the narrow ribbon (green symbols) does not support any WG modes (from now on marked by circles) but it shows two distinguishable edge modes (5 and 6, marked by squares) which merge together for the wider structure (4*, red symbols). The field profile is presented in Fig.3.4c for both the WG and edge modes. If one placed two wide ribbons on top of each other and separated by a

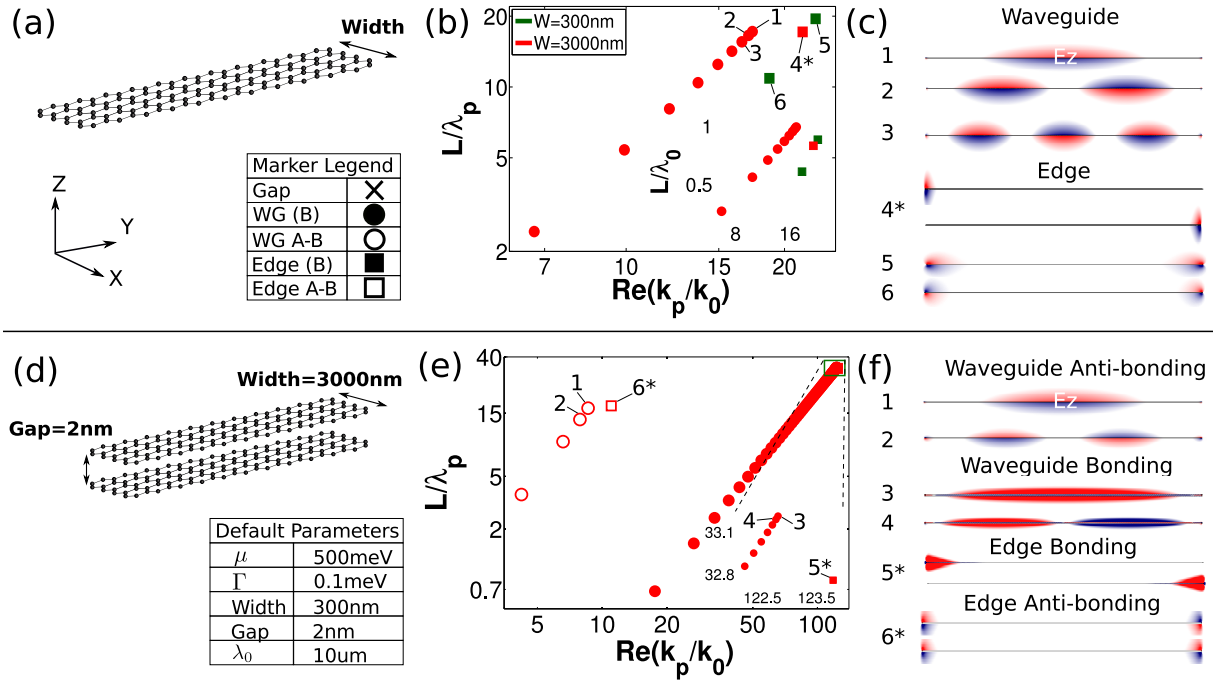

Figure 3.4: (a) Ribbon geometry and symbols convention. (b) Mode spectrum of 300 nm (green) and 3000 nm (red) graphene ribbons at $\lambda_0 = 10\,\mu$m; the inset shows the same modes with the propagation length normalized to the free space wavelength. (c) E_z field with positive (negative) sign coloured in red (blue) for the modes numbered in (b), the "*" denotes the degeneracy of the modes. (d) Sandwich geometry and summary of the default parameters used throughout the article unless otherwise specified. (e) Mode spectrum exhibited by a sandwich of two 3000 nm wide ribbons vertically offset by 2 nm, the inset is a zoom of the green rectangle in the top right-hand side corner; bonding modes are represented with full markers while anti-bonding ones are marked with open symbols. (f) E_z field of the modes numbered in (e) (Reprinted from [127]).

2nm gap, see Fig.3.4d, one notices the emergence of bonding (B, full markers) and anti-bonding (A-B, open markers) combinations of both the edge and WG modes, Fig.3.4e. The A-B modes follow the same dispersion than the original and B modes but shifted at smaller wavevectors. The field profiles for these modes are shown in Fig.3.4f. The A-B combinations present a minimum field in the gap (same charges) while the B modes have opposite charges on the two internal faces leading to a maximum of the field within the gap. Note that the "$*$" denotes the degeneracy of the modes [127].

3.3.3. Mode Evolution

Before investigating further the evolution of the coupled modes when varying the frequency or the gap, it is instructive to develop a simple model to describe the guided plasmon modes in graphene nanoribbons. Following a similar approach than Zia *et al.* [157] for metallic stripes, we can write the total in-plane wavevector as $k_x^2 + k_y^2 = \beta^2 = k_{spp}^2$, or in other words, we assume that the vertical component is left unchanged by the finite width. The modes we consider are bound and in consequence both k_x and k_y must be bigger than $\sqrt{\varepsilon_d}k_0$. This allows us to write that $k_x^2 = k_{spp}^2 - k_y^2 < k_{spp}^2 - \varepsilon_d k_0^2$. In addition, the highest mode supported by the stripe will have N maxima along the width W and so $k_{x,max} = N\pi/W$. This leads naturally the total number of modes supported by a single ribbon as

$$N < \frac{2W}{\lambda}\left[\mathrm{i}\varepsilon_0(\varepsilon_d + 1)\mathrm{c}/\sigma - \sqrt{\varepsilon_m}\right] \tag{3.6}$$

where we used $k_{spp} = \mathrm{i}\varepsilon_0(\varepsilon_d + 1)\omega/\sigma$. The number of waveguide modes as a function of width and operating wavelength is presented in Fig.3.5a for the same graphene discussed previously ($\mu = 0.5\,\mathrm{eV}$ and $\hbar\Gamma = 0.1\,\mathrm{meV}$). One can clearly recognize the effect of the dispersion which allows more modes as the frequency approaches the surface plasmon asymptote.

If we look back at Fig.3.3b and realize this is a dispersion diagram (i.e. energy versus wavevector) rotated by 90° then it is easy to realize that the coupling between two ribbons will proceed similarly to the scheme in Fig.3.5b. Anti-bonding modes will form at higher energies and in consequence will exhibit smaller wavevectors for a given frequency. Bonding states will tend to reduce the energy of the

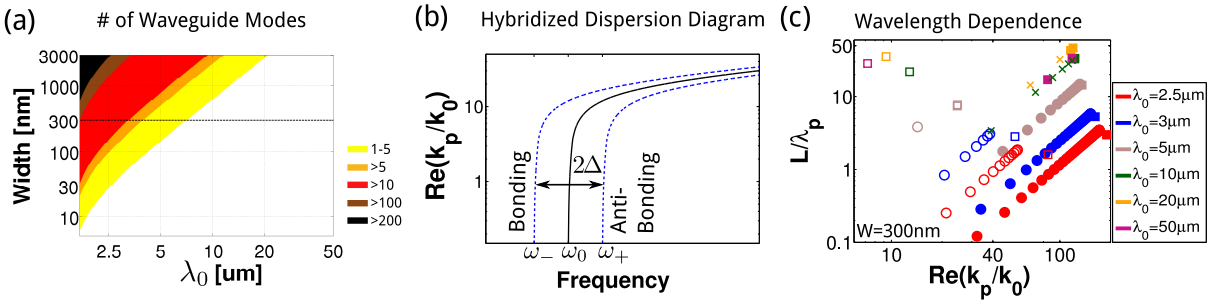

Figure 3.5: (a) Number of waveguide modes in a single graphene ribbon as given by Eq.3.6. (b) Schematic of the hybridization mechanism as seen in the dispersion diagram. (c) Mode spectra for a sandwich with 300 nm width and 2 nm gap at different wavelengths; the marker legend is the same than in 3.4a (Reprinted from [127]).

system and show larger k-vectors for a fixed frequency. From this simple model, one expect in addition to observe bonding modes beyond the cut-off wavelength of the single ribbon. This is illustrated in Fig.3.5c where the modes for a graphene sandwich with $W = 300$nm and $Gap = 2$nm are plotted at different wavelengths. It is seen that as the wavelength is increased the total number of waveguide modes (shown by circles) decreases with the anti-bonding ones (open circles) disappearing above 5μm. We also choose to represent hybridized waveguide modes which exist above the cut-off of the single ribbon by crosses and name them gap modes due to their particular field distribution which will be discussed later. In order to distinguish more easily between the various hybridization mechanisms taking place we will consider this sandwich geometry below cut-off (at 2.5μm) where both A-B and B waveguide modes are supported and above (at 10μm) where only B modes are present.

3.3.4. Mode Hybridization

The hybridization is strongly mediated by the gap and this mechanism for waveguide modes is easily observed below cut-off, see Fig.3.6. Indeed, as the gap is increased the two combinations (A-B and

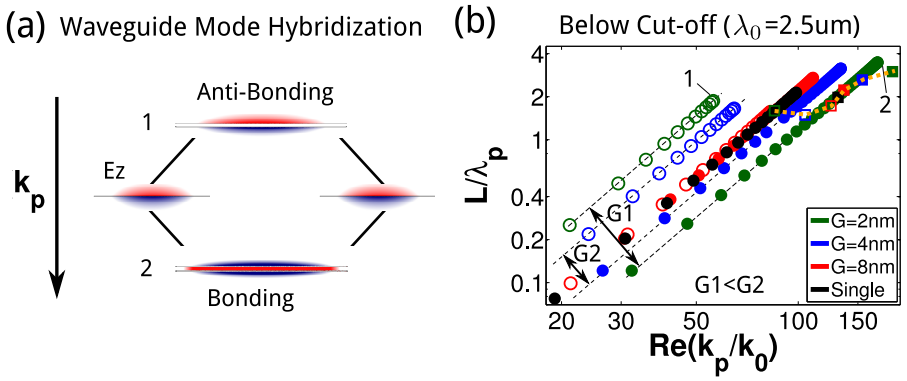

Figure 3.6: (a) E_z fields and hybridization mechanism between two single ribbon waveguide modes splitting into anti-bonding and bonding combinations. (b) Mode spectra of a graphene sandwich at $\lambda_0 = 2.5\,\mu$m (below cut-off) for different gap sizes (coloured markers) compared with a single ribbon (black symbols), the E_z fields for the numbered modes are shown in (a) and the dashed line indicates the evolution of the edge modes with the gap (Reprinted from [127]).

B) merge to the spectrum of the single ribbon shown in black. Anti-bonding states have a reduced confinement and therefore increased propagation while bonding configuration are further confined. It is also apparent that the hybridization only occur between waveguide modes of identical order. Last, the edge modes (indicated by squares) initially degenerated for a single ribbon (remember Fig.3.4b and c) split due to the coupling and move further away from each other as this one is increased. Above cut-off, see Fig.3.7, the situation is apparently more complicated as one vary the gap because the effective cut-off for the bonding waveguide mode is strongly dependent upon it. In addition, the longer wavelength lift the initial degeneracy of the edge modes within the single ribbon resulting in the existence of four edge modes in total in the sandwich case. Fig.3.7a depicts the hybridization scheme for the edge modes in the sandwich and one can observe in Fig.3.7b that they experience a sort of a anti-crossing where the

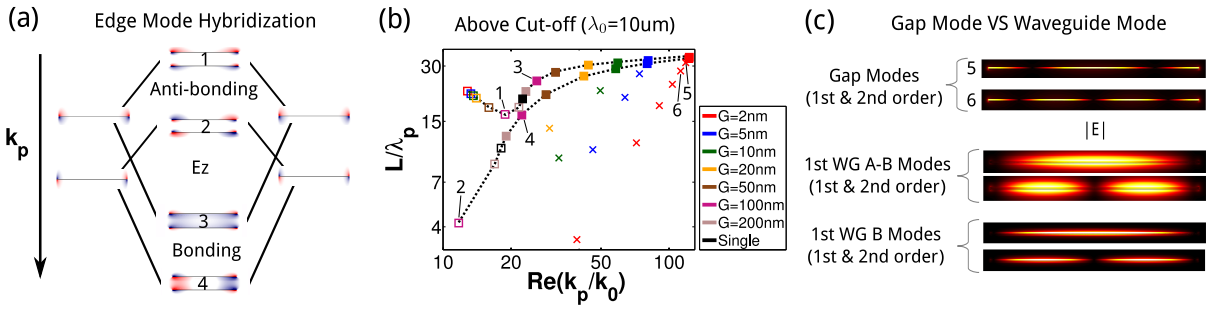

Figure 3.7: (a) E_z fields and hybridization mechanisms for the symmetric and antisymmetric edge modes in single ribbons when brought in proximity to each others. (b) Mode spectra of a graphene sandwich at $\lambda_0 = 10\mu$m (above cut-off) for different gap sizes (coloured markers) compared with a single ribbon (black symbols); the dashed lines indicate the evolution for the two branches of edge modes with different symmetries and the E_z fields for the numbered modes are shown in (a). (c) Difference in the field $|E|$ distribution between gap, anti-bonding and bonding waveguide modes (Reprinted from [127]).

states composed of original edge modes with opposite symmetries evolve on separate lines (shown by the two black interrupted lines). Last, as stated above, the gap affects the bonding waveguide modes and those are more numerous and with higher wavevectors as the coupling is stronger. It is instructive to compare further the modes presented here by looking at the distribution of the field intensity in the sandwich structure. As one might expect, the field is maximum within the gap for the bonding waveguide mode and minimum for the anti-bonding configuration, Fig.3.7c. However, the confinement of the field is striking for both cases with nearly no field outside the 2nm-gap region for the former and a field almost exclusively located within a few nanometres from the surface for the latter. The gap modes, which are those bonding waveguide modes existing beyond the cut-off of the single ribbon have a modified field profile with a significant contribution from the edges and an even tighter confinement of the field coupled with longer propagation.

3.3.5. Towards Realistic Devices

Until now, we only considered ideal structures consisting of floating graphene sheets. Obviously, we need to implement now the effect of a substrate as well as a dielectric spacer. Fig.3.8 presents the mode spectra for the same graphene sandwich we investigated earlier placed in different dielectric environment. The first effect of a dielectric is to compress further the wavelength of the plasmons and lead to increased wavevectors (black symbols compared with green ones). Furthermore, it is seen that most of the effect is caused by the index within the gap rather in the surrounding of the structure (blue compared with black and green). It is quite important to remark as well that anti-bonding modes cease to exist when the indices on the two sides of the graphene ribbon are too different (blue markers), which can prove beneficial for sensing applications. Surprisingly, A-B modes still exist when the sandwich is placed on a substrate probably by propagating at the upper interface (red symbols). One of the advantages of graphene is its tunable properties which allows to control the confinement and propagation of the modes simply by changing its carrier concentration, see Fig.3.9-I. An increase of the doping leads to better propagation

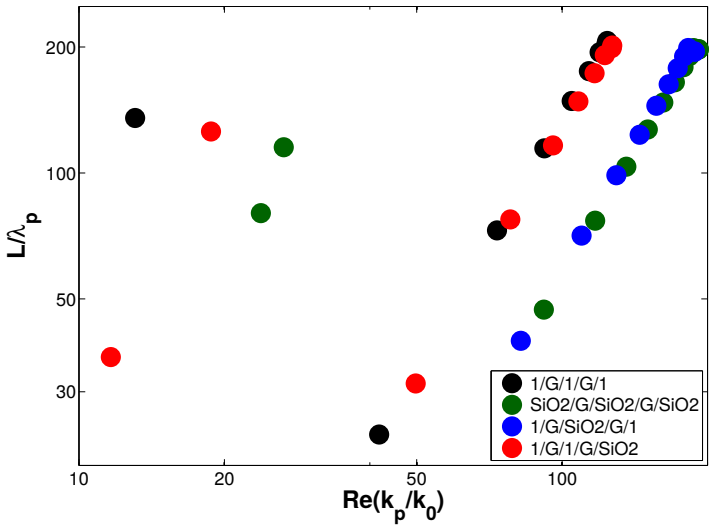

Figure 3.8: Mode spectra for graphene sandwiches ($\lambda_0 = 10\mu$m, $W = 300$nm, $Gap = 2$nm, $\mu = 0.5\,$eV and $\hbar\Gamma = 0.1\,$meV) with different symmetric and asymmetric dielectric environments.

as the asymptote is moved further from the operation frequency and therefore the wavevectors get closer to the light line. We have seen that the addition of a substrate and a dielectric spacer in the sandwich geometry can lead to the suppression of the anti-bonding modes but the highly confined bonding states are more robust as they are isolated from the surrounding. Nevertheless, they still require the presence of two vertically spaced ribbons to exist which is fairly impractical. Since they originate from the symmetric superposition of the original modes we can expect a single ribbon together with its image to reproduce the same hybridization process. This is indeed what is observed when one place a ribbon above a gold mirror and spaced by $2n$m of dielectric with $n = 1.5$, see Fig.3.9-II. Although the anti-bonding modes are lost, this new configuration conserves all the other features found within the spectrum of a sandwich confirming our intuition. In order to simplify further the designing of devices making use of these modes, we consider now an operating frequency of 3THz (100μm) where the permittivity of highly doped silicon has a magnitude high enough to use it as a mirror. In this geometry, we recover again the same strongly confined gap modes though they suffer from a bit more loss due to phonons within the graphene and the limited conductivity of silicon, Fig.3.9-III.

The modes supported by graphene sandwiches and graphene on conducting substrates can easily be envisioned for two distinct applications. On one hand, the strongly confined gap modes can be used as building blocks for nanocircuitry with an operation range from the infrared down to the terahertz. The versatility offered by graphene through electrostatic gating when placed on oxidized silicon and its ease of patterning by lithography are promising, see left-hand side of Fig.3.10. On the other hand, due to the localization of the field right at the surface in anti-bonding waveguide modes, one could imagine a scheme where a graphene sandwich is buried within a dielectric. A flow cell could be placed on top and a liquid with a similar index than the one within the gap used as matrix. Due to the strong field close to the

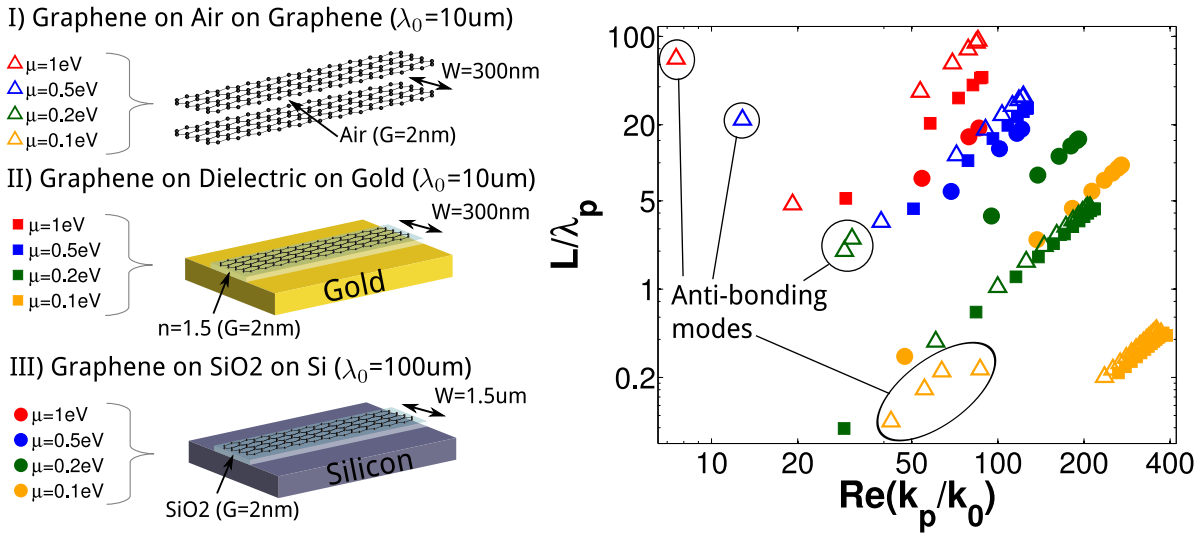

Figure 3.9: Mode spectra of I) a graphene sandwich (open triangles) for different dopings (or chemical potentials μ) compared with II) a graphene ribbon placed on top of a gold [158] substrate spaced by a 2 nm thick dielectric spacer with refractive index n=1.5 (full squares) and III) a wider ribbon at $\lambda_0 = 100\,\mu$m on top of a highly doped ($N = 10^{20}\text{cm}^{-3}$) silicon substrate [159] coated with a 2 nm thick silica layer (full circles) (Reprinted from [127]).

ribbon particles within the flow cell might get attracted at the surface and changes in the environment of the mode will affect its propagation efficiency and therefore be measured as changed in intensity, see right-hand side of Fig.3.10.

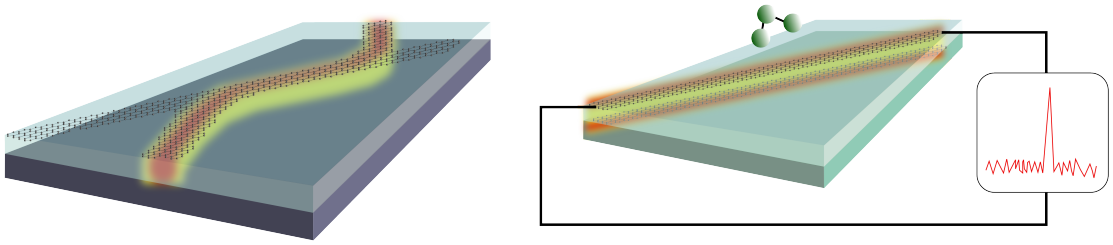

Figure 3.10: Left) Patterned graphene on an oxidized conducting plane can support tightly confined modes located within the dielectric and could therefore serve a building block for nanocircuitry. Right) Two graphene ribbons embedded within a dielectric substrate support anti-bonding modes with field concentrated at the surface allowing at the same time the sensitive probing of the external face and the electrical detection of changes which might occur there (Reprinted from [127]).

3.4. Graphene Sensor

Drawing on the exceptional confinement of plasmons in graphene sandwiches, we propose here a sensor which makes use of the particular field distribution of A-B WG modes. A schematic of an experimental setup is presented in Fig.3.11. It can for instance be used as an accessory to a FTIR microscope which provides the source and detector components. It would rely on three essential elements, first, two channels one for the sample and one for the reference, second, a flow cell which circulate the liquid sample on top of the graphene sandwich and third, a grating coupler which allows to excite and detect the plasmon modes. To prove the novelty, feasibility, extreme sensitivity and robustness of such a sensor, we analyse

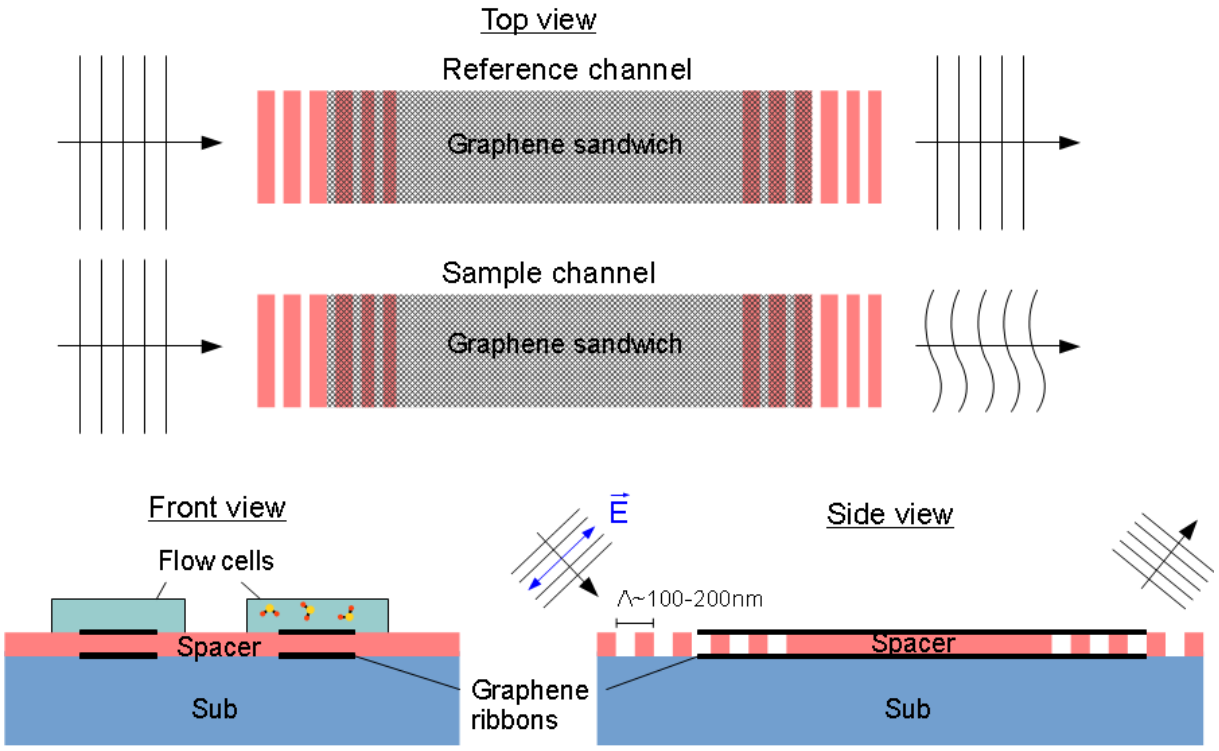

Figure 3.11: Excitation and detection scheme for a sensor based on graphene sandwiches. The device would consist in two different single channels (one for the reference and one for the sample) in the form of a flow cell, in which chemical species can be circulated, and covering a graphene ribbon sandwich separated by a spacer and placed on a substrate. The excitation and detection would proceed from free-space via, for instance, a grating coupler, exciting the coupled plasmon modes supported by the graphene sandwich. Given the moderate compression of those modes, gratings with a period not smaller than $\Lambda \sim 100\,\mathrm{nm}$ should be enough to achieve an efficient coupling. The confined, propagating modes will suffer from increased loss at the analyte absorption lines: their intensity as a function of frequency will therefore reflect the sample absorption spectrum.

the geometry shown in Fig.3.12. It consists of a graphene sandwich separated by a 2nm gap, with a 600nm width and as before $\mu = 0.5\mathrm{eV}$ and $\hbar\Gamma = 0.1\mathrm{meV}$. The spacer layer has an index of 1.5 and the substrate index is set to 1.5 or 3.4. The 2nm-thick top layer is chosen to be either purely dielectric with $n = 1.5$ in which case it is considered sample-free or with a complex index $\tilde{n}$ which is given by the molecule absorption. We choose here a phenol molecule (transmittance spectrum obtained from the National Institute

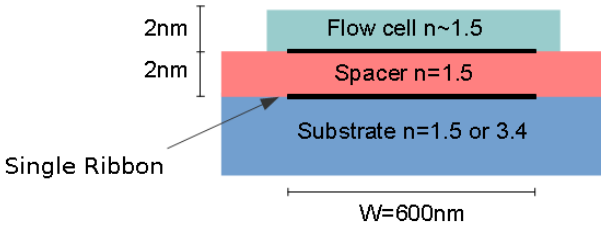

Figure 3.12: Geometry of the calculated sensor based on graphene sandwich A-B WG modes.

of Standards and Technology (NIST) `http://webbook.nist.gov/cgi/cbook.cgi?ID=C108952&Units=SI&Type=IR-SPEC&Index=1#IR-SPEC`) and plot its infrared absorbance in Fig.3.13. From Beer-Lambert's

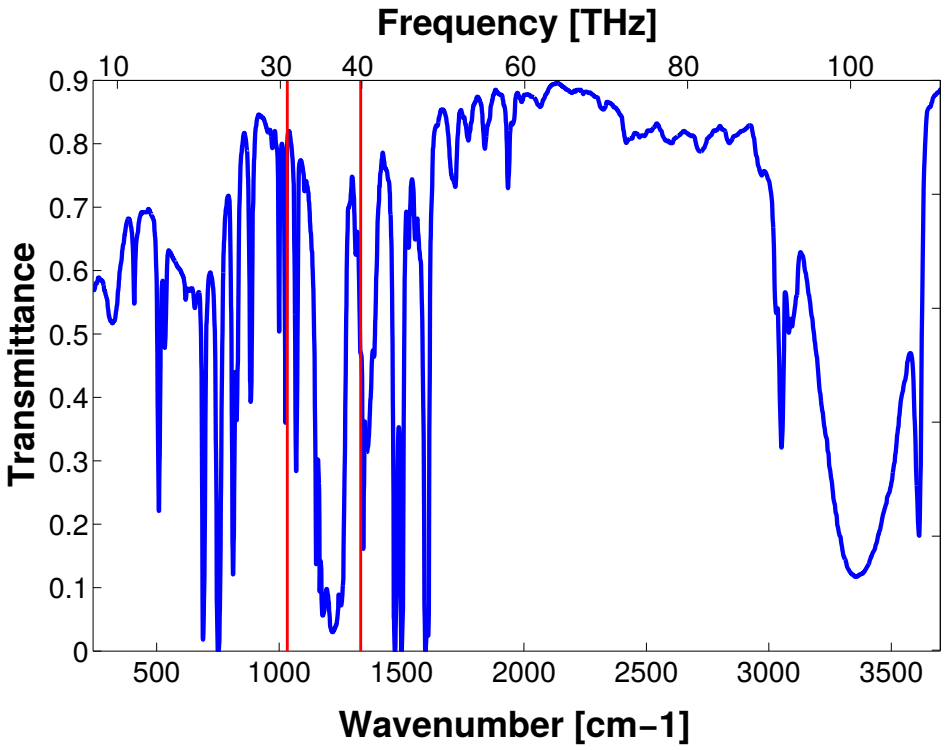

Figure 3.13: Transmittance of a 0.011 cm-thick phenol concentrated at 10% (from NIST). The red lines denote the frequency range considered in the following calculations.

and Kramers-Kronig's relations, recall Eqs.1.25 and 1.26, we can extract the absorption coefficient α from the transmittance of the molecule and calculate its refractive index. The molecule index is then

$$\tilde{n}(\omega) = 1.5 + \frac{\mathrm{c}}{\pi}\mathcal{P}\int_0^\infty \frac{\alpha(\omega')}{\omega'^2 - \omega^2}\,\mathrm{d}\omega' + \mathrm{i}\frac{\alpha(\omega)\mathrm{c}}{2\omega} \tag{3.7}$$

The layer defined in this fashion is a good approximation of a monolayer with a phenol-like vibrational spectrum. To illustrate further the sensitivity of our sensor we only use a phenol concentrated to 10% in the following results.

We select here the frequency window 31-40THz (1033-1333cm^{-1}, 9.7-7.5μm) corresponding to a region where molecules show fingerprint-like spectrum which allows their clear identification and which is highlighted in red in Fig.3.13. In this regime, the proposed structure supports only one or a few A-B WG mode which makes their analysis easier. However, it should be noted that even at higher frequencies, where a lot of modes can be excited, they will all have similar sensing capabilities and sum up together. If the conditions are nearly identical on the two channels, the same normalization will take place resulting in exactly the same behaviour as reported in what follows. We show in Fig.3.14 the normalized propagation constants $q = k_p/k_0$ and propagation distances L/λ_p for the first order A-B WG mode for the proposed structure with and without the absorbing molecule. It can be seen in Fig.3.14 that although the presence

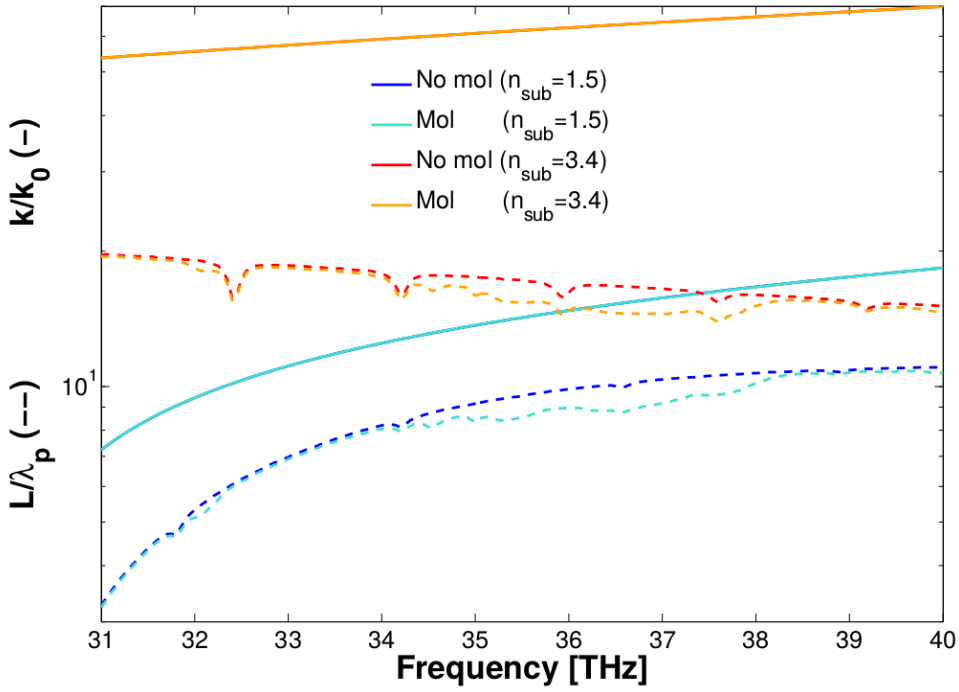

Figure 3.14: Normalized propagation constants (full lines) and propagation distances (interrupted lines) for the first order A-B WG mode of a graphene sandwich sensor. The substrate index is 1.5 (dark and clear blue) or 3.4 (red and orange) for the structure without (dark blue and red) or with (clear blue and orange) a phenol-like top layer.

of the molecule does not perturb the real propagation constant of the modes, the propagation distance is notably affected. More specifically, the intensity of the mode is calculated by $I = I_0 \exp(-2\Im[k_p]x)$ with x the distance which the plasmon mode has propagated. From this relation it is easy to extract the relative intensity at the output of the device for the two channels. We plot in Fig.3.15 the intensity change in dB, calculated as dB $= 10 \times \log(I_{sample}/I_{ref})$, and linear scale. The change due to the a 2nm-thick diluted molecule are impressive and can reach up to 50% (3dB) for a 10μm distance between input and

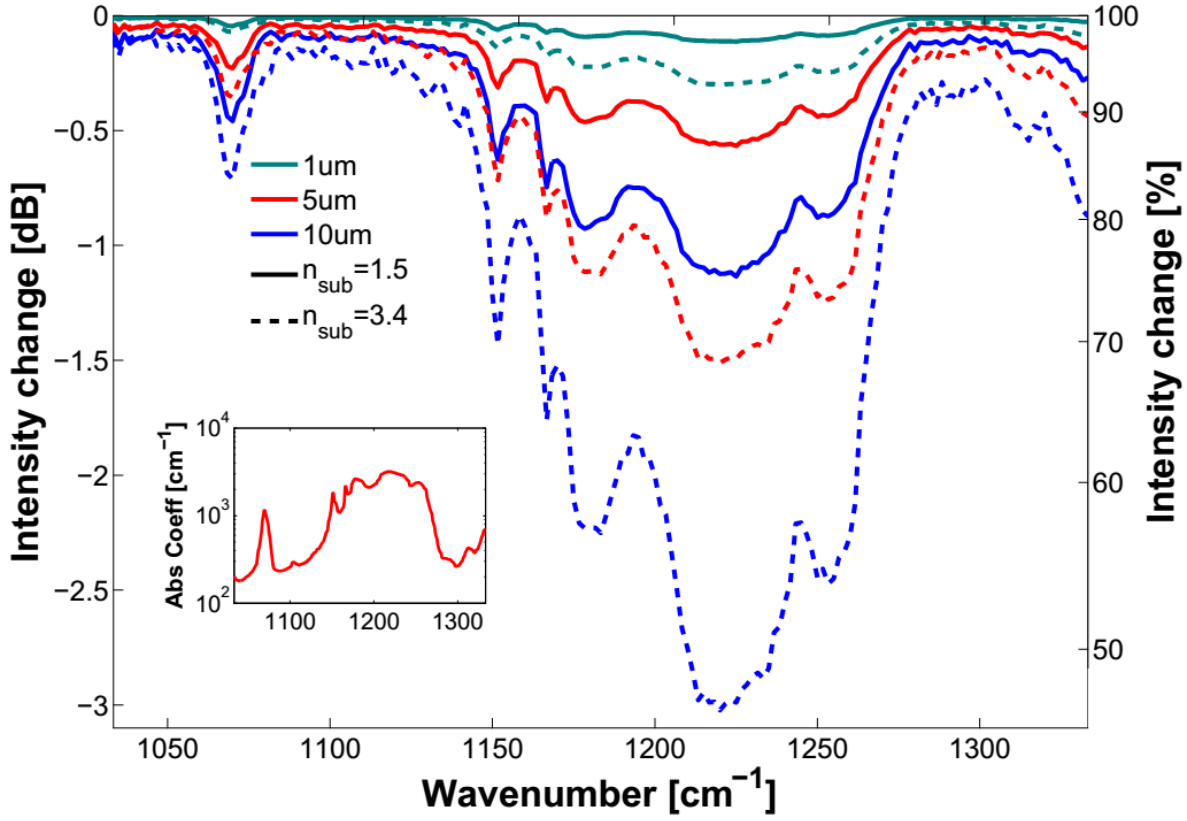

Figure 3.15: Changes in the mode intensity in dB (left axis) and percent (right axis) for an output placed 1 (green), 5 (red) and 10μm (blue) away from the input caused by the molecule for the low (full lines) and high index (dashed lines) substrate geometry. The inset represents the absorption coefficient of the analyte as derived from the transmittance in Fig.3.13 following Beer-Lambert's relation (Eq.1.25). One clearly sees that the intensity change of the modes exactly maps the absorption spectrum of the molecule. As the modes are made to propagate for longer distance between the input and output, their damping increases exponentially. Furthermore, a higher index substrate induces a stronger compression leading to an increase in the number of optical cycles per unit of length and thus in turn an increased sensitivity to the molecule/damping of the modes.

output. It is apparent that the highest index substrate leads to the finest sensitivity and this stems from the increased confinement of the modes caused by the index, as can be seen from the wavevectors in Fig.3.14. It is also further illustrated in Fig.3.16 where the absolute propagation is shown. In addition, the operation of the device is quite robust with a very small linear dependence on the top layer index as highlighted by Fig.3.17. Therefore we have proved that the device can operate with a large choice of substrates and does not require any layer indices to be matched.

At the contrary of the previous sensing methods presented before, the proposed graphene sensor does not detect a change in refractive index. Nor does it enhanced a particular vibrational line. Here, because we use propagating plasmons which are broadband compared with localized modes which are intrinsically narrowband, the complete absorption spectrum of a molecule can be acquired. Although the same results could be obtained with metallic structures, the extreme sensitivity which enables to measure a 2nm-thick diluted molecule film is entirely due to the highly confined modes found in doped graphene sandwiches.

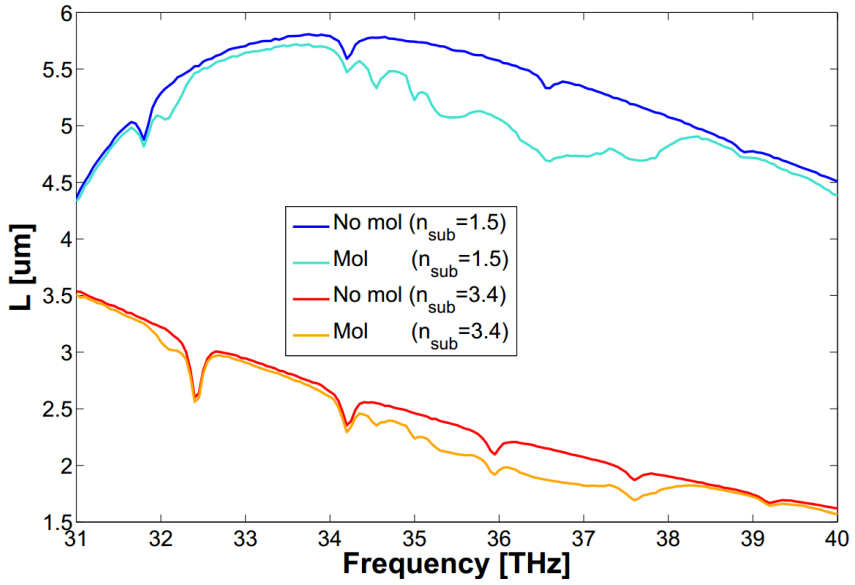

Figure 3.16: Propagation distances L, defined as the position where the intensity has decayed by 1/e along the propagation direction, for the first order A-B WG mode of a graphene sandwich sensor. The substrate index is 1.5 (dark and clear blue) or 3.4 (red and orange) for the structure without (dark blue and red) or with (clear blue and orange) a phenol-like top layer. Note the change of dispersion of L with the substrate index which originates from a redshift of the cut-off frequency thanks to the increased compression deriving from an increased index.

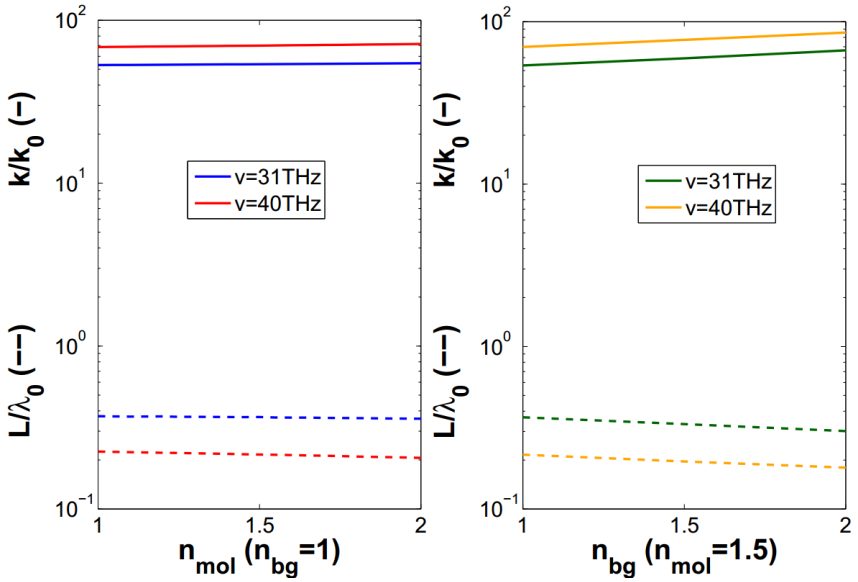

Figure 3.17: Changes in the mode confinement and propagation with changes in left) the top layer (the background having $n = 1$) or right) the whole background (the 2nm-thick top layer being fixed at $n = 1.5$) at the starting and ending frequency of the range explored. Full lines represent the normalized propagation constant (to the wavevector of light in free-space) and dashed lines the normalized propagation length (to the wavelength of light). One observes that changes in the indices only lead to moderate and monotonic shifts which can be easily averaged out by normalization to a reference channel.

3.5. Graphene Sensing

Graphene optical and electrical properties can be well estimated by Raman spectroscopy [116, 160–162] but its properties are normally accessed by electrical four-probes measurements, with possible application of magnetic fields. Here we propose an alternative optical measurement based on plasmonic sensing. Part of the results presented here were published in Ref. [163]. The idea is that the permittivity of graphene is strongly dispersive and therefore its effect on two plasmonic resonances sufficiently spaced in frequency is enough to retrieve the chemical potential and damping rate of the graphene. Fig.3.18 illustrates the

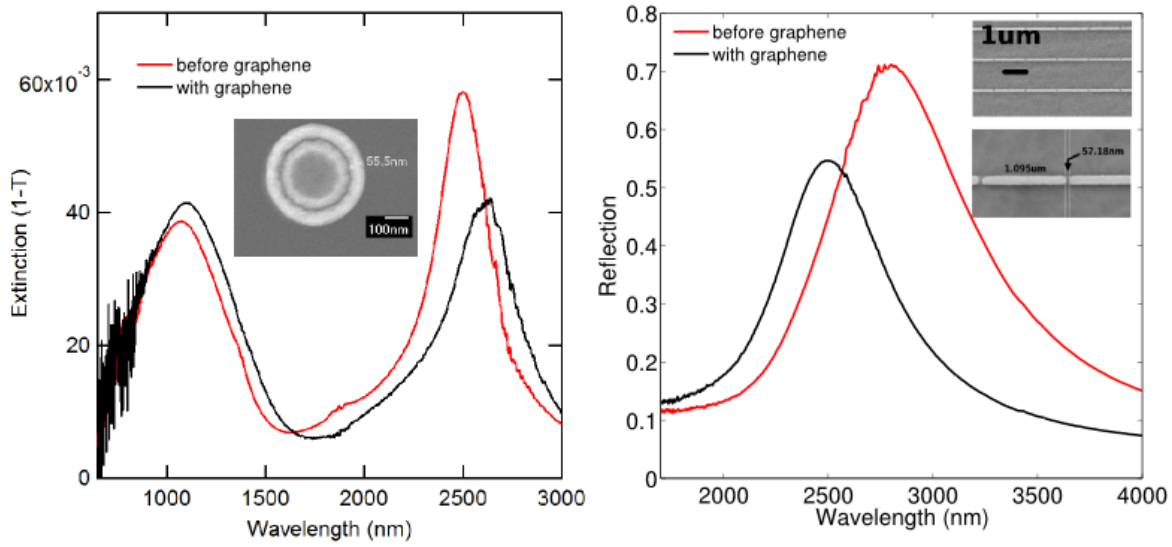

Figure 3.18: When graphene is placed on top of a plasmonic structure it can induce left) a redshift or right) a blueshift depending on its doping. Left) the structure consists in an array of ring-disk resonators with periodicity $\Lambda_x = \Lambda_y = 3\,\mu$m on a quartz substrate. The diameters of the ring [outer, inner]=[425nm, 314nm] and the diameter of the internal disk is 288nm. The gap between the disk and the ring is 13nm and the thickness of the gold is 60nm. Right) the bar array has gaps $G_x \sim 50$nm and $G_y = 1, 2\mu$m and the 20nm-thick gold was deposited on an IR-transparent BaF_2 substrate. The bars have a length $\sim 1.1\mu$m along which the light is polarized and width of 100nm (Adapted from [163]).

principle of graphene sensing, where a monolayer is placed by wet transfer on two different plasmonic structures. On the left-hand side, the graphene induces a redshift of the ring-disk cavity modes which means that its permittivity is positive in this frequency range. On the right-hand side, the graphene induces a blueshift of the bar array resonance suggesting a much higher carrier concentration for the second sample. The ring-disk structure possesses two modes called super and subradiant due to their increased and reduced radiation losses, respectively. These are well separated spectrally and with a few FEM simulations one can retrieve the optical properties of the graphene as shown in Fig.3.19. Indeed, the shift is mostly dependent on the Fermi level while the damping of the modes is related to the damping, the fitted value of $\mu = 260$meV and $\hbar\Gamma = 20$meV match with what one might expect from CVD graphene and wet-transfer on gold [163].

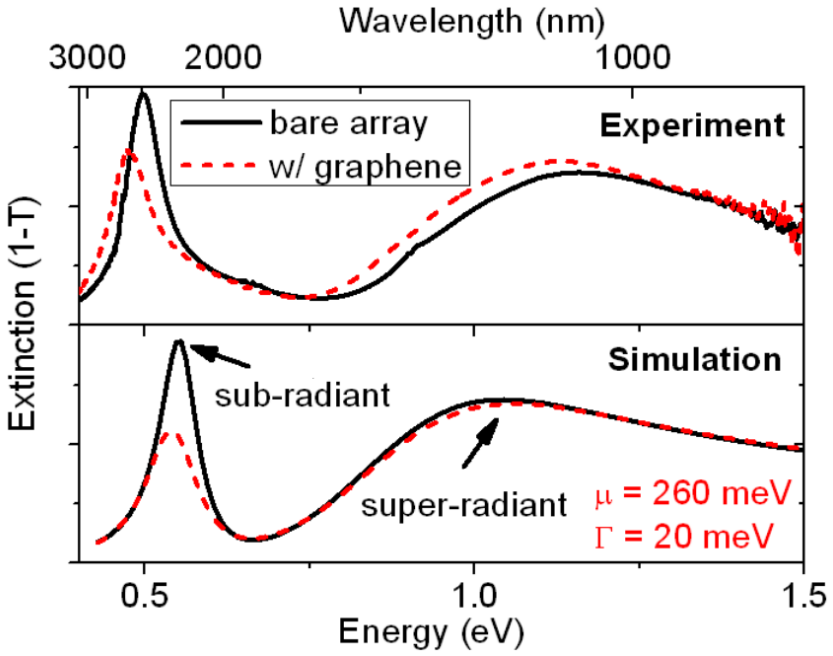

Figure 3.19: Top) FTIR measurement of the ring-disk structure presented in Fig.3.20 before (full line) and after (interrupted line) graphene coverage. Bottom) The observed shift is well reproduced by FEM simulations with a graphene having $\mu = 260$meV and $\hbar\Gamma = 20$meV (Reprinted from [163]).

This approach is straightforward but does require some numerical efforts. However, since the shift maps directly the permittivity of the graphene one could instead design plasmonic nanostructures to have resonances all along the frequency axis and therefore allow a direct reading of the chemical potential. Fig.3.20 shows the induced shifts for a few of such designed arrays where the length is increased in order for the resonance to span a large range of energies. Fig.3.21 shows the shift for all the bar arrays due to graphene coating where the X-axis corresponds to the original position of the LSPR mode E_0. Colours represents different designs while identical colours (in the same frequency range) characterize the sample homogeneity as they corresponds to four identical e-beam write. Unfortunately, shifts are expected to become higher positive as the energy is reduced due to the Drude-like dispersion of graphene at low frequencies. The high energy side makes even less sense as graphene should induce redder shifts when going to high frequencies. Subsequent Raman characterization showed a significant variation in the graphene properties and holes were even observed. Several attempts were made following this initial effort but all the graphene sheets obtained through the various providers proved highly doped and inhomogeneous preventing any successful demonstration of this principle. In the meantime, other groups showed the validity of this approach and thanks to electrostatic gating of the graphene even managed to dynamically shift plasmonic resonances [164–168].

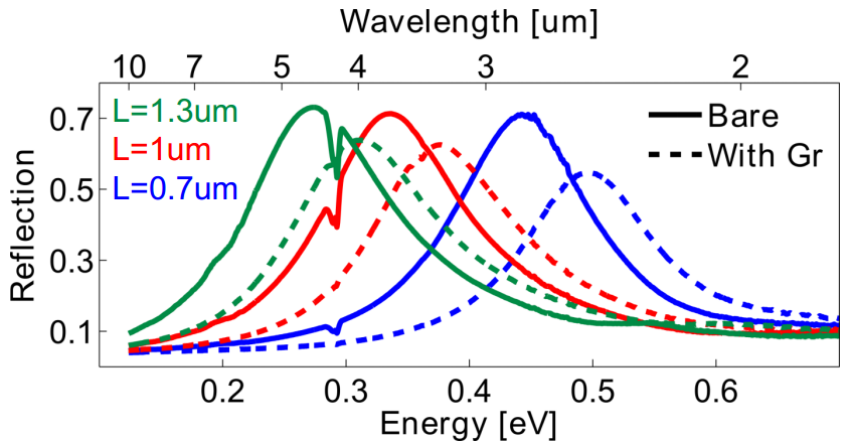

Figure 3.20: Graphene-induced shifts for gold bar arrays with different length, 20nm-thick and deposited on a BaF_2 substrate. The lateral periodicity is 1.2μm, the gap between antennae from tip to tip is 100nm and their width is 100nm. Full lines are before and dashed lines after graphene coverage. Note the atmospheric CO_2 absorption line at $\lambda = 4.25\mu$m.

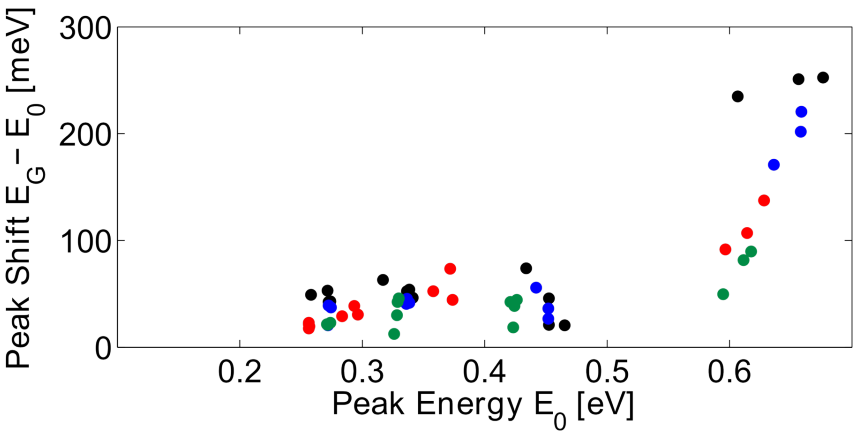

Figure 3.21: The induced shift due to graphene for the antenna arrays described in Fig.3.18 with lengths varying from 170 to 1310nm are reported. We see that the original peak position E_0 is in all cases redshifted to E_G, the plasmon peak position in presence of graphene. Unfortunately, the dispersion of the shift does not correspond to that of the permittivity of graphene which was expected, see Fig.3.1.

4. Metallic Gyroids as Self-Assembled Metamaterials

4.1. Review and Applications of Metamaterials

4.1.1. A Brief History of Metamaterials

As we stated in Sec.1.2.2.2, the interaction of a medium with an electromagnetic wave is usually fully described by the permittivity or dielectric function. This is the case because most of the time the magnetic response is very weak, approaching unity beyond the microwave regime. However, clever designs have proved to be able to engineer both the permittivity ε and the permeability μ and lead to a new class of materials called metamaterials. These man-made structures are patterned at a scale significantly smaller than the wavelength allowing an effective medium behaviour; there, the electromagnetic response is governed not any more by chemistry but by the fabricated unit cells or meta-atoms.

The ability to control ε and μ has also revived pioneering works of some Russian physicists from 1940-1970 [169] including Veselago who predicted the unusual occurrence of negative refraction when both parameters were to be negative simultaneously [170]. Even more striking was the statement by Pendry that such a piece of material would act as a perfect lens [171], relieving the microscopy community from the diffraction limited resolution $d \approx \lambda/2n$. Metamaterials continued their ascension with amazing promises for invisibility cloaking device and light concentrators [172, 173].

The first engineering of ε and μ was theoretically proposed by Pendry and co-workers based on diluted metallic wires [174] and split ring resonators (SRR) [175] in 1996 and 1999, respectively. Their experimental realisation was done by Smith *et al.* one year later [176] and negative refraction demonstrated in 2001 [177] at microwave frequencies. Reduction of the size of the SRR pushed $\mu < 0$ towards the near-infrared [178–180], but this design was very inefficient for the visible [181]. Research aimed then for a fishnet structure [182, 183] that showed eventually negative refraction at optical wavelengths [184]. Some 3D metamaterials have also started to emerge but are mostly limited to simple geometries due to the fabrication techniques [185–189]. A lot of good reviews have been written, some about metamaterials in general [190, 191], negative refractive index materials (NIM) in the visible [169, 192], negative refraction [193–196] or advances on the perfect lens [197].

4.1.2. Tricking Light

We present below a few concepts which originate from the exotic properties which can be obtained through careful structural design.

4.1.2.1. Perfection is on the Other Side

Soon after the revival of negative index materials, Pendry proposed his concept of a perfect lens [171]. The principle stems from the fact that lenses can only recover the propagating fields and lose the information contained in the evanescent larger wavevector components which are scattered by the object. This is known as the diffraction limit which states that features smaller than the wavelength cannot be resolved. Pendry's idea was that a negative index acted like negative space in which energy flow and dissipation goes in the reverse direction. The near-field information, instead of decaying, would be amplified within such a medium. There has been a long debate over the existence of such an effect in left-handed metamaterials, but experimental proofs if nothing else, finally settled the question. In Pendry's original proposal, a thin silver slab is used as a perfect lens, see Fig.4.1. There the wavevectors larger than that of free-space radiation are able to excite suface plasmons which couple on both sides leading to a recovery of the fields on the image side with intensities similar to those found at the object position. Note also that due

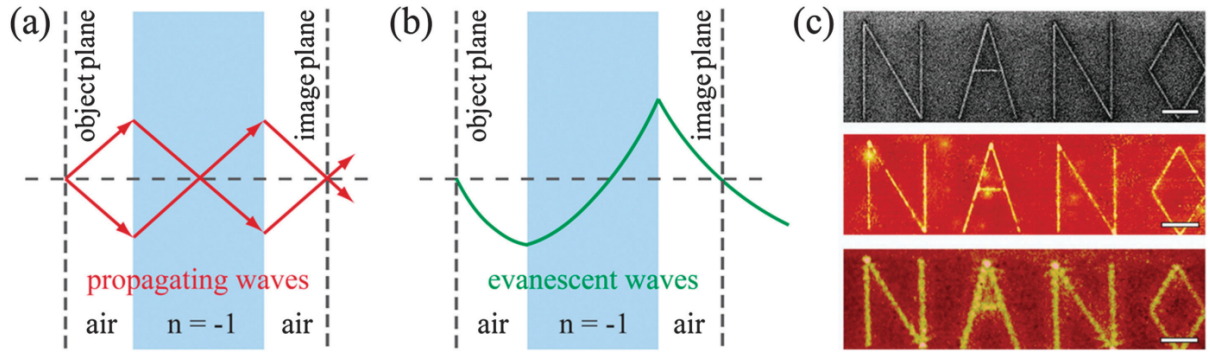

Figure 4.1: a) Focusing of the propagating scattered field and b) recovery of the evanescent components for a perfect lens made out of a negative index slab. c) Superresolution proven by lithography through a "NANO" mask (SEM image, top) with (middle) and without (bottom) a thin silver layer acting as the perfect lens (Reprinted from [191]).

to a refraction of the waves going on the "wrong" side, *i.e.* their angle of refraction is negative, slabs made out of negative index materials focus naturally any incident waves. Fig.4.1c shows the increased resolution which can be obtained with such a silver lens (middle) compared with a simple lithography step (bottom).

4.1.2.2. Gradients for Invisibility

Another important development for electromagnetic metamaterials was that of cloaking initially proposed by Pendry and Smith [172] and Leonhardt [198] independently. The invisibility cloak can be easily understood by realizing that light is always guided in the material with higher refractive index. In order to prevent light from "seeing" an object, one simply needs to create an index gradient around that object. More specifically, the concept of an optical cloaking device led to the powerful technique of transformation optics. This method considers the coordinate transform which can create a "hole" in space which will be

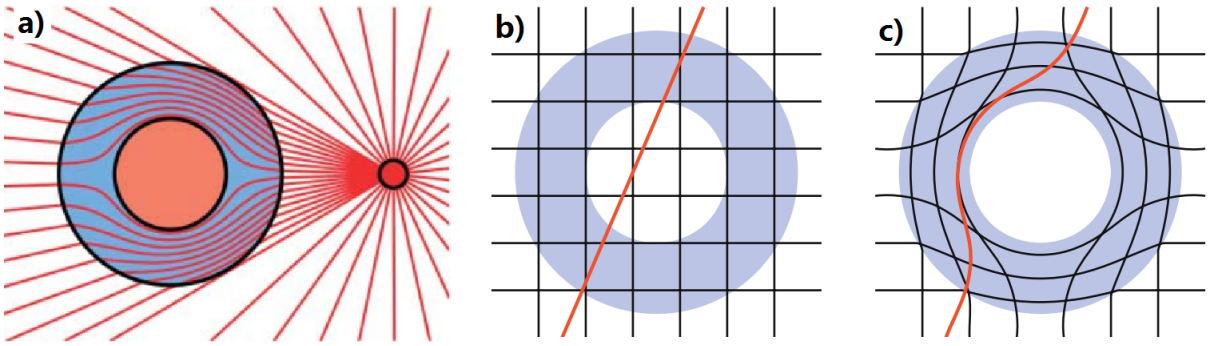

Figure 4.2: a) An electromagnetic cloak renders a similar scattering pattern than in the absence of the hollow space (Reprinted from [172]). b-c) Principle of transformation optics where a geometric transformation is applied to the material (represented by the spatial grid) in order to bend the light ray in red and leave out a hollow, invisible core (Reprinted from [199]).

the invisible spot in the final device. It then applies this transformation to the material optical properties, i.e. its permeability and permittivity, see Fig.4.2. The smaller one tries to make the cloak the stronger the gradient in the properties of the material. These can often only be obtained through a metamaterial approach and explain partly the difficulty to get cloak for the visible. Indeed, the sub-structure must be on a scale much smaller than the wavelength in order to get the desired effective properties.

4.1.2.3. Rainbows on a Standstill

Another interesting application of metamaterials is that of slow and stopped light. It normally rests on the use of gigantic refractive index which considerably decrease the group velocity of radiation. This could have an important impact on optical fibre technology where one would be able to delay or store information. Normally, one faces two issues, first, the impedance of a system is inversely proportional to its index, and therefore it is impossible to input radiation in a device with a huge permittivity and second, light tends to get imprinted in matter, for instance as polaritons, a form in which it suffers from additional losses and from which it is difficult to recover propagating fields. Tsakmakidis and Hess [200] proposed a clever approach to this problem by the mean of tapering, see Fig.4.3. In this configuration, the incoming field can enter into the device which is impedance-matched at its input, and on entering the tapered negative region, the guided wave is stopped due to interferences between the positive and negative propagating components. It is further seen that each frequency component is stored at a particular thickness of the taper.

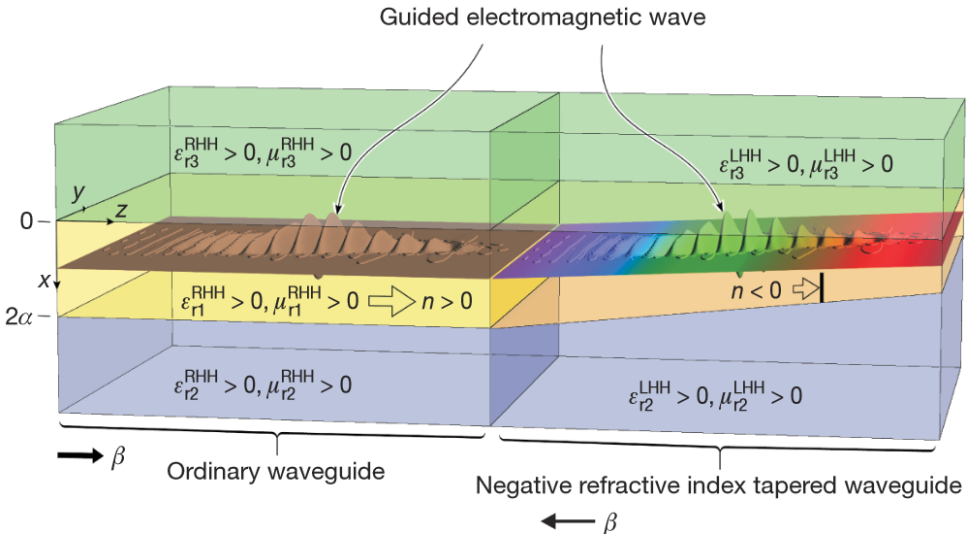

Figure 4.3: A tapered left-handed waveguide can stop and decompose a light pulse thanks to the interferences between positive and negative propagations. A guided wave packet within the ordinary waveguide is efficiently injected towards the left-handed heterostructure (LHH, while RHH stands for right handed) waveguide thanks to the tapering which allows an optimal phase matching at the junction between the two waveguides while slowing down smoothly the wave via the adiabatic reduction of its core thickness. Inside the negative index waveguide, the phase propagates in opposite direction to that of the phase within the positive index waveguide resulting in a standing, "stopped" wave. Furthermore, because of the varying core thickness, low frequencies are stopped preferably at small thicknesses and high frequencies at larger ones hence decomposing spectrally the wave packet spatially. The refractive indices numbering proceeds in descended order of magnitude so that $n_{core} > n_{top} > n_{bottom}$ (Reprinted from [200]).

4.1.3. Achieving Negative Refraction

Despite all the promising results aforementioned, these metamaterials are subjected to high losses and prevent their use for real life applications. When moving to three dimensional structures, which is the next logical step, this conclusion is even worse [201]. The high absorption is due, on one side, to the use of metals and, on a second side, the reliance on resonances. The first issue could be addressed by the addition of a gain medium that would only partly compensate for metal Joule effect [202]. The latter is a problem because resonances are associated with high dispersion and losses and only a change in the way negative parameters are achieved could possibly solve it.

Luckily, various strategies have emerged to obtain negative refraction. First, in photonic crystals, even if inhomogeneous by definition, negative bands can give rise to negative refraction when proper conditions for the iso-frequency contour and phase matching are met [196]. One can also make use of waveguides supporting surface modes which allow the fabrication of 2D metamaterials with the appealing feature of being also wide-angle NIM [203–205]. Alternatively, stacks of anisotropic layers have been known for quite a long time to exhibit particular properties and have indeed been used to create NIM in the mid-infrared [206] and visible range [207]. But the approach with more potential for 3D metamaterials is chirality. Theoretically postulated independently by Tretyakov *et al.* [208] and Pendry who proposed the now famous Swiss roll structure [209], the optical activity of chiral metamaterials was shown to lead to a negative refractive index for one polarization if the chirality was strong enough. Experimentally demonstrated, chiral metamaterials are now an expanding field of research [191, 210, 211]. Finally, a radical change in the type of materials that are used is an important direction for both the plasmonic and the metamaterial communities [33, 212].

4.2. Metallic Gyroids

Collaborating with Wiesner's group at Cornell University, gyroid metamaterials were investigated and the results shown below were published in Ref. [213]. These structures are obtained through the self-assembly of block copolymers (BCP) that have the practical aptitude to take very different morphologies depending on their composition. Of particular interest are the gyroids which are 3D continuous interwoven chiral struts, see Fig.4.4. While some calculations were done to calculate the band diagram of gyroid

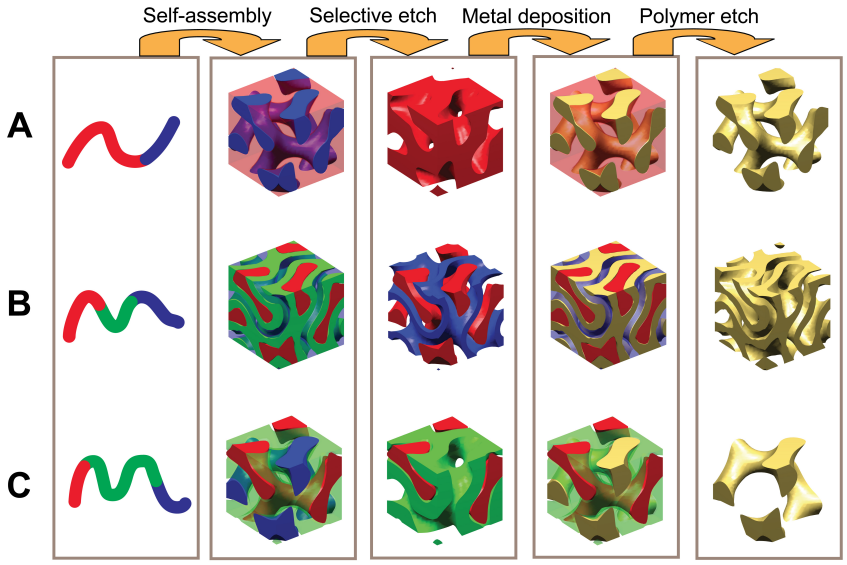

Figure 4.4: Fabrication of metallic gyroid metamaterials from BCP for A) double gyroid, B) hollow double gyroid and C) alternating gyroid: self assembly, selective etching, metal deposition and polymer total removal (Reprinted from [213]).

photonic crystals [214] and butterfly wings structures [215–217], all dielectric cases, the optical properties of metallic gyroids were unknown. We therefore investigated them, on one hand, by FDTD following the method described in Ref. [218] overlooking the loss and then by the commercial FEM software COMSOL considering the real dielectric function of the metals.

Band diagrams as calculated by FDTD for the three different geometries are shown in Fig.4.5 for the case of a Drude metal with $\omega_p/2\pi = 2.19 \times 10^{15}$Hz. One note first the presence of flat bands that are typical of metallic photonic crystals; in this regime light is rather localized but affected by high modal losses [218]. Second, low frequency light is forbidden in the alternating gyroid though the volume fraction of metal, to say 0.17, is half the one in the two other geometries, i.e. 0.34. Yet the latter allow low energy light to propagate. It is believed that in this case propagation takes place through two counter circular polarizations along each network as suggested by pictures in the near-field. This mechanism indeed would lack in the alternating structure.

Blue bands represent positive propagation while orange are for slow and red fast negative propagations. However, the backward bending of the bands is not a sufficient condition and only calculation of the

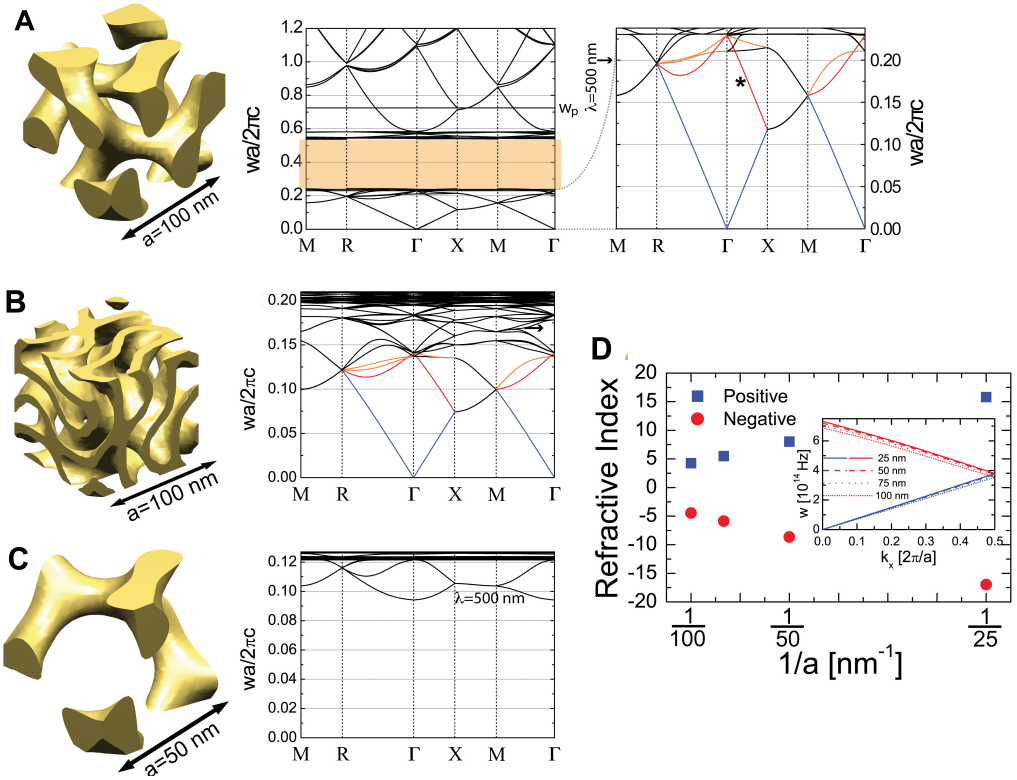

Figure 4.5: A), B) and C) band diagram for the three gyroid metamaterials with unit cell size a, blue bands state for positive propagation while orange and red are for slow and fast negative propagations respectively, D) refractive index (*i.e.* kc/ω) as a function of a for the double gyroid for the two first bands along $\Gamma - X$, the inset shows that these two bands are left unchanged by the change of a (Reprinted from [213]).

Poynting vector can determine for sure whether negative refraction is occurring or not. Hopefully, the Drude metal without loss shows such a behaviour and thus could be of interest as a negative index material in the visible. Nevertheless, losses have to be considered and using the experimental permittivities for silver, gold and aluminium revealed a quite disappointing outcome, see Fig.4.6. Indeed, it appears that the absorption due to interband transitions in gold destroys the negative refraction, which is a situation known to be problematic for metamaterials [183]. Silver is much less lossy and there the wave and Poynting vectors are anti-parallel, characteristic of negative refraction. Also, surprising is the propagation in aluminium gyroids, where the large real part of *varepsilon* results in a very small skin depth preventing the light to suffer too much from its high absorption and allows negative propagation. Most probably negative refraction is caused in these gyroid structures by the usual combination of permeability resonance due to the capacitance and mutual induction between the two conductive struts [175] and a negative permittivity as found in metals below their plasma frequency.

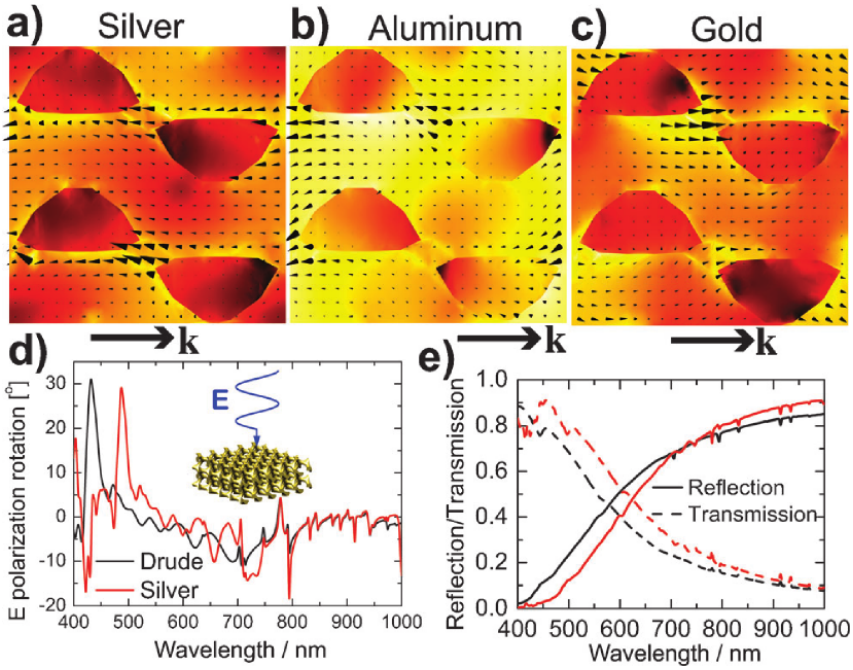

Figure 4.6: a), b) and c) intensity near-field cuts (black is minimum, white maximum) through a unit cell showing the energy flow (Poynting vector, black arrows) for double gyroids made out of real metals. The large black arrows below the figures show the direction of the wavevector. In a left-handed (*i.e.* negative index) material, the Poynting and wave vectors are colinear like in a conventional right-handed medium, but the energy flows in opposite direction to that of the wave propagation direction. This condition is met for the case of silver and aluminium where the limited loss or small skin depth, respectively, does not destroy the effect of negative refraction. At the opposite, the strong interband damping in gold within the visible range destroys the left-handness and the Poynting and wavevectors point in the same direction. d) Rotation angle of linearly polarized light passing through a two unit cells stack of the alternating gyroid and e) reflectance and transmittance of such stack for a lossless Drude metal (black) and silver (red). One can observe strong peaks in the rotation angle which corresponds to allowed bands in Fig.4.5C and an increased reflection/decreased transmission as the frequency decreases below the bandgap energy (Reprinted from [213]).

As we mentioned before, the alternating gyroid forbids the propagation of low frequency light. In

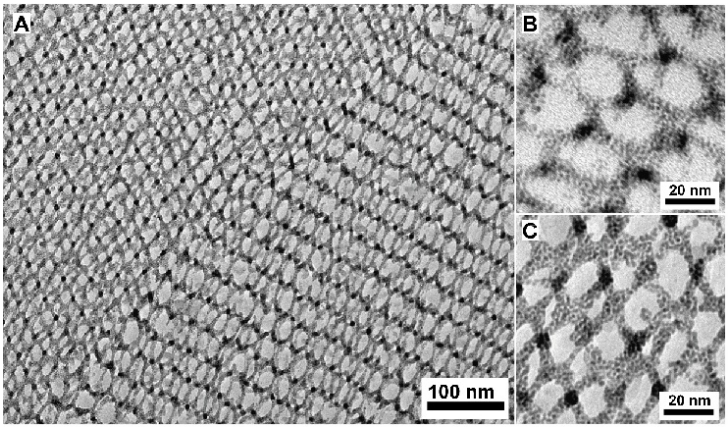

Figure 4.7: TEM images of organic-metallic NP hybrid gyroid film with Pt NPs fraction weight of 22.8% B) before and C) after a 10min plasma treatment. A) An extent of the film after treatment showing that order is well preserved.

addition, it is a chiral structure and therefore will reflect light which is circularly polarized anti-clockwise compared to its structure. When light is linearly polarized though, it can be transmitted as shown in Fig.4.6e, where reflection gets stronger at energies below the band gap ($\lambda = 555$nm). The chirality makes the gyroid optically active and in consequence the direction of the electric field of light will rotate as it passes through the structure, see Fig.4.6d. One can also observe the effect of the constituting material and the appearance of strong rotations at particular frequencies corresponding to the bands in 4.5C.

The metallisation of the structure is achieved through the selective etching of one of the block copolymer, followed by electro-deposition and removal of the remaining organic material, see sketch in Fig.4.4. An alternative method is to mix metallic NPs into block copolymers, similar self-assembly processes to pure BCP happen and there is no need of tedious and time-consuming electro-deposition or back-filling. The resulting samples can be of high quality and macroscopic size as confirmed by TEM imaging (Fig.4.7, note that the unit cell is 50nm and thus the features reach a much smaller scale). A final pure metal structure can then be obtained by sintering, burning off the organic chemicals.

Steiner's group in Cambridge is also working on metallic gyroids and their first measurements do indeed show chirality [219, 220]. Our experimental attempts were based on thin slices obtained by cryo-microtoming of thicker samples. FIB was also planned at a later stage. Unfortunately, the structures obtained did not exhibit order and homogeneity on a scale large enough to allow their property measurements. Nevertheless, prospects are highly appealing as layers of such materials could be used as thin perfect lens. Before metallisation or sintering, they are even flexible and so could conform with any surface. The alternating gyroids can also be used as thin, cheap waveplates. Finally, the fabrication procedure, being based on self-assembly, is completely upscalable at the contrary of structures prepared by lithography.

5. An Analytic Fano Theory to Understand Some Aspects of Nanophotonics

5.1. Review and Applications of Fano Interferences

Fano interferences have a long history in physics and were described long ago by Majorana [221, 222] and Fano [223, 224]. These are often recognized by their asymmetric lineshape but can be observed whenever two coupled resonances are close enough spectrally speaking. Famous in some area of physics such as atomic physics, quantum transport or scattering theory, it is getting widely observed nowadays in nanostructures [225–232]. Because it is commonly encountered in plasmonics with plasmon resonances acting as continuum and sharp states arising from emitters, dark states or diffractive modes for instance, there is a strong impulse to rewrite the original Fano theory for the particular case of plasmonics [57, 229–231, 233–235]. It is also observed in SEIRA experiments [58, 59, 62, 65] where the narrow absorption line of a molecule interacts with the broad plasmonic resonance of metallic islands or structures [51, 60, 61, 64, 68–70, 236].

Fano resonances take place in a very narrow frequency window in which both complete suppression and enhanced transmission can occur. This translates into a very sharp phase change across the resonance which is of critical importance for optical switching and sensing [48, 227, 228, 237]. However, due to their omnipresence in nanophotonics it is above all of fundamental interest to understand and be able to predict the conditions in which they arise. These resonances explain for instance the particular lineshapes that are observed when different plasmonic states close enough spatially and spectrally hybridize [20, 47, 48, 238–245] or when diffraction modes couple with SPP like in extraordinary optical transmission [246–249]. It can also be seen when LSPP couples with lattice resonances [250–252], waveguide mode [253, 254], diffraction mode [255] or SPP [256]. Finally symmetry breaking [257–262] and electromagnetically induced transparency [237, 263–265] are of such interferences as well.

Many attempts have been made to adapt the original Fano theory to particular cases allowing to use it in a more straightforward manner. However, these have revealed to be either oversimplificating, resulting in the well-known Fano profile with q and $\mathcal{E}$ to be fitted numerically, or at the contrary filled with additional parameters which values are impossible to identify physically. Recurrent methods also include classical oscillators models [236, 266–268], coupled mode theory [269, 270], scattering theory [271, 272] or even transfer matrix approach [253].

In what follows, we apply Fano theory to the particular case of plasmonic resonances in interaction with discrete states and arrived at a very synthetic and simple analytical formula. It allows a good

understanding of this phenomenon and can be used to design clever nanostructures with very fine tuning of the optical response of such systems [273, 274]. The results presented below were published in Ref. [229, 232].

5.2. Original Fano Theory

Fano formulated his complete theory of "configuration interaction" in 1961 in order to explain the particular excitation spectrum during the auto-ionization of helium [224]. He considered the interaction of a discrete state with a continuum, calculating the resulting energy spectrum.

Let $|d\rangle$ be the discrete (DS) and $|c\rangle$ the continuum (CS) states, we have

$$\langle d|\,\mathcal{H}_0\,|d\rangle = E_d \tag{5.1a}$$

$$\text{and } \langle c|\,\mathcal{H}_0\,|c'\rangle = E\delta(E-E') \tag{5.1b}$$

for the unperturbed Hamiltonian where the orthonormalization within the continuum gives $\langle c|\,c'\rangle = \delta(E-E')$. The coupling V between the states reads

$$\langle c|\,V\,|d\rangle = v(E), \tag{5.2a}$$

$$\text{and } \langle c|\,V\,|c\rangle = \langle d|\,V\,|d\rangle = 0; \tag{5.2b}$$

We want to solve the eigenvalue problem $\mathcal{H}\,|\Psi\rangle = E\,|\Psi\rangle$, where $\mathcal{H} = \mathcal{H}_0 + V$ and $|\Psi\rangle$ is the mixed state resulting from the interaction between the DS and the CS. The first step is to project $\mathcal{H}\,|\Psi\rangle$ onto $|c\rangle$ and $|d\rangle$ making use of the closure relation

$$\mathbb{I} = |d\rangle\langle d| + \int |c\rangle\langle c|\,\mathrm{d}E \tag{5.3}$$

which leads

$$\begin{aligned} \langle c|\,\mathcal{H}_0\,|\Psi\rangle + \langle c|\,V\,|\Psi\rangle &= \langle c|\,E\,|\Psi\rangle \\ E\,\langle c|\Psi\rangle + \langle c|\,V\,|d\rangle\,\langle d|\Psi\rangle + \int \langle c|\,V\,|c\rangle\,\langle c|\Psi\rangle\,\mathrm{d}E &= E'\,\langle c|\Psi\rangle \\ v(E)\,\langle d|\Psi\rangle &= (E'-E_d)\,\langle c|\Psi\rangle \end{aligned} \tag{5.4}$$

and

$$\begin{aligned} \langle d|\,\mathcal{H}_0\,|\Psi\rangle + \langle d|\,V\,|\Psi\rangle &= \langle d|\,E\,|\Psi\rangle \\ E_d\,\langle d|\Psi\rangle + \langle d|\,V\,|d\rangle\,\langle d|\Psi\rangle + \int \langle d|\,V\,|c\rangle\,\langle c|\Psi\rangle\,\mathrm{d}E &= E'\,\langle d|\Psi\rangle \\ \int v(E)^*\,\langle c|\Psi\rangle\,\mathrm{d}E &= (E'-E)\,\langle c|\Psi\rangle \end{aligned} \tag{5.5}$$

Working further with Eq.5.4 and 5.5 following the method used by Fano, the new mixed state is expressed as

$$|\Psi\rangle = \frac{v(E)\Big(\,|d\rangle + |\Omega\rangle\,\Big) + \Big(E'-E_d-\Delta\Big)\,|c'\rangle}{\sqrt{(E'-E_d-\Delta)^2 + (\Gamma_m(E')/2)^2}} \tag{5.6}$$

with

$$\Gamma_m(E) = 2\pi|v(E)|^2 \tag{5.7a}$$

$$\Delta = \mathcal{P}\int \frac{|v(E)|^2}{E' - E}\mathrm{d}E \tag{5.7b}$$

$$|\Omega\rangle = \mathcal{P}\int \frac{v(E)}{E' - E}\,|c\rangle\,\mathrm{d}E \tag{5.7c}$$

where $\Gamma_m(E)$ is the modified linewidth of the DS, and Δ and $|\Omega\rangle$ are the spectral shifts of the CS and DS, respectively. $\mathcal{P}$ indicates the Cauchy principal part of these undefined integrals. The interferences effects appear then when such mixed state is excited from another initial state $|i\rangle$. Indeed in that case the spectrum is given by the ratio of the probability to excite the mixed state to the one of exciting the unperturbed CS, i.e.

$$\frac{|\langle i|\,W\,|\Psi\rangle|^2}{|\langle i|\,W\,|c\rangle|^2} = \frac{(\mathcal{E}+q)^2}{\mathcal{E}^2+1} \tag{5.8}$$

with

$$\mathcal{E} = \frac{E - E_d - \Delta}{\Gamma_d(E)/2} \tag{5.9a}$$

$$q = \frac{\langle\Phi|\,W\,|i\rangle}{\pi v(E)^*\,\langle c|\,W\,|i\rangle} \tag{5.9b}$$

where W is the coupling with $|i\rangle$, $\mathcal{E}$ the reduced energy and $\frac{1}{2}\pi q^2$ the ratio of the probability to excite the modified DS $|\Phi\rangle = |d\rangle + |\Omega\rangle$ to the one of exciting a bandwidth Γ_d of unperturbed CS. The lineshapes described by Eq.5.8 are the famous asymmetric Fano profiles, see Fig.5.1a, which are composed of a peak and a dip very close spectrally speaking. Variation in the coupling between the two original states represented by q can give rise to asymmetric or symmetric profiles with resonant enhancement or suppression [224, 229, 275].

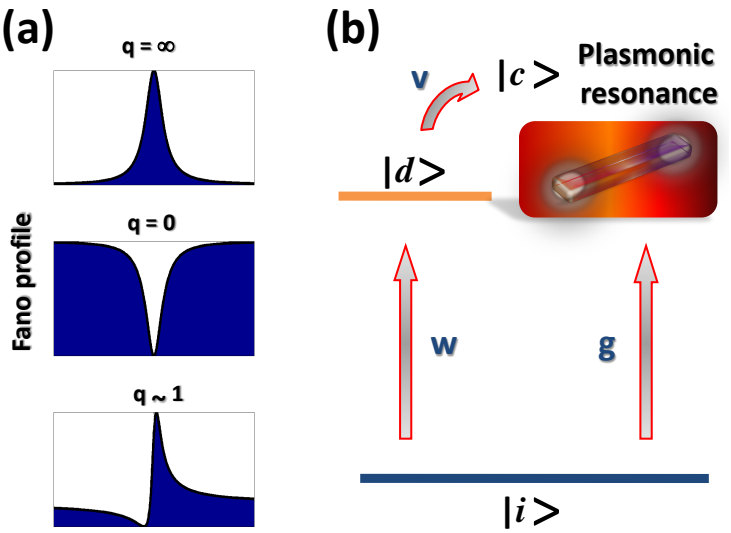

Figure 5.1: a) Fano profiles obtained from Eq.5.8 for three extreme values of the q parameter, b) energy diagram and coupling factors between one plasmonic continuum $|c\rangle$, a discrete state $|d\rangle$ and an initial state $|i\rangle$ (Reprinted from [229]).

5.3. Analytical Fano Model

At the contrary of past approaches, we choose now to draw on the original Fano theory but applying it to the case of plasmonics. Let the CS $|c\rangle$ be a plasmonic resonance, see Fig.5.1b, which can be regarded as such because it is much broader than the DS $|d\rangle$ with which it interacts through the coupling V, both interacting with an incident photon $|i\rangle$ through W. The DS can be, just to name a few, a dark resonance, the absorption line of a molecule or the excitation of a diffraction or guided mode with the only requirement of being sharp compared to $|c\rangle$. The only assumption that we will make is that we know that the excitation of $|c\rangle$ follows a Lorentzian shape with a linewidth Γ_P and peak at E_P

$$\mathcal{L}(E) = \frac{1}{1 + \left(\frac{E-E_P}{\Gamma_P/2}\right)^2} \tag{5.10}$$

Taking the DS as origin, i.e. $E_d = 0$, the matrix elements read

$$\langle c| V |d\rangle = v\sqrt{\mathcal{L}(E)} \tag{5.11a}$$

$$\langle i| W |d\rangle = w \tag{5.11b}$$

$$\langle i| W |c\rangle = g\sqrt{\mathcal{L}(E)} \tag{5.11c}$$

When those are substituted into Eq.5.6 and the integrals are solved by the residue method, the equations beautifully simplify to the analytical expressions

$$F(\mathcal{E}) = \frac{|\langle i| W |\Psi\rangle|^2}{|\langle i| W |c\rangle|^2} = \frac{(\mathcal{E}+q)^2}{\mathcal{E}^2+1}, \tag{5.12a}$$

$$q = \frac{vw/g}{\Gamma_d(E)/2} + \frac{E-E_P}{\Gamma_P/2}, \tag{5.12b}$$

$$\mathcal{E} = \frac{E}{\Gamma_m(E)/2} - \frac{E-E_P}{\Gamma_P/2}, \tag{5.12c}$$

where $\Gamma_m(E) = 2\pi v^2 \mathcal{L}(E)$ is the modified linewidth of the discrete state and E the incoming photon energy. Actually, for the case of a flat continuum $\mathcal{L}(E) = 1$ and Γ_d is the half-width of the DS as obtained from Fermi's golden rule. Eqs.5.12 recover the classical Fano profile but now q and $\mathcal{E}$ are expressed out of the plasmonic properties (E_P, Γ_P). As one can see, the whole physics of the interference is thus described by three coupling parameters v, w and g, see Fig.5.1b [229, 232].

The task consists then in relating these parameters to some physical properties of the system as we will show below. In order to do so we analyse the extinction spectra which here are calculated numerically but which could be measured experimentally as well. This quantity is proportional to the probability of directly exciting the mixed state $|\Psi\rangle$ with the incident photon $|i\rangle$ (see Eq.5.12a)

$$|\langle i| W |\Psi\rangle|^2 = \frac{(\mathcal{E}+q)^2}{\mathcal{E}^2+1} \times |\langle i| W |c\rangle|^2 = F(\mathcal{E}) \times g^2\mathcal{L}\ . \tag{5.13}$$

In presence of absorption, which in quantum mechanics translates as an incoherent process that does not contribute to the interference but adds as a background, the previous equation reads

$$|\langle i|\, W\, |\Psi\rangle|^2 = \Big(F(\mathcal{E}) + A\Big) \times g^2\mathcal{L} = g^2\mathcal{L} \times F(\mathcal{E}) + g^2\mathcal{L} \times A = F'(E)\ . \tag{5.14}$$

Here $g^2\mathcal{L}$ is the direct excitation of the bright mode which couples to light and can be related therefore to σ_{scat} while the non-radiative part given by $g^2\mathcal{L}A$ where no interference is present has to be the absorption of the system linked to σ_{abs}. In summary, $F'(E)$ is equal to the extinction cross-section

$$Ext = \sigma_{scat} \times F(\mathcal{E}) + \sigma_{abs} \tag{5.15}$$

except for a normalization factor C that arises because the probability ratio $F(\mathcal{E})$ (see Eq.5.12a) is unitless [229, 232].

5.4. Analytical Fano Applied to Nanophotonics

5.4.1. Plasmon-Absorber Coupling

To illustrate the ease of use and power of this new formulation of Fano resonances, let us look at the interaction between an antenna array and an absorber illuminated with a plane wave [261, 276], see Fig.5.2a and b. The absorber is chosen as PMMA which absorbs at $E_d = 5.78\mu\text{m}=1730\text{cm}^{-1}$ arising

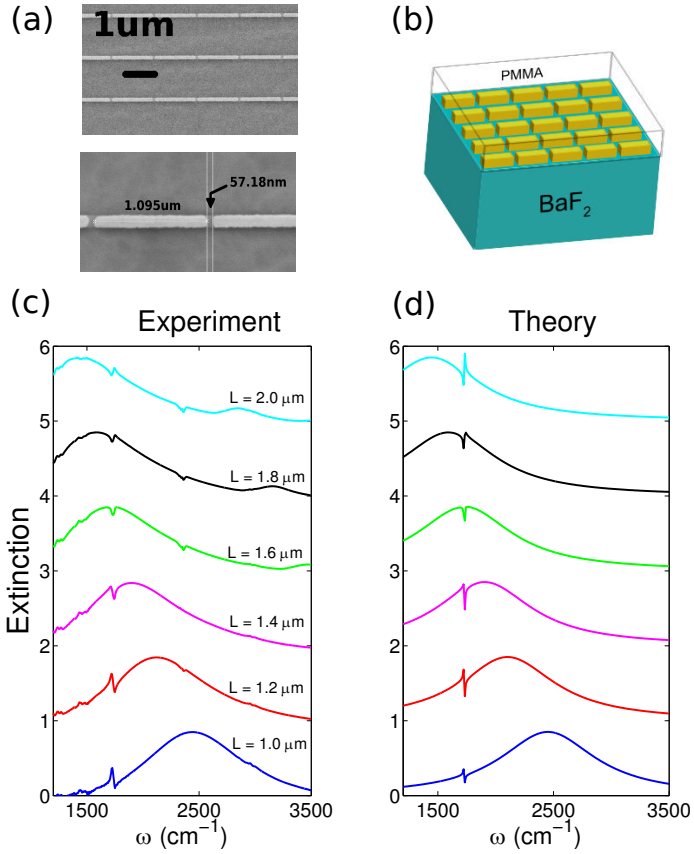

Figure 5.2: (a) Scanning electron microscope top view image of a 20nm-thick array of gold nanoantennae prepared by electron beam lithography. (b) Schematic representation of the array covered with PMMA on a BaF_2 substrate. (c) Measured and (d) calculated (with Eq.5.15) extinction of an array of nanoantennae as a function of the frequency ω and the nanoantenna length L. The incident light is polarized parallel to the long axis of the antennas. Note also the atmospheric CO_2 absorption line at $\sim 2400\,\text{cm}^{-1}$ which is separated from the array by the PMMA layer thus preventing coupling and interferences (Reprinted from [229]).

due to the C=O bond stretching. In this situation, the molecular absorption line is very sharp and the plasmonic resonance (PR) of the antenna array can be accurately considered flat at the scale of the sharp mode. The coupling factor g is given by the probability to excite the broad state with a plane wave, which is simply the PR linewidth and thus $g^2 = \Gamma_P/2\pi$. Since the continuum is nearly flat, the excitation of the discrete state v is well approximated by Fermi's golden rule $v^2 = \Gamma_d/2\pi$, *i.e.* it behaves

as if placed in free-space hence its excitation probability is directly related to its linewidth. Also, since we are illuminating with a low power source, the excitation and emission are obtained through Einstein's coefficients leading to $w \sim v^2$; note that because of the continuum normalization it is v^2 and g^2 that have dimensions of an energy. In order to investigate the Fano profile, the antennae length is varied to span the collective resonance across the PMMA absorption line. Fig.5.2c and d compares FTIR measurements with the analytical formula presented above and the aforementioned parameters. It can be seen that the Fano lineshape is changed from asymmetric to symmetric depending on the relative position of E_P and E_d. All the interference lineshapes are very well reproduced within our analytical framework leading to a remarkable agreement between calculated and measured spectra proving the power of this formulation. This is particularly true considering that no fitting parameters are required and the asymmetry is solely governed by the relative position without modification of the coupling parameters [229].

5.4.2. Plasmonic Crystals

To demonstrate further the simplicity and usefulness of Eqs.5.12 we will turn now to three cases of current interest to the plasmonic community. Lattice resonances are surface waves arising from the hybridization between the collective scattering of NPs arranged in a periodic fashion with the in-plane diffracted wave at the Rayleigh anomaly [250–252, 277–281]. The resulting profile is strongly affected by the offset between the NPs LSPR peak and the Rayleigh position at $\lambda_d = \Lambda \times n$. When the LSPR lies on the blue side for instance, the overall linewidth can be significantly reduced. This is an efficient way to reshape LSPR for sensing applications. Here, the broad mode is the scattering cross-section of a single particle (dashed blue line in 5.3a) and its excitation is as before taken as $g^2 = \Gamma_P/2\pi$. The discrete mode is the diffracted wave tangential to the array plane and its direct excitation is mediated by the cooperative Rayleigh scattering of the NPs. However, since this one is much smaller than the total scattered field, w is taken small ~ 0. Last, the coupling between the two modes v is unknown and chosen similar to g at first approximation. FDTD calculations (black lines) for a square array of gold NP with $R = 50$nm and unit cell b) $\Lambda^2 = 450 \times 450$ and c) 350×350nm^2 are shown in Fig.5.3. Dashed red lines are the spectra obtained with the above parameters and Eq.5.15 and dotted blue lines with slightly modified parameters to reach a better accordance. It can be seen that even the red curves reproduce very well the physics for the $\Lambda^2 = 450 \times 450$nm^2 case. At the opposite, the second case is pretty inaccurate. Indeed the formula predicts a peak while there is only a dip. Actually, it has been proven that when the LSPR is at smaller energy than the diffraction edge, little radiative coupling can occur and therefore the interference phenomenon is only marginal [231, 237, 239]. This means we are assuming an interference effect when it is barely present [232].

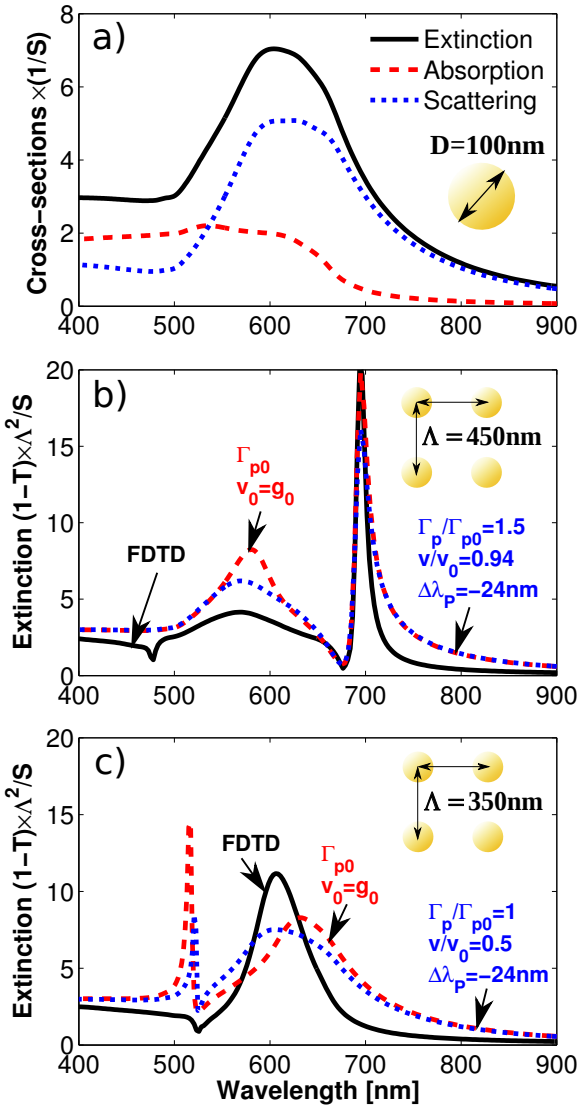

Figure 5.3: a) Normalized (to $S = \pi \times R^2$) extinction (full black), scattering (dotted blue) and absorption (dashed red) cross-sections of a 50 nm-radius gold sphere calculated by FDTD. b-c) Normalized (to S/Λ^2) extinction ($1 - transmittance$) of the same nanoparticle arranged periodically along X and Y with b) $\Lambda = 450$ nm and c) 350 nm. The full black lines are FDTD results and dashed red obtained by $Ext = \sigma_{scat} \times F(\mathcal{E}) + \sigma_{abs}$ with $F(\mathcal{E})$ from Eqs.5.12. All the parameters are taken from the single sphere cross-sections with $g_0 = \sqrt{\Gamma_P/2\pi}$, $v_0 \sim g_0$ and $w \sim 0$. For the dotted blue curves, E_P, Γ_P and v have been slightly amended to show better accordance with the FDTD results (see plots for full details, reprinted from [232]).

5.4.3. Dark-Bright Interferences

Another fascinating effect is observed in dolmen nanostructures. There, a careful design can lead to the interference between dark and bright modes resulting in what is known as electromagnetically induced transparency (EIT) [47, 229, 237, 263, 264, 276, 282]. To build such structure, we will consider two sets of parallel silver nanobars the first exhibiting a dipolar (first order) resonance that spectrally matches with the quadrupolar (second order) of the second. To do so, the length of the former is chosen as 75nm and the one of the latter as 200nm, see Fig.5.4. The quadrupolar of the long antennae is dark and can only be observed by breaking the symmetry like at tilted incidence (compare the dashed red and dotted blue lines). By assembling the two pairs perpendicular to each other like in the inset of Fig.5.5, with the short antenna aligned with the incident electric field, we insure the quadrupolar can only be excited through near-field coupling. Here the broad state is the bright dipolar mode of the short antennae pair and as usual its excitation is given by $g^2 = \Gamma_P/2\pi$. The direct coupling to the dark quadrupolar resonance is symmetry forbidden and so $w = 0$. Again, the interaction strength is unknown and will be taken at first as $v^2 \sim \Gamma_d/2\pi$. Fig.5.5 shows the extinction cross-section of this dolmen with a varying gap between short antennae side and long antennae tips from a) $G = 20$ to b) 10 and c) 5nm as calculated by FDTD (solid black lines). The red dashed curves are the spectra obtained with the formula and the arbitrary v. The agreement is rather bad and one could extrapolate that for bigger gap, the lineshapes may eventually merge. This is because the value of v which expresses the coupling is too weak, indeed when the gap becomes small there is a strong coupling, *i.e.* v increases when the gap decreases, see for example the near-field in Fig.5.6a. The dotted blue lines in Fig.5.5 are also calculated with the formula but now v is tuned to reproduce the numerical results. Note that E_P and E_d are also slightly modified to account for the mutual influence of the pairs. These final spectra are much more satisfying and the obtained values for v can be used to get some physical insight. Fig.5.6b reports the fitted values of v^2 in function of the gap G. Since we know the interaction between the dark and bright modes is mediated by near-field coupling, the electric field strength in the gap is also plotted in the same figure. Very interestingly, the two quantities are seen to follow exactly the same trend: inversely proportional to the gap. Hence, it appears clearly after a simple parameter study by the means of Eqs.5.12 that the best way to control the EIT in the presented structure is to work on the near-field coupling within the gaps [232].

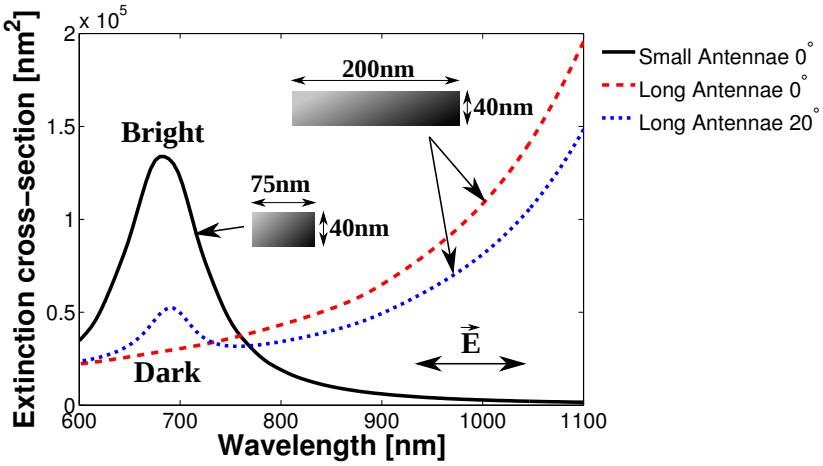

Figure 5.4: Extinction cross-sections of the long (dashed red) and short (full black) antennae pairs at normal incidence. The dipolar resonance of the latter is matched to the second order resonance of the former that can only be excited when the symmetry is broken, here *via* a tilted illumination of 20° (dotted blue). The long antennae also support a dipolar mode that is located in the near infrared which explains the increase of their extinction towards longer wavelength (Reprinted from [232]).

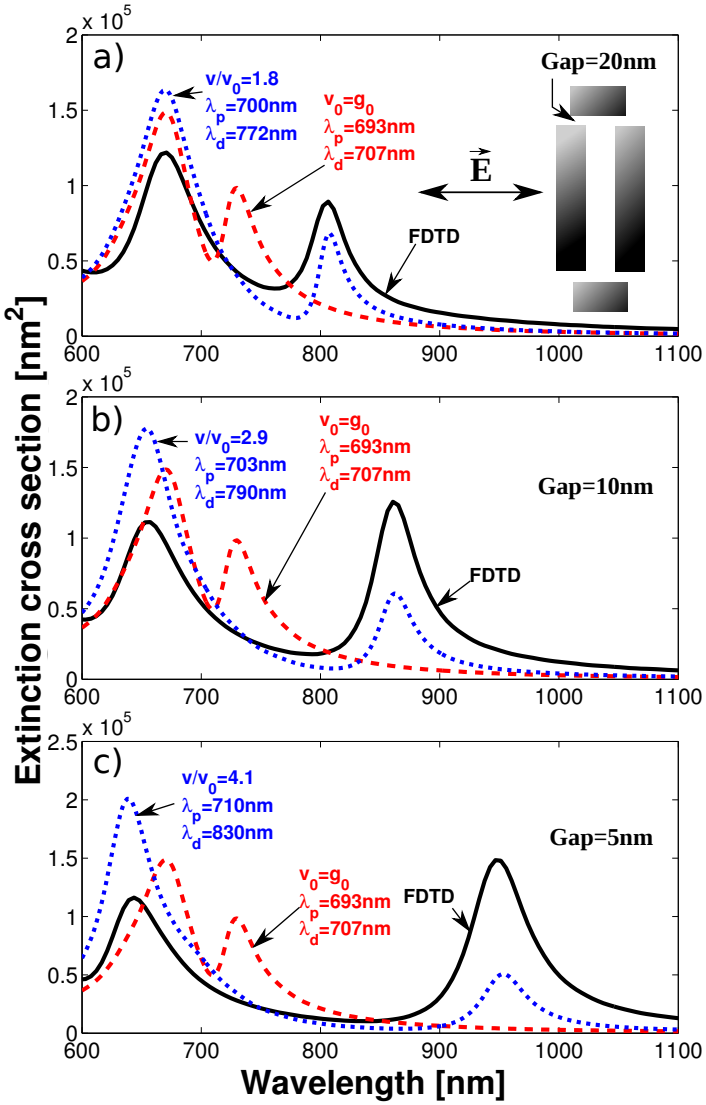

Figure 5.5: Extinction cross-sections of the dolmen structure for a gap $G = 20$ nm (a), 10 nm (b) and 5 nm (c). The full black lines are FDTD calculations, the dashed red curves are obtained by $Ext = \sigma_{scat} \times F(\mathcal{E}) + \sigma_{abs}$ with $F(\mathcal{E})$ from Eqs.5.12. All the parameters are taken from the cross-sections of the uncoupled antenna pairs with $g_0 = \sqrt{\Gamma_P/2\pi}$, $v_0 \sim \sqrt{\Gamma_d/2\pi}$ and $w = 0$. For the dotted blue curves, E_d, E_P and v have been modified to fit the FDTD results (see plots for full details, reprinted from [232]).

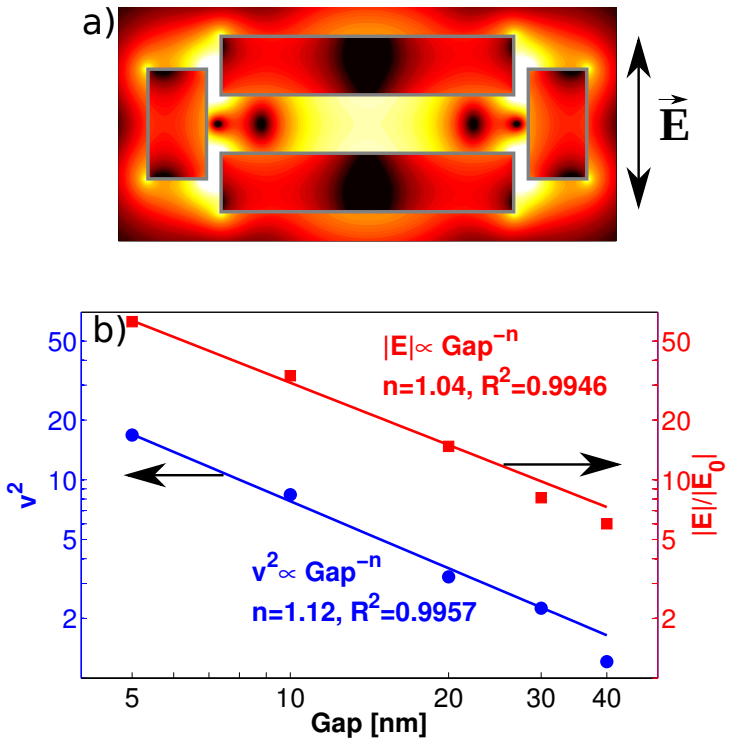

Figure 5.6: a) Near-field cut at mid-height of the nanostructure shown in the inset of Fig.5.5b with $G = 10$ nm showing the electric field intensity at 860 nm on a logarithmic scale (the outline of the structure is drawn in grey). b) Coupling factor v^2 and electric amplitude, $|E|$, in the middle of the gap at the second peak in function of the gap G on a log-log scale. The blue and red lines represents the fits $v^2 = 103 \times G^{-1.12}$ and $|E| = 339 \times G^{-1.04}$ with correlation coefficient $R^2 = 0.9957$ and 0.9946, respectively (Reprinted from [232]).

5.4.4. Oligomers

Last, the hybridization theory has become ubiquitous in plasmonics where it is used to describe and explain the spectra of strongly interacting nanosystems [48, 238, 240–243, 259, 273, 274, 283–286]. As an example, let us look at the lineshape of a heptamer of gold nanoshells with silica core embedded in a silica disk [height, diameter]=[10nm, 85nm] as shown in the inset of Fig.5.7. For shells with [inner, outer] diameters of [60nm, 80nm] and gaps between closest neighbours of 5nm, FDTD calculations give the full black line in Fig.5.7a. While numerical methods are accurate into predicting complex profiles such as this one, the whole interference effect is hidden and the understanding of the ongoing physics as well. Our Fano formulation can provide key insight in this situation also. Indeed, the spectra to analyse, which could also have been obtained experimentally, can be easily fitted by varying freely all the parameters in Eqs.5.12 and assuming a Lorentzian lineshape for both the dark and bright interacting modes. The coupling factors g and v then read $g = \sqrt{\Gamma_P/2\pi}$ and $v = \sqrt{\Gamma_d/2\pi}$. The fitted lineshape (dashed red curve in Fig.5.7a) is the result of the interference between two "original" modes which are normally not directly accessible because they arise during the hybridization process. However, starting with a known profile it is possible to retrieve these modes which are given by the fitted (E_P, Γ_P) and (E_d, Γ_d). The extracted superradiant and subradiant modes are shown as dash red lines in Fig.5.7b and c, respectively. If we now look at a near-field cut at the first peak of Fig.5.7a, it reveals a field distribution that seems to leave out the central particle, see Fig.5.7d. Strikingly, the near-field of this external ring (see inset of Fig.5.7b) is very similar, see Fig.5.7e. This suggests one of the modes is formed by the nanocluster without the central component, as confirmed by observations from Hentschel *et al.* [287] and Lassiter and co-workers [288]. Furthermore, the simulated spectrum of this external ring matches (solid black curve in Fig.5.7b) well with the extracted bright mode (dashed red line). By varying the gaps in the vertical trimer along the polarization axis (see inset of Fig.5.7c and e) from G=5nm (solid black curve in Fig.5.7f) to 7nm (dashed red line) and 10nm (dotted blue curve) shows that the peak at 713nm, which we just identified as the superradiant mode, is not affected at the contrary of the Fano feature at lower energy. It seems sensible then to consider the subradiant state as originating from a mode of strong trimer character. Reporting the simulated spectra of the trimer in Fig.5.7c (solid black line) along the extracted dark state (dashed red curve) is indeed confirming this intuition. Following this analysis, we therefore proposed (see Fig.5.7g) that the extinction of the full heptamer structure (full black curve) is the result of the Fano interference between a superradiant mode originating from the ring resonance (dashed red curve) and a subradiant mode with a strong trimer character (dotted blue curve) [232].

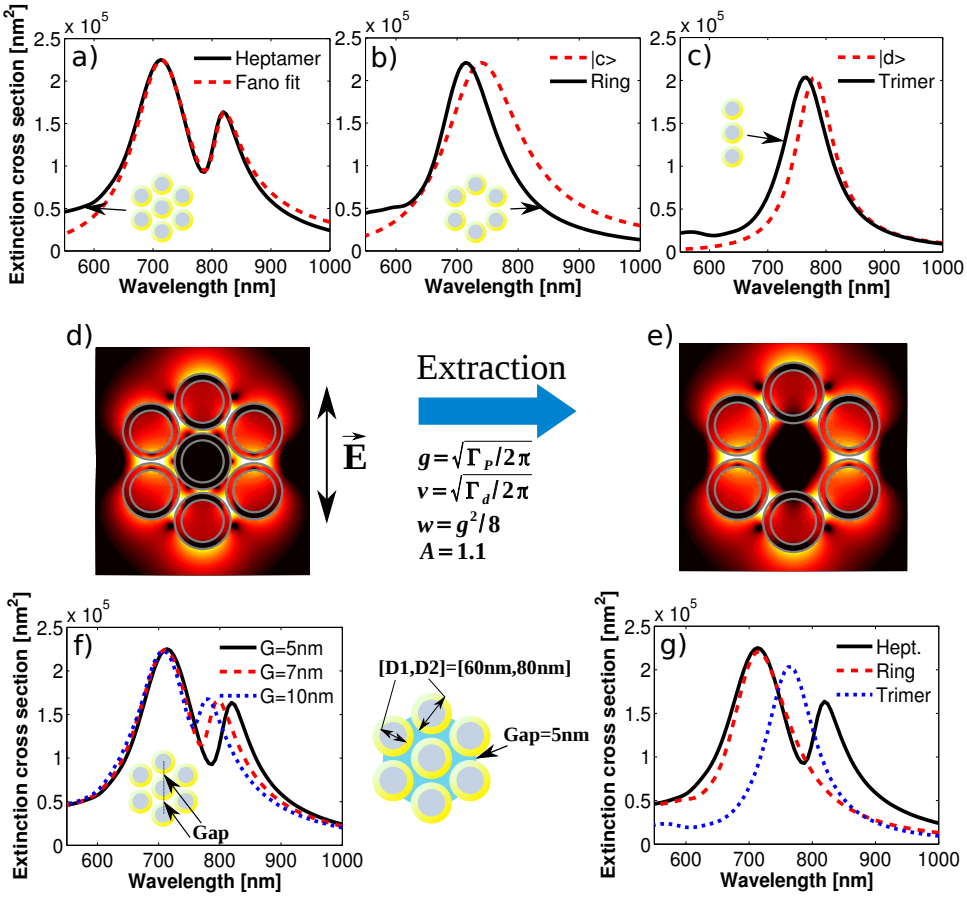

Figure 5.7: a-c) The full black lines are the extinction cross-sections calculated by FDTD of (a) a full heptamer of gold nanoshells, (b) its external ring and (c) the vertical trimer (see respective insets). The dashed red curves represent (a) the fit obtained with the analytic Fano formula $F'(E) = g^2\mathcal{L} \times F(\mathcal{E}) + g^2\mathcal{L} \times A$ with A linked to absorption and its extracted (b) bright $|c\rangle$ and (c) dark $|d\rangle$ modes (for full details see Methods section in [232]). d-e) FDTD near-field cuts at mid-height at 713 nm in log scale of (d) the full heptamer and (e) its external ring. f) FDTD extinction cross-sections of the full heptamer by varying the two gaps G along the vertical trimer axis (polarization direction) from $G = 5$ nm (full black curve) to 7 nm (dashed red line) and 10 nm (dotted blue curve). g) Suggested "original modes" for the heptamer structure (full black line): a bright mode originating from the ring resonance (red dashed curve) and a dark state with a strong trimer character (dotted blue curve, reprinted from [232]).

6. General Conclusions

Throughout this thesis, we have studied the optical properties of structured materials with negative permittivities. We started by reviewing the effects associated with surface polaritons, namely field enhancement and localization, and their condition of existence in different media such as conductors and ionic crystals. We have then discussed the fascinating perspectives which nanophotonics opens up, ranging from sensing and nanocircuitry applications to emerging technologies and devices like plasmon-enhanced photocatalysis, nanolasing, superresolution or electromagnetic cloaks. As we stated, current research is hampered by the losses inherent to electron transport in conductors as well as the intrinsically 2D nature of the available fabrication techniques. It is those two main issues that the work pursued during this thesis was trying to address.

First, we discussed the exciting LSPP resonances in CuS/CuSe octapods grown by our colleagues at IIT. Interestingly, we calculated very strong near-fields for those nanocrystals. They originate, on one hand, from the reduced plasma frequency of the semiconductors, and on another hand, from the numerous tips of the octapods that favour electric field crowding. While still under investigation, these octapods could potentially serve as powerful sensors. We then moved to nanopillars patterned out of thick SiC substrates by Caldwell's group. Within the reststrahlen band of the SiC located in the mid-iR range, localized phonon polariton modes are measured despite not being isolated from the substrate. Calculations further showed the presence of monopole modes among those together with gigantic field enhancement up to four orders of magnitude higher than the excitation power. As the negative permittivity is achieved through the stimulation of optical phonons rather than plasmons, the linewidths observed are also much smaller than for typical plasmonic modes. Experiments to implement those structures for SEIRA are under way as the modes are ideally located in a frequency region rich in molecular vibrations. Finally, as an alternative to metals or classical semiconductors we studied the potentials of graphene, and in particular graphene nanoribbons. We explored the modes supported by sandwiched ribbons and reported on the existence of tightly confined gap modes and anti-bonding waveguide modes. These modes are able to squeeze light in 2 nm-thick dielectric layers or present strong field confinement right at their surfaces. Moreover, by analysing in detail the hybridization mechanism we proposed a simpler geometry in which a single ribbon is placed on top of oxidized conductors like gold or silicon. We also proposed schemes in which these structures could be used for sensing or nanocircuitry applications.

From another perspective, we investigated numerically the optical properties of gold gyroids in a collaboration with Wiesner's group. Those structures represent a new class of materials obtained from the self-assembly of block-copolymers. While measurements on our side were not successful other groups confirmed part of our findings. We predicted for instance that single gyroids would prevent the transmission of low energy light and calculated its rotation power. Double gyroids were shown to exhibit negative

refraction, but in the case of strong absorption, such as due to the interband transitions in gold, this exciting property may disappear.

A significant part of thesis was finally dedicated to the study of Fano resonances after we observed those features in the spectra of SEIRA measurements. This led to the development of an analytical derivation of the original Fano theory by considering the broad plasmonic resonance as the continuum state. The resulting powerful but simple formula allowed us an in depth understanding of the origin of Fano interferences in nanophotonics as we studied SEIRA, EIT, lattice resonances and hybridization.

From our results, it is clear that the successful implementation of nanophotonic concepts into commercial applications can occur through a combination of efficient and large-scale fabrication methods such as self-assembly with low-cost low-loss materials like dielectrics. However, a larger control and better knowledge of those is still in progress.

Bibliography

[1] J. D. Jackson. *Classical Electrodynamics*. John Wiley & Sons, Inc., Hoboken, NJ, 1998.

[2] E. Hecht. *Optics*. Addison Welsey, San Francisco, 2002.

[3] S. A. Maier. *Plasmonics: Fundamentals and applications*. Springer, New York, 2007.

[4] B. Saleh and M. Teich. *Fundamentals of Photonics*. Wiley Series in Pure and Applied Optics. Wiley, 2007.

[5] E. Kapon. *Optics: Course booklet*. EPFL, 2008.

[6] P. W. Atkins and R. S. Friedman. *Molecular quantum mechanics*. Oxford press university, New York, 1997.

[7] E. J. Murphy and S. O. Morgan. *The dielectric properties of insulating materials*. Bell System Technical Journal, 17(4):pp. 640–669, 1938.

[8] M. Fox. *Optical Properties of Solids (Oxford Master Series in Physics)*. Oxford University Press, USA, 1 edition, January 2002.

[9] C. Kittel. *Introduction to solid state physics*. John Wiley & Sons, Inc., New York, 1996.

[10] S. M. Sze. *Physics of semiconductor devices*. Wiley, 2 edition, November 1981.

[11] H. Mutschke, A. C. Andersen, D. Clément, T. Henning and G. Peiter. *Infrared properties of SiC particles*. Astronomy and Astrophysics, 345:pp. 187–202, 1999.

[12] W. L. Barnes, A. Dereux and T. W. Ebbesen. *Surface plasmon subwavelength optics*. Nature, 424(6950):pp. 824–830, August 2003.

[13] A. Otto. *Excitation of nonradiative surface plasma waves in silver by the method of frustrated total reflection*. Zeitschrift für Physik, 216(4):pp. 398–410, 1968.

[14] E. Kretschmann and H. Raether. *Radiative decay of nonradiative surface plasmons excited by light*. Z. Naturforsch. A, 23:p. 2135, 1968.

[15] H. Raether. *Surface Plasmons on Smooth and Rough Surfaces and on Gratings*. Springer-Verlag, Berlin, 1986.

[16] E. Ozbay. *Plasmonics: Merging photonics and electronics at nanoscale dimensions*. Science, 311(5758):pp. 189–193, 2006.

[17] T. W. Ebbesen, C. Genet and S. I. Bozhevolnyi. *Surface-plasmon circuitry.* Physics Today, 61(5):pp. 44–50, 2008.

[18] K. Crozier, A. Sundaramurthy, G. Kino and C. Quate. *Optical antennas: Resonators for local field enhancement.* Journal of Applied Physics, 94(7):pp. 4632–4642, Oct 1 2003.

[19] J. Aizpurua, G. W. Bryant, L. J. Richter, F. J. García de Abajo, B. K. Kelley and T. Mallouk. *Optical properties of coupled metallic nanorods for field-enhanced spectroscopy.* Physical Review B, 71(23):p. 235420, Jun 2005.

[20] V. Myroshnychenko, J. Rodriguez-Fernandez, I. Pastoriza-Santos, A. M. Funston, C. Novo, P. Mulvaney, L. M. Liz-Marzan and F. J. Garcia de Abajo. *Modelling the optical response of gold nanoparticles.* Chemical Society Reviews, 37(9):pp. 1792–1805, Sep 2008.

[21] J. Z. Zhang and C. Noguez. *Plasmonic Optical Properties and Applications of Metal Nanostructures.* Plasmonics, 3(4):pp. 127–150, Dec 2008.

[22] E. Cubukcu, N. Yu, E. J. Smythe, L. Diehl, K. B. Crozier and F. Capasso. *Plasmonic Laser Antennas and Related Devices.* IEEE Journal of Selected Topics in Quantum Electronics, 14(6):pp. 1448–1461, Nov-Dec 2008.

[23] E. S. Barnard, J. S. White, A. Chandran and M. L. Brongersma. *Spectral properties of plasmonic resonator antennas.* Optics Express, 16(21):pp. 16529–16537, OCT 13 2008.

[24] V. Giannini, A. I. Fernández-Domínguez, Y. Sonnefraud, T. Roschuk, R. Fernández-Garciá and S. A. Maier. *Controlling Light Localization and Light-Matter Interactions with Nanoplasmonics.* Small, 6(22):pp. 2498–2507, Nov 22 2010.

[25] K. S. Yee. *Numerical solution of initial boundary value problems involving maxwells equations in isotropic media.* IEEE Transactions on Antennas and Propagation, pp. 302–307, 1966.

[26] J. Zhao, A. O. Pinchuk, J. M. McMahon, S. Li, L. K. Ausman, A. L. Atkinson and G. C. Schatz. *Methods for Describing the Electromagnetic Properties of Silver and Gold Nanoparticles.* Accounts of Chemical Research, 41(12):pp. 1710–1720, December 2008.

[27] J. Parsons, C. Burrows, J. Sambles and W. Barnes. *A comparison of techniques used to simulate the scattering of electromagnetic radiation by metallic nanostructures.* Journal of Modern Optics, 57(5):pp. 356–365, 2010.

[28] H. W. and G. J. *Understanding FT-IR-Data Processing.* CAL, 4-6():pp. 352–425, 1984.

[29] D. Y. Lei, K. Appavoo, Y. Sonnefraud, J. Richard F. Haglund and S. A. Maier. *Single-particle plasmon resonance spectroscopy of phase transition in vanadium dioxide.* Optics Letters, 35(23):pp. 3988–3990, Dec 2010.

[30] K. Kneipp, Y. Wang, H. Kneipp, L. Perelman, I. Itzkan, R. Dasari and M. Feld. *Single molecule detection using surface-enhanced Raman scattering (SERS).* Physical Review Letters, 78(9):pp. 1667–1670, Mar 3 1997.

[31] V. Giannini, A. I. Fernández-Domínguez, S. C. Heck and S. A. Maier. *Plasmonic nanoantennas: Fundamentals and their use in controlling the radiative properties of nanoemitters.* Chemical Reviews, 111(6):pp. 3888–3912, 2011.

[32] J. M. Luther, P. K. Jain, T. Ewers and A. P. Alivisatos. *Localized surface plasmon resonances arising from free carriers in doped quantum dots.* Nature Materials, 10(5):pp. 361–366, 2011.

[33] A. Boltasseva and H. A. Atwater. *Low-Loss Plasmonic Metamaterials.* Science, 331(6015):pp. 290–291, Jan 21 2011.

[34] V. Giannini, A. Berrier, S. M. Maier, J. Antonio Sanchez-Gil and J. G. Rivas. *Scattering efficiency and near field enhancement of active semiconductor plasmonic antennas at terahertz frequencies.* Optics Express, 18(3):pp. 2797–2807, Feb 1 2010.

[35] S. M. Hanham, A. I. Fernández-Domínguez, J. H. Teng, S. S. Ang, K. P. Lim, S. F. Yoon, C. Y. Ngo, N. Klein, J. B. Pendry and S. A. Maier. *Broadband terahertz plasmonic response of touching insb disks.* Advanced Materials, 24(35):pp. OP226–OP230, 2012.

[36] R. Hillenbrand, T. Taubner and F. Keilmann. *Phonon-enhanced light-matter interaction at the nanometre scale.* Nature(London), 418(6894):pp. 159–162, 2002.

[37] R. W. Wood. *On a remarkable case of uneven distribution of light in a diffraction grating spectrum.* Proceedings of the Physical Society of London, 18(1):p. 269, 1902.

[38] R. H. Ritchie. *Plasma losses by fast electrons in thin films.* Physical Review, 106:pp. 874–881, Jun 1957.

[39] S. A. Maier and H. A. Atwater. *Plasmonics: Localization and guiding of electromagnetic energy in metal/dielectric structures.* Journal of Applied Physics, 98(1):011101, 2005.

[40] V. M. Agranovich and D. L. Mills (Editors). *Surface Polaritons: Electromagnetic Waves at Surfaces and Interfaces.* North Holland, 1982.

[41] J. Homola, S. Yee and G. Gauglitz. *Surface plasmon resonance sensors: review.* Sensors and Actuators B-Chemical, 54(1-2):pp. 3–15, Jan 25 1999.

[42] P. Berini. *Long-range surface plasmon polaritons.* Advances in Optics and Photonics, 1(3):pp. 484–588, 2009.

[43] A. Haes, C. Haynes, A. McFarland, G. Schatz, R. Van Duyne and S. Zou. *Plasmonic materials for surface-enhanced sensing and spectroscopy.* MRS Bulletin, 30(5):pp. 368–375, May 2005.

[44] K. A. Willets and R. P. Van Duyne. *Localized surface plasmon resonance spectroscopy and sensing.* Annual Review of Physical Chemistry, 58:pp. 267–297, 2007.

[45] M. Pelton, J. Aizpurua and G. Bryant. *Metal-nanoparticle plasmonics.* Laser & Photonics Reviews, 2(3):pp. 136–159, Jun 2008.

[46] J. N. Anker, W. P. Hall, O. Lyandres, N. C. Shah, J. Zhao and R. P. Van Duyne. *Biosensing with plasmonic nanosensors*. Nature Materials, 7(6):pp. 442–453, Jun 2008.

[47] N. Verellen, Y. Sonnefraud, H. Sobhani, F. Hao, V. V. Moshchalkov, P. V. Dorpe, P. Nordlander and S. A. Maier. *Fano resonances in individual coherent plasmonic nanocavities*. Nano Letters, 9(4):pp. 1663–1667, 2009.

[48] J. A. Fan, K. Bao, C. Wu, J. Bao, R. Bardhan, N. J. Halas, V. N. Manoharan, G. Shvets, P. Nordlander and F. Capasso. *Fano-like Interference in Self-Assembled Plasmonic Quadrumer Clusters*. Nano Letters, 10(11):pp. 4680–4685, Nov 2010.

[49] M. Moskovits. *Surface-enhanced spectroscopy*. Reviews of Modern Physics, 57(3):pp. 783–826, Jul 1985.

[50] M. Moskovits. *Surface-enhanced Raman spectroscopy: a brief retrospective*. Journal of Raman Spectroscopy, 36(6-7):pp. 485–496, Jun-Jul 2005.

[51] M. Osawa. *Surface-enhanced infrared absorption*. In *Near-field optics and surface plasmon polaritons*, volume 81 of *Topics in applied physics*, pp. 163–187. Springer-Verlag, Berlin, 2001.

[52] K. Ataka and J. Heberle. *Biochemical applications of surface-enhanced infrared absorption spectroscopy*. Analytical and Bioanalytical Chemistry, 388(1):pp. 47–54, May 2007.

[53] M. Fleischmann, P. Hendra and A. McQuillan. *Raman spectra of pyridine adsorbed at a silver electrode*. Chemical Physics Letters, 26(2):pp. 163 – 166, 1974.

[54] D. L. Jeanmaire and R. P. V. Duyne. *Surface raman spectroelectrochemistry: Part i. heterocyclic, aromatic, and aliphatic amines adsorbed on the anodized silver electrode*. Journal of Electroanalytical Chemistry, 84(1):pp. 1 – 20, 1977.

[55] M. Albrecht and J. Creighton. *Anomalously intense Raman-spectra of pyridine at a silver electrode*. Journal of The American Chemical Society, 99(15):pp. 5215–5217, 1977.

[56] A. Hartstein, J. Kirtley and J. Tsang. *Enhancement of infrared-absorption from molecular monolayers with thin metal overlayers*. Bulletin of the American Physical Society, 25(3):p. 425, 1980.

[57] V. Giannini, R. Rodríguez-Oliveros and J. Sánchez-Gil. *Surface plasmon resonances of metallic nanostars/nanoflowers for surface-enhanced raman scattering*. Plasmonics, 5:pp. 99–104, 2010.

[58] M. Osawa and M. Ikeda. *Surface-enhanced infrared-absorption of para-nitrobenzoic acid deposited on silver island films - contributions of electromagnetic and chemical mechanisms*. Journal of Physical Chemistry, 95(24):pp. 9914–9919, Nov 28 1991.

[59] G. Lu, S. Sun, S. Chen and L. Cai. *Novel properties of dispersed Pt and Pd thin layers supported on GC for CO adsorption studied using in situ MS-FTIR reflection spectroscopy*. Journal of Electronanalytical Chemistry, 421(1-2):pp. 19–23, Jan 30 1997.

[60] O. Krauth, G. Fahsold and A. Pucci. *Asymmetric line shapes and surface enhanced infrared absorption of CO adsorbed on thin iron films on MgO(001).* Journal of Chemical Physics, 110(6):pp. 3113–3117, Feb 8 1999.

[61] Y. Zhu, H. Uchida and M. Watanabe. *Oxidation of carbon monoxide at a platinum film electrode studied by Fourier transform infrared spectroscopy with attenuated total reflection technique.* Langmuir, 15(25):pp. 8757–8764, Dec 7 1999.

[62] G. Lu, S. Sun, L. Cai, S. Chen, Z. Tian and K. Shiu. *In situ FTIR spectroscopic studies of adsorption of CO, SCN-, and poly(o-phenylenediamine) on electrodes of nanometer thin films of Pt, Pd, and Rh: Abnormal infrared effects (AIREs).* Langmuir, 16(2):pp. 778–786, Jan 25 2000.

[63] D. Enders and A. Pucci. *Surface enhanced infrared absorption of octadecanethiol on wet-chemically prepared Au nanoparticle films.* Applied Physics Letters, 88(18), May 1 2006.

[64] J. Kundu, F. Le, P. Nordlander and N. J. Halas. *Surface enhanced infrared absorption (SEIRA) spectroscopy on nanoshell aggregate substrates.* Chemical Physics Letters, 452(1-3):pp. 115–119, Feb 4 2008.

[65] Y. Nishikawa, K. Fujiwara and T. Shima. *A study on the qualitative and quantitative-analysis of nanogram samples by transmission infrared-spectroscopy with the use of silver island films.* Applied Spectroscopy, 45(5):pp. 747–751, Jun 1991.

[66] R. Bukasov and J. S. Shumaker-Parry. *Silver Nanocrescents with Infrared Plasmonic Properties As Tunable Substrates for Surface Enhanced Infrared Absorption Spectroscopy.* Analytical Chemistry, 81(11):pp. 4531–4535, Jun 1 2009.

[67] F. Neubrech, T. Kolb, R. Lovrincic, G. Fahsold, A. Pucci, J. Aizpurua, T. W. Cornelius, M. E. Toimil-Molares, R. Neumann and S. Karim. *Resonances of individual metal nanowires in the infrared.* Applied Physics Letters, 89:p. 253104, 2006.

[68] F. Neubrech, A. Pucci, T. W. Cornelius, S. Karim, A. Garcia-Etxarri and J. Aizpurua. *Resonant plasmonic and vibrational coupling in a tailored nanoantenna for infrared detection.* Physical Review Letters, 101(15), Oct 2008.

[69] R. Adato, A. A. Yanik, J. J. Amsden, D. L. Kaplan, F. G. Omenetto, M. K. Hong, S. Erramilli and H. Altug. *Ultra-sensitive vibrational spectroscopy of protein monolayers with plasmonic nanoantenna arrays.* Proceedings of the National Academy of Sciences of the United States of America, 106(46):pp. 19227–19232, Nov 17 2009.

[70] J. Aizpurua, T. Taubner, F. J. G. de Abajo, M. Brehm and R. Hillenbrand. *Substrate-enhanced infrared near-field spectroscopy.* Optics Express, 16(3):pp. 1529–1545, 2008.

[71] Z. Fang, Y.-R. Zhen, O. Neumann, A. Polman, F. J. Garca de Abajo, P. Nordlander and N. J. Halas. *Evolution of light-induced vapor generation at a liquid-immersed metallic nanoparticle.* Nano Letters, 13(4):pp. 1736–1742, 2013.

[72] O. Neumann, C. Feronti, A. D. Neumann, A. Dong, K. Schell, B. Lu, E. Kim, M. Quinn, S. Thompson, N. Grady, P. Nordlander, M. Oden and N. J. Halas. *Compact solar autoclave based on steam generation using broadband light-harvesting nanoparticles.* Proceedings of the National Academy of Sciences, 110(29):pp. 11677–11681, 2013.

[73] O. Neumann, A. S. Urban, J. Day, S. Lal, P. Nordlander and N. J. Halas. *Solar vapor generation enabled by nanoparticles.* ACS Nano, 7(1):pp. 42–49, 2013.

[74] D. J. Bergman and M. I. Stockman. *Surface plasmon amplification by stimulated emission of radiation: Quantum generation of coherent surface plasmons in nanosystems.* Physical Review Letters, 90:p. 027402, Jan 2003.

[75] M. A. Noginov, G. Zhu, A. M. Belgrave, R. Bakker, V. M. Shalaev, E. E. Narimanov, S. Stout, E. Herz, T. Suteewong and U. Wiesner. *Demonstration of a Spaser-Based Nanolaser.* Nature, 460(7259):pp. 1110–U68, Aug 27 2009.

[76] S. Mukherjee, F. Libisch, N. Large, O. Neumann, L. V. Brown, J. Cheng, J. B. Lassiter, E. A. Carter, P. Nordlander and N. J. Halas. *Hot electrons do the impossible: Plasmon-induced dissociation of h2 on au.* Nano Letters, 13(1):pp. 240–247, 2013.

[77] P. V. Kamat. *Photophysical, photochemical and photocatalytic aspects of metal nanoparticles.* ChemInform, 33(43):pp. 257–257, 2002.

[78] S. Linic, P. Christopher and D. B. Ingram. *Plasmonic-metal nanostructures for efficient conversion of solar to chemical energy.* Nature Materials, 10(12):pp. 911–921, 2011.

[79] V. P. Zhdanov and B. Kasemo. *Photo-induced chemical processes on metal-semiconductor-metal nanostructures.* Chemical Physics Letters, 524(0):pp. 16 – 19, 2012.

[80] X. Zhang, Y. L. Chen, R.-S. Liu and D. P. Tsai. *Plasmonic photocatalysis.* Reports on Progress in Physics, 76(4):p. 046401, 2013.

[81] H. Li, M. Zanella, A. Genovese, M. Povia, A. Falqui, C. Giannini and L. Manna. *Sequential cation exchange in nanocrystals: Preservation of crystal phase and formation of metastable phases.* Nano Letters, 11(11):pp. 4964–4970, 2011.

[82] K. Miszta, D. Dorfs, A. Genovese, M. R. Kim and L. Manna. *Cation exchange reactions in colloidal branched nanocrystals.* ACS Nano, 5(9):pp. 7176–7183, 2011.

[83] K. Miszta, J. De Graaf, G. Bertoni, D. Dorfs, R. Brescia, S. Marras, L. Ceseracciu, R. Cingolani, R. Van Roij, M. Dijkstra and L. Manna. *Hierarchical self-assembly of suspended branched colloidal nanocrystals into superlattice structures.* Nature Materials, 10(9):pp. 1–5, 2011.

[84] B. Mansour, S. Demian and H. Zayed. *Determination of the effective mass for highly degenerate copper selenide from reflectivity measurements.* Journal of Materials Science: Materials in Electronics, 3(4):pp. 249–252, 1992.

[85] C. M. Hessel, V. P. Pattani, M. Rasch, M. G. Panthani, B. Koo, J. W. Tunnell and B. A. Korgel. *Copper selenide nanocrystals for photothermal therapy.* Nano Letters, 11(6):pp. 2560–2566, 2011.

[86] S.-W. Hsu, K. On and A. R. Tao. *Localized surface plasmon resonances of anisotropic semiconductor nanocrystals.* Journal of the American Chemical Society, 133(47):pp. 19072–19075, 2011.

[87] D. Dorfs, T. Haertling, K. Miszta, N. C. Bigall, M. R. Kim, A. Genovese, A. Falqui, M. Povia and L. Manna. *Reversible tunability of the near-infrared valence band plasmon resonance in $Cu_{2-x}Se$ nanocrystals.* Journal of the American Chemical Society, 133(29):pp. 11175–11180, 2011.

[88] W. Liang and M.-H. Whangbo. *Conductivity anisotropy and structural phase transition in covellite cus.* Solid State Communications, 85(5):pp. 405 – 408, 1993.

[89] J. Le Gall, M. Olivier and J.-J. Greffet. *Experimental and theoretical study of reflection and coherent thermal emissionby a sic grating supporting a surface-phonon polariton.* Physical Review B, 55:pp. 10105–10114, Apr 1997.

[90] J. Greffet, R. Carminati, K. Joulain, J. Mulet, S. Mainguy and Y. Chen. *Coherent emission of light by thermal sources.* Nature, 416(6876):pp. 61–64, Mar 7 2002.

[91] F. Marquier, K. Joulain and J.-J. Greffet. *Resonant infrared transmission through sic films.* Optics Letters, 29(18):pp. 2178–2180, Sep 2004.

[92] N. Ocelic and R. Hillenbrand. *Subwavelength-scale tailoring of surface phonon polaritons by focused ion-beam implantation.* Nature Materials, 3(9):pp. 606–609, Sep 2004.

[93] A. Huber, N. Ocelic, D. Kazantsev and R. Hillenbrand. *Near-field imaging of mid-infrared surface phonon polariton propagation.* Applied Physics Letters, 87(8):081103, 2005.

[94] A. J. Huber, B. Deutsch, L. Novotny and R. Hillenbrand. *Focusing of surface phonon polaritons.* Applied Physics Letters, 92(20):203104, 2008.

[95] T. Taubner, F. Keilmann and R. Hillenbrand. *Nanoscale-resolved subsurface imaging by scattering-type near-field optical microscopy.* Optics Express, 13(22):pp. 8893–8899, Oct 31 2005.

[96] T. Taubner, D. Korobkin, Y. Urzhumov, G. Shvets and R. Hillenbrand. *Near-field microscopy through a SiC superlens.* Science, 313(5793):p. 1595, Sep 15 2006.

[97] D. Korobkin, Y. Urzhumov and G. Shvets. *Enhanced near-field resolution in midinfrared using metamaterials.* Journal of the Optical Society of America B, 23(3):pp. 468–478, Mar 2006.

[98] D. Korobkin, Y. Urzhumov, B. Neuner III, C. Zorman, Z. Zhang, I. Mayergoyz and G. Shvets. *Mid-infrared metamaterial based on perforated sic membrane: engineering optical response using surface phonon polaritons.* Applied Physics A, 88(4):pp. 605–609, 2007.

[99] Y. A. Urzhumov, D. Korobkin, B. N. III, C. Zorman and G. Shvets. *Optical properties of sub-wavelength hole arrays in sic membranes.* Journal of Optics A: Pure and Applied Optics, 9(9):p. S322, 2007.

[100] B. Neuner, C. Wu, G. T. Eyck, M. Sinclair, I. Brener and G. Shvets. *Efficient infrared thermal emitters based on low-albedo polaritonic meta-surfaces.* Applied Physics Letters, 102(21):211111, 2013.

[101] J. A. Schuller, T. Taubner and M. L. Brongersma. *Optical antenna thermal emitters.* Nature Photonics, 3(11):pp. 658–661, Nov 2009.

[102] M. Anderson. *Surface enhanced infrared absorption by coupling phonon and plasma resonance.* Applied physics letters, 87(14), Oct 3 2005.

[103] C. Rockstuhl, M. G. Salt and H. P. Herzig. *Analysis of the phonon-polariton response of silicon carbide microparticles and nanoparticles by use of the boundary element method.* Journal of the Optical Society of America B, 22(2):pp. 481–487, Feb 2005.

[104] J. A. Schuller, R. Zia, T. Taubner and M. L. Brongersma. *Dielectric metamaterials based on electric and magnetic resonances of silicon carbide particles.* Physical Review Letters, 99(10), Sep 7 2007.

[105] T. Wang, P. Li, B. Hauer, D. N. Chigrin and T. Taubner. *Optical properties of single infrared resonant circular microcavities for surface phonon polaritons.* Nano Letters, 13(11):pp. 5051–5055, 2013.

[106] J. D. Caldwell, O. J. Glembocki, Y. Francescato, N. Sharac, V. Giannini, F. J. Bezares, J. P. Long, J. C. Owrutsky, I. Vurgaftman, J. G. Tischler, V. D. Wheeler, N. D. Bassim, L. M. Shirey, R. Kasica and S. A. Maier. *Low-Loss, Extreme Subdiffraction Photon Confinement via Silicon Carbide Localized Surface Phonon Polariton Resonators.* Nano Letters, 13(8):pp. 3690–3697, Aug 2013.

[107] T. Taminiau, F. B. Segerink and N. van Hulst. *A monopole antenna at optical frequencies: Single-molecule near-field measurements.* IEEE Transactions on Antennas and Propagation, 55(11):pp. 3010–3017, 2007.

[108] A. E. Çetin, A. A. Yanik, C. Yilmaz, S. Somu, A. Busnaina and H. Altug. *Monopole antenna arrays for optical trapping, spectroscopy, and sensing.* Applied Physics Letters, 98(11):111110, 2011.

[109] A. K. Geim and K. S. Novoselov. *The rise of graphene.* Nature Materials, 6(3):pp. 183–191, Mar 2007.

[110] A. H. Castro Neto, F. Guinea, N. M. R. Peres, K. S. Novoselov and A. K. Geim. *The electronic properties of graphene.* Review of Modern Physics, 81:pp. 109–162, Jan 2009.

[111] A. K. Geim. *Graphene: Status and prospects.* Science, 324(5934):pp. 1530–1534, 2009.

[112] F. Bonaccorso, Z. Sun, T. Hasan and A. C. Ferrari. *Graphene photonics and optoelectronics.* Nature Photonics, 4(9):pp. 611–622, Sep 2010.

[113] P. Avouris. *Graphene: Electronic and photonic properties and devices.* Nano Letters, 10(11):pp. 4285–4294, 2010.

[114] Q. Bao and K. P. Loh. *Graphene photonics, plasmonics, and broadband optoelectronic devices.* ACS Nano, 6(5):pp. 3677–3694, 2012.

[115] A. N. Grigorenko, M. Polini and K. S. Novoselov. *Graphene plasmonics.* Nature Photonics, 6(11):pp. 749–758, Nov 2012.

[116] H. Liu, Y. Liu and D. Zhu. *Chemical doping of graphene.* Journal of Materials Chemistry, 21:pp. 3335–3345, 2011.

[117] F. Wang, Y. Zhang, C. Tian, C. Girit, A. Zettl, M. Crommie and Y. R. Shen. *Gate-variable optical transitions in graphene.* Science, 320(5873):pp. 206–209, Apr 11 2008.

[118] Z. Q. Li, E. A. Henriksen, Z. Jiang, Z. Hao, M. C. Martin, P. Kim, H. L. Stormer and D. N. Basov. *Dirac charge dynamics in graphene by infrared spectroscopy.* Nature Physics, 4(7):pp. 532–535, Jul 2008.

[119] L. Ju, B. Geng, J. Horng, C. Girit, M. Martin, Z. Hao, H. A. Bechtel, X. Liang, A. Zettl, Y. R. Shen and F. Wang. *Graphene plasmonics for tunable terahertz metamaterials.* Nature Nanotechnology, 6(10):pp. 630–634, Oct 2011.

[120] Z. Fei, A. S. Rodin, G. O. Andreev, W. Bao, A. S. McLeod, M. Wagner, L. M. Zhang, Z. Zhao, M. Thiemens, G. Dominguez, M. M. Fogler, A. H. C. Neto, C. N. Lau, F. Keilmann and D. N. Basov. *Gate-tuning of graphene plasmons revealed by infrared nano-imaging.* Nature, 487(7405):pp. 82–85, Jul 5 2012.

[121] J. Chen, M. Badioli, P. Alonso-Gonzalez, S. Thongrattanasiri, F. Huth, J. Osmond, M. Spasenovic, A. Centeno, A. Pesquera, P. Godignon, A. Zurutuza Elorza, N. Camara, F. Javier García de Abajo, R. Hillenbrand and F. H. L. Koppens. *Optical nano-imaging of gate-tunable graphene plasmons.* Nature, 487(7405):pp. 77–81, Jul 5 2012.

[122] C.-F. Chen, C.-H. Park, B. W. Boudouris, J. Horng, B. Geng, C. Girit, A. Zettl, M. F. Crommie, R. A. Segalman, S. G. Louie and F. Wang. *Controlling inelastic light scattering quantum pathways in graphene.* Nature, 471(7340):pp. 617–620, Mar 31 2011.

[123] V. P. Gusynin, S. G. Sharapov and J. P. Carbotte. *Magneto-optical conductivity in graphene.* Journal of Physics: Condensed Matter, 19(2):p. 026222, 2007.

[124] A. Vakil and N. Engheta. *Transformation optics using graphene.* Science, 332(6035):pp. 1291–1294, 2011.

[125] A. Y. Nikitin, F. Guinea, F. J. García-Vidal and L. Martín-Moreno. *Fields radiated by a nanoemitter in a graphene sheet.* Physical Review B, 84:p. 195446.

[126] L. A. Falkovsky and S. S. Pershoguba. *Optical far-infrared properties of a graphene monolayer and multilayer.* Physical Review B, 76:p. 153410, Oct 2007.

[127] Y. Francescato, V. Giannini and S. A. Maier. *Strongly confined gap plasmon modes in graphene sandwiches and graphene-on-silicon.* New Journal of Physics, 15, Jun 14 2013.

[128] R. R. Nair, P. Blake, A. N. Grigorenko, K. S. Novoselov, T. J. Booth, T. Stauber, N. M. R. Peres and A. K. Geim. *Fine structure constant defines visual transparency of graphene.* Science, 320(5881):p. 1308, 2008.

[129] K. F. Mak, M. Y. Sfeir, Y. Wu, C. H. Lui, J. A. Misewich and T. F. Heinz. *Measurement of the optical conductivity of graphene.* Physical Review Letters, 101:p. 196405, Nov 2008.

[130] S. A. Mikhailov and K. Ziegler. *New electromagnetic mode in graphene.* Phys. Rev. Lett., 99:p. 016803, Jul 2007.

[131] W. Gao, J. Shu, C. Qiu and Q. Xu. *Excitation of plasmonic waves in graphene by guided-mode resonances.* ACS Nano, 6(9):pp. 7806–7813, 2012.

[132] A. Manjavacas, P. Nordlander and F. J. García de Abajo. *Plasmon blockade in nanostructured graphene.* ACS Nano, 6(2):pp. 1724–1731, 2012.

[133] P. Li and T. Taubner. *Broadband subwavelength imaging using a tunable graphene-lens.* ACS Nano, 6(11):pp. 10107–10114, 2012.

[134] H. Yan, F. Xia, Z. Li and P. Avouris. *Plasmonics of coupled graphene micro-structures.* New Journal of Physics, 14(12):p. 125001, 2012.

[135] R. Alaee, M. Farhat, C. Rockstuhl and F. Lederer. *A perfect absorber made of a graphene micro-ribbon metamaterial.* Optics Express, 20(27):pp. 28017–28024, Dec 2012.

[136] A. Fallahi and J. Perruisseau-Carrier. *Design of tunable biperiodic graphene metasurfaces.* Physical Reveview B, 86:p. 195408.

[137] I. Crassee, M. Orlita, M. Potemski, A. L. Walter, M. Ostler, T. Seyller, I. Gaponenko, J. Chen and A. B. Kuzmenko. *Intrinsic terahertz plasmons and magnetoplasmons in large scale monolayer graphene.* Nano Letters, 12(5):pp. 2470–2474, 2012.

[138] H. Yan, Z. Li, X. Li, W. Zhu, P. Avouris and F. Xia. *Infrared spectroscopy of tunable dirac terahertz magneto-plasmons in graphene.* Nano Letters, 12(7):pp. 3766–3771, 2012.

[139] W. Wang, S. P. Apell and J. M. Kinaret. *Edge magnetoplasmons and the optical excitations in graphene disks.* Physical Review B, 86:p. 125450.

[140] B. Wang, X. Zhang, F. J. García-Vidal, X. Yuan and J. Teng. *Strong coupling of surface plasmon polaritons in monolayer graphene sheet arrays.* Physical Review Letters, 109:p. 073901.

[141] P. Liu, W. Cai, L. Wang, X. Zhang and J. Xu. *Tunable terahertz optical antennas based on graphene ring structures.* Applied Physics Letters, 100(15):153111, 2012.

[142] B. Wang, X. Zhang, X. Yuan and J. Teng. *Optical coupling of surface plasmons between graphene sheets.* Applied Physics Letters, 100(13):131111, 2012.

[143] Z. Fang, S. Thongrattanasiri, A. Schlather, Z. Liu, L. Ma, Y. Wang, P. M. Ajayan, P. Nordlander, N. J. Halas and F. J. Garcia de Abajo. *Gated tunability and hybridization of localized plasmons in nanostructured graphene.* ACS Nano, 7(3):pp. 2388–2395, 2013.

[144] W. B. Lu, W. Zhu, H. J. Xu, Z. H. Ni, Z. G. Dong and T. J. Cui. *Flexible transformation plasmonics using graphene.* Optics Express, 21(9):pp. 10475–10482, May 2013.

[145] N. Liu, S. Mukherjee, K. Bao, L. V. Brown, J. Dorfmller, P. Nordlander and N. J. Halas. *Magnetic plasmon formation and propagation in artificial aromatic molecules.* Nano Letters, 12(1):pp. 364–369, 2012.

[146] Z. Fang, Y. Wang, Z. Liu, A. Schlather, P. M. Ajayan, F. H. L. Koppens, P. Nordlander and N. J. Halas. *Plasmon-induced doping of graphene.* ACS Nano, 6(11):pp. 10222–10228, 2012.

[147] Z. Fang, Z. Liu, Y. Wang, P. M. Ajayan, P. Nordlander and N. J. Halas. *Graphene-antenna sandwich photodetector.* Nano Letters, 12(7):pp. 3808–3813, 2012.

[148] N. Papasimakis, Z. Luo, Z. X. Shen, F. D. Angelis, E. D. Fabrizio, A. E. Nikolaenko and N. I. Zheludev. *Graphene in a photonic metamaterial.* Optics Express, 18(8):pp. 8353–8359, Apr 2010.

[149] Y. Zou, P. Tassin, T. Koschny and C. M. Soukoulis. *Interaction between graphene and metamaterials: split rings vs. wire pairs.* Optics Express, 20(11):pp. 12198–12204, May 2012.

[150] M. Jablan, H. Buljan and M. Soljačić. *Plasmonics in graphene at infrared frequencies.* Physical Review B, 80:p. 245435.

[151] Z. Fei, G. O. Andreev, W. Bao, L. M. Zhang, A. S. McLeod, C. Wang, M. K. Stewart, Z. Zhao, G. Dominguez, M. Thiemens, M. M. Fogler, M. J. Tauber, A. H. Castro-Neto, C. N. Lau, F. Keilmann and D. N. Basov. *Infrared nanoscopy of dirac plasmons at the graphene-sio2 interface.* Nano Letters, 11(11):pp. 4701–4705, 2011.

[152] W. Zhou, J. Lee, J. Nanda, S. T. Pantelides, S. J. Pennycook and J.-C. Idrobo. *Atomically localized plasmon enhancement in monolayer graphene.* Nature Nanotechnology, 7(3):pp. 161–165, Mar 2012.

[153] F. H. L. Koppens, D. E. Chang and F. J. García de Abajo. *Graphene plasmonics: A platform for strong light-matter interactions.* Nano Letters, 11(8):pp. 3370–3377, 2011.

[154] P. Tassin, T. Koschny and C. M. Soukoulis. *Graphene for terahertz applications.* Science, 341(6146):pp. 620–621, 2013.

[155] A. Y. Nikitin, F. Guinea, F. J. García-Vidal and L. Martín-Moreno. *Edge and waveguide terahertz surface plasmon modes in graphene microribbons.* Physical Review B, 84:p. 161407.

[156] J. Christensen, A. Manjavacas, S. Thongrattanasiri, F. H. L. Koppens and F. J. García de Abajo. *Graphene plasmon waveguiding and hybridization in individual and paired nanoribbons.* ACS Nano, 6(1):pp. 431–440, 2012.

[157] R. Zia, M. D. Selker and M. L. Brongersma. *Leaky and bound modes of surface plasmon waveguides.* Physical Review B, 71:p. 165431.

[158] *Handbook of Optical-Constants.* Journal of the Optical Society of America A-Optics Image Science and Vision, 1(12):p. 1297, 1984.

[159] W. Spitzer and H. Y. Fan. *Infrared absorption in n-type silicon.* Physical Review, 108:pp. 268–271, Oct 1957.

[160] A. Das, S. Pisana, B. Chakraborty, S. Piscanec, S. K. Saha, U. V. Waghmare, K. S. Novoselov, H. R. Krishnamurthy, A. K. Geim, A. C. Ferrari and A. K. Sood. *Monitoring dopants by Raman scattering in an electrochemically top-gated graphene transistor.* Nature Nanotechnology, 3(4):pp. 210–215, Apr 2008.

[161] P. Venezuela, M. Lazzeri and F. Mauri. *Theory of double-resonant raman spectra in graphene: Intensity and line shape of defect-induced and two-phonon bands.* Physical Review B, 84:p. 035433, Jul 2011.

[162] R. Wang, S. Wang, D. Zhang, Z. Li, Y. Fang and X. Qiu. *Control of carrier type and density in exfoliated graphene by interface engineering.* ACS Nano, 5(1):pp. 408–412, 2011.

[163] Y. Xiao, Y. Francescato, V. Giannini, M. Rahmani, T. R. Roschuk, A. M. Gilbertson, Y. Sonnefraud, C. Mattevi, M. Hong, L. F. Cohen and S. A. Maier. *Probing the dielectric response of graphene via dual-band plasmonic nanoresonators.* Physical Chemistry Chemical Physics, 15(15):pp. 5395–5399, 2013.

[164] J. Niu, Y. Jun Shin, Y. Lee, J.-H. Ahn and H. Yang. *Graphene induced tunability of the surface plasmon resonance.* Applied Physics Letters, 100(6):061116, 2012.

[165] N. K. Emani, T.-F. Chung, X. Ni, A. V. Kildishev, Y. P. Chen and A. Boltasseva. *Electrically tunable damping of plasmonic resonances with graphene.* Nano Letters, 12(10):pp. 5202–5206, 2012.

[166] J. Kim, H. Son, D. J. Cho, B. Geng, W. Regan, S. Shi, K. Kim, A. Zettl, Y.-R. Shen and F. Wang. *Electrical control of optical plasmon resonance with graphene.* Nano Letters, 12(11):pp. 5598–5602, 2012.

[167] Y. Yao, M. A. Kats, P. Genevet, N. Yu, Y. Song, J. Kong and F. Capasso. *Broad electrical tuning of graphene-loaded plasmonic antennas.* Nano Letters, 13(3):pp. 1257–1264, 2013.

[168] S. H. Mousavi, I. Kholmanov, K. B. Alici, D. Purtseladze, N. Arju, K. Tatar, D. Y. Fozdar, J. W. Suk, Y. Hao, A. B. Khanikaev, R. S. Ruoff and G. Shvets. *Inductive tuning of fano-resonant metasurfaces using plasmonic response of graphene in the mid-infrared.* Nano Letters, 13(3):pp. 1111–1117, 2013.

[169] V. M. Shalaev. *Optical negative-index metamaterials.* Nature Photonics, 1(1):pp. 41–48, Jan 2007.

[170] V. G. Veselago. *The electrodynamics of substances with simultaneously negative values of ε and μ.* Soviet Physics Uspekhi, 10(4):p. 509, 1968.

[171] J. Pendry. *Negative refraction makes a perfect lens.* Physical Review Letters, 85(18):pp. 3966–3969, Oct 30 2000.

[172] J. Pendry, D. Schurig and D. Smith. *Controlling electromagnetic fields.* Science, 312(5781):pp. 1780–1782, Jun 23 2006.

[173] V. M. Shalaev. *Transforming light.* Science, 322(5900):pp. 384–386, Oct 17 2008.

[174] J. B. Pendry, A. J. Holden, W. J. Stewart and I. Youngs. *Extremely low frequency plasmons in metallic mesostructures.* Physical Review Letters, 76(25):pp. 4773–4776, Jun 1996.

[175] J. Pendry, A. Holden, D. Robbins and W. Stewart. *Magnetism from conductors and enhanced nonlinear phenomena.* IEEE Transactions on Microwave Theory and Techniques, 47(11):pp. 2075–2084, Nov 1999.

[176] D. R. Smith, W. J. Padilla, D. C. Vier, S. C. Nemat-Nasser and S. Schultz. *Composite medium with simultaneously negative permeability and permittivity.* Physical Review Letters, 84(18):pp. 4184–4187, May 2000.

[177] R. Shelby, D. Smith and S. Schultz. *Experimental verification of a negative index of refraction.* Science, 292(5514):pp. 77–79, Apr 6 2001.

[178] T. Yen, W. Padilla, N. Fang, D. Vier, D. Smith, J. Pendry, D. Basov and X. Zhang. *Terahertz magnetic response from artificial materials.* Science, 303(5663):pp. 1494–1496, Mar 5 2004.

[179] S. Linden, C. Enkrich, M. Wegener, J. Zhou, T. Koschny and C. Soukoulis. *Magnetic response of metamaterials at 100 terahertz.* Science, 306(5700):pp. 1351–1353, Nov 19 2004.

[180] C. M. Soukoulis, S. Linden and M. Wegener. *Negative refractive index at optical wavelengths.* Science, 315(5808):pp. 47–49, Jan 5 2007.

[181] J. Zhou, T. Koschny, M. Kafesaki, E. Economou, J. Pendry and C. Soukoulis. *Saturation of the magnetic response of split-ring resonators at optical frequencies.* Physical Review Letters, 95(22), Nov 25 2005.

[182] S. Zhang, W. Fan, N. Panoiu, K. Malloy, R. Osgood and S. Brueck. *Experimental demonstration of near-infrared negative-index metamaterials.* Physical review letters, 95(13), Sep 23 2005.

[183] G. Dolling, C. Enkrich, M. Wegener, C. Soukoulis and S. Linden. *Simultaneous negative phase and group velocity of light in a metamaterial.* Science, 312(5775):pp. 892–894, May 12 2006.

[184] S. Xiao, U. K. Chettiar, A. V. Kildishev, V. P. Drachev and V. M. Shalaev. *Yellow-light negative-index metamaterials.* Optics Letters, 34(22):pp. 3478–3480, Nov 15 2009.

[185] N. Liu, H. Guo, L. Fu, S. Kaiser, H. Schweizer and H. Giessen. *Three-dimensional photonic metamaterials at optical frequencies.* Nature Materials, 7(1):pp. 31–37, Jan 2008.

[186] J. Valentine, S. Zhang, T. Zentgraf, E. Ulin-Avila, D. A. Genov, G. Bartal and X. Zhang. *Three-dimensional optical metamaterial with a negative refractive index.* Nature, 455(7211):pp. 376–U32, Sep 18 2008.

[187] J. Yao, Z. Liu, Y. Liu, Y. Wang, C. Sun, G. Bartal, A. M. Stacy and X. Zhang. *Optical negative refraction in bulk metamaterials of nanowires.* Science, 321(5891):p. 930, Aug 15 2008.

[188] J. K. Gansel, M. Thiel, M. S. Rill, M. Decker, K. Bade, V. Saile, G. von Freymann, S. Linden and M. Wegener. *Gold Helix Photonic Metamaterial as Broadband Circular Polarizer.* Science, 325(5947):pp. 1513–1515, Sep 18 2009.

[189] D. O. Gueney, T. Koschny, M. Kafesaki and C. A. Soukoulis. *Connected bulk negative index photonic metamaterials.* Optics Letters, 34(4):pp. 506–508, Feb 15 2009.

[190] D. Smith, J. Pendry and M. Wiltshire. *Metamaterials and negative refractive index.* Science, 305(5685):pp. 788–792, Aug 6 2004.

[191] Y. Liu and X. Zhang. *Metamaterials: a new frontier of science and technology.* Chemical Society Reviews, 40(5):pp. 2494–2507, 2011.

[192] T. A. Klar, A. V. Kildishev, V. P. Drachev and V. M. Shalaev. *Negative-index metamaterials: Going optical.* IEEE Journal of Selected Topics in Quantum Electronics, 12(6, Part 1):pp. 1106–1115, Nov-Dec 2006.

[193] J. Pendry. *Negative refraction.* Contemporary Physics, 45(3):pp. 191–202, May-Jun 2004.

[194] S. A. Ramakrishna. *Physics of negative refractive index materials.* Reports on Progress in Physics, 68(2):p. 449, 2005.

[195] M. W. McCall. *What is negative refraction?* Journal of Modern Optics, 56(16):pp. 1727–1740, 2009.

[196] S. A. Ramakrishna and T. M. Grzegorczyk. *Physics and Applications of Negative Refractive Index Materials.* Bellingham, Wash, London, 2009.

[197] X. Zhang and Z. Liu. *Superlenses to overcome the diffraction limit.* Nature Materials, 7(6):pp. 435–441, Jun 2008.

[198] U. Leonhardt. *Optical conformal mapping.* Science, 312(5781):pp. 1777–1780, 2006.

[199] B. Wood. *Structure and properties of electromagnetic metamaterials.* Laser & Photonics Reviews, 1(3):pp. 249–259, 2007.

[200] K. L. Tsakmakidis, A. D. Boardman and O. Hess. *'Trapped rainbow' storage of light in metamaterials.* Nature, 450(7168):pp. 397–401, Nov 15 2007.

[201] C. M. Soukoulis and M. Wegener. *Optical Metamaterials-More Bulky and Less Lossy.* Science, 330(6011):pp. 1633–1634, Dec 17 2010.

[202] S. A. Ramakrishna and J. B. Pendry. *Removal of absorption and increase in resolution in a near-field lens via optical gain.* Physical Review B, 67(20), May 15 2003.

[203] H. J. Lezec, J. A. Dionne and H. A. Atwater. *Negative refraction at visible frequencies.* Science, 316(5823):pp. 430–432, Apr 20 2007.

[204] E. Verhagen, R. de Waele, L. Kuipers and A. Polman. *Three-Dimensional Negative Index of Refraction at Optical Frequencies by Coupling Plasmonic Waveguides.* Physical Review Letters, 105(22), Nov 23 2010.

[205] S. P. Burgos, R. de Waele, A. Polman and H. A. Atwater. *A single-layer wide-angle negative-index metamaterial at visible frequencies.* Nature Materials, 9(5):pp. 407–412, May 2010.

[206] A. J. Hoffman, L. Alekseyev, S. S. Howard, K. J. Franz, D. Wasserman, V. A. Podolskiy, E. E. Narimanov, D. L. Sivco and C. Gmachl. *Negative refraction in semiconductor metamaterials.* Nature Materials, 6(12):pp. 946–950, Dec 2007.

[207] A. Fang, T. Koschny and C. M. Soukoulis. *Optical anisotropic metamaterials: Negative refraction and focusing.* Physical Review B, 79(24):p. 245127, Jun 2009.

[208] S. Tretyakov, I. Nefedov, A. Sihvola, S. Maslovski and C. Simovski. *Waves and energy in chiral nihility.* Journal of Electromagnetic Waves and Applications, 17(5):pp. 695–706, 2003.

[209] J. Pendry. *A chiral route to negative refraction.* Science, 306(5700):pp. 1353–1355, Nov 19 2004.

[210] J. Zhou, J. Dong, B. Wang, T. Koschny, M. Kafesaki and C. M. Soukoulis. *Negative refractive index due to chirality.* Physical Review B, 79(12):p. 121104, Mar 2009.

[211] B. Wang, J. Zhou, T. Koschny, M. Kafesaki and C. M. Soukoulis. *Chiral metamaterials: simulations and experiments.* Journal of Optics A-Pure and Applied Optics, 11(11), Nov 2009. 1st International Workshop on Theoretical and Computational Nano-Photonics, Bad Honnef, Germany, DEC 03-05, 2008.

[212] P. R. West, S. Ishii, G. V. Naik, N. K. Emani, V. M. Shalaev and A. Boltasseva. *Searching for better plasmonic materials.* Laser & Photonics Reviews, 4(6):pp. 795–808, Nov 2010.

[213] K. Hur, Y. Francescato, V. Giannini, S. A. Maier, R. G. Hennig and U. Wiesner. *Three-dimensionally isotropic negative refractive index materials from block copolymer self-assembled chiral gyroid networks.* Angewandte Chemie International Edition, 50(50):pp. 11985–11989, 2011.

[214] M. Maldovan, A. Urbas, N. Yufa, W. Carter and E. Thomas. *Photonic properties of bicontinuous cubic microphases.* Physical Review B, 65(16), Apr 15 2002.

[215] K. Michielsen and D. G. Stavenga. *Gyroid cuticular structures in butterfly wing scales: biological photonic crystals.* Journal of the Royal Society Interface, 5(18):pp. 85–94, Jan 6 2008.

[216] V. Saranathan, C. O. Osuji, S. G. J. Mochrie, H. Noh, S. Narayanan, A. Sandy, E. R. Dufresne and R. O. Prum. *Structure, function, and self-assembly of single network gyroid (I4(1)32) photonic crystals in butterfly wing scales.* Proceedings of the National Academy of Sciences of the United States of America, 107(26):pp. 11676–11681, Jun 29 2010.

[217] M. Saba, M. Thiel, M. D. Turner, S. T. Hyde, M. Gu, K. Grosse-Brauckmann, D. N. Neshev, K. Mecke and G. E. Schroeder-Turk. *Circular Dichroism in Biological Photonic Crystals and Cubic Chiral Nets.* Physical Review Letters, 106(10), Mar 11 2011.

[218] A. Raman and S. Fan. *Photonic band structure of dispersive metamaterials formulated as a hermitian eigenvalue problem.* Physical Review Letters, 104(8):p. 087401, Feb 2010.

[219] S. Vignolini, N. A. Yufa, P. S. Cunha, S. Guldin, I. Rushkin, M. Stefik, K. Hur, U. Wiesner, J. J. Baumberg and U. Steiner. *A 3d optical metamaterial made by self-assembly.* Advanced Materials, 24(10):pp. OP23–OP27, 2012.

[220] S. Salvatore, A. Demetriadou, S. Vignolini, S. S. Oh, S. Wuestner, N. A. Yufa, M. Stefik, U. Wiesner, J. J. Baumberg, O. Hess and U. Steiner. *Tunable 3d extended self-assembled gold metamaterials with enhanced light transmission.* Advanced Materials, 25(19):pp. 2713–2716, 2013.

[221] E. Majorana. *I presunti termini anomali dell'elio.* Nuovo Cimento, 8(1):pp. 78–83, 1931.

[222] E. Majorana. *Teoria dei triplettip? incompleti.* Nuovo Cimento, 8(1):pp. 107–113, 1931.

[223] U. Fano. *Sullo spettro di assorbimento dei gas nobili presso il limite dello spettro d'arco.* Nuovo Cimento, 12(3):pp. 154–161, 1935.

[224] U. Fano. *Effects of configuration interaction on intensities and phase shifts.* Physical Review, 124(6):pp. 1866–1878, Dec 1961.

[225] S. Bandopadhyay, B. Dutta-Roy and H. S. Mani. *Understanding the fano resonance through toy models.* American Journal of Physics, 72(12):pp. 1501–1507, 2004.

[226] A. Rau. *Perspectives on the Fano resonance formula.* Physica Scripta, 69(1):pp. C10–C13, Jan 2004.

[227] A. Miroshnichenko, S. Flach and Y. Kivshar. *Fano resonances in nanoscale structures.* Reviews of Modern Physics, 82(3):pp. 2257–2298, Aug 2010.

[228] B. Luk'yanchuk, N. I. Zheludev, S. A. Maier, N. J. Halas, P. Nordlander, H. Giessen and C. T. Chong. *The Fano resonance in plasmonic nanostructures and metamaterials.* Nature Materials, 9(9):pp. 707–715, Sep 2010.

[229] V. Giannini, Y. Francescato, H. Amrania, C. C. Phillips and S. A. Maier. *Fano resonances in nanoscale plasmonic systems: A parameter-free modeling approach.* Nano Letters, 11(7):pp. 2835–2840, Jul 2011.

[230] B. Gallinet and O. J. F. Martin. *Ab initio theory of fano resonances in plasmonic nanostructures and metamaterials.* Physical Review B, 83:p. 235427, Jun 2011.

[231] B. Gallinet and O. J. F. Martin. *Influence of electromagnetic interactions on the line shape of plasmonic fano resonances.* ACS Nano, 5(11):pp. 8999–9008, 2011.

[232] Y. Francescato, V. Giannini and S. A. Maier. *Plasmonic systems unveiled by fano resonances.* ACS Nano, 6(2):pp. 1830–1838, 2012.

[233] A. Artar, A. A. Yanik and H. Altug. *Multispectral plasmon induced transparency in coupled meta-atoms.* Nano Letters, 11(4):pp. 1685–1689, 2011.

[234] A. Manjavacas, F. J. G. d. Abajo and P. Nordlander. *Quantum plexcitonics: Strongly interacting plasmons and excitons.* Nano Letters, 11(6):pp. 2318–2323, 2011.

[235] M. Shapiro. *Electromagnetically induced transparency with structured multicontinua.* Physical Review A, 75:p. 013424, Jan 2007.

[236] E. Bortchagovsky and U. Fischer. *On the modulation of optical transmission spectra of thin dye layers by a supporting medium.* Journal Of Chemical Physics, 117(11):pp. 5384–5392, Sep 15 2002.

[237] N. Liu, L. Langguth, T. Weiss, J. Kaestel, M. Fleischhauer, T. Pfau and H. Giessen. *Plasmonic analogue of electromagnetically induced transparency at the Drude damping limit.* Nature Materials, 8(9):pp. 758–762, Sep 2009.

[238] E. Prodan, C. Radloff, N. Halas and P. Nordlander. *A hybridization model for the plasmon response of complex nanostructures.* Science, 302(5644):pp. 419–422, Oct 17 2003.

[239] A. Christ, Y. Ekinci, H. H. Solak, N. A. Gippius, S. G. Tikhodeev and O. J. F. Martin. *Controlling the Fano interference in a plasmonic lattice.* Physical Review B, 76(20), Nov 2007.

[240] N. A. Mirin, K. Bao and P. Nordlander. *Fano Resonances in Plasmonic Nanoparticle Aggregates.* Journal of Physical Chemistry A, 113(16):pp. 4028–4034, Apr 23 2009.

[241] J. A. Fan, C. Wu, K. Bao, J. Bao, R. Bardhan, N. J. Halas, V. N. Manoharan, P. Nordlander, G. Shvets and F. Capasso. *Self-Assembled Plasmonic Nanoparticle Clusters.* Science, 328(5982):pp. 1135–1138, May 28 2010.

[242] S. Mukherjee, H. Sobhani, J. B. Lassiter, R. Bardhan, P. Nordlander and N. J. Halas. *Fanoshells: Nanoparticles with Built-in Fano Resonances.* Nano Letters, 10(7):pp. 2694–2701, Jul 2010.

[243] J. B. Lassiter, H. Sobhani, J. A. Fan, J. Kundu, F. Capasso, P. Nordlander and N. J. Halas. *Fano resonances in plasmonic nanoclusters: Geometrical and chemical tunability.* Nano Letters, 10(8):pp. 3184–3189, 2010.

[244] C. P. Burrows and W. L. Barnes. *Large spectral extinction due to overlap of dipolar and quadrupolar plasmonic modes of metallic nanoparticles in arrays.* Optics Express, 18(3):pp. 3187–3198, Feb 1 2010.

[245] K. Aydin, I. M. Pryce and H. A. Atwater. *Symmetry breaking and strong coupling in planar optical metamaterials.* Optics Express, 18(13):pp. 13407–13417, Jun 21 2010.

[246] T. W. Ebbesen, H. J. Lezec, H. F. Ghaemi, T. Thio and P. A. Wolff. *Extraordinary optical transmission through sub-wavelength hole arrays.* Nature, 391(6668):pp. 667–669, Feb 12 1998.

[247] H. F. Ghaemi, T. Thio, D. E. Grupp, T. W. Ebbesen and H. J. Lezec. *Surface plasmons enhance optical transmission through subwavelength holes.* Physical Review B, 58(11):pp. 6779–6782, Sep 15 1998.

[248] C. Genet, M. van Exter and J. Woerdman. *Fano-type interpretation of red shifts and red tails in hole array transmission spectra.* Optics Communications, 225(4-6):pp. 331–336, Oct 1 2003.

[249] A. Christ, T. Zentgraf, S. G. Tikhodeev, N. A. Gippius, O. J. F. Martin, J. Kuhl and H. Giessen. *Interaction between localized and delocalized surface plasmon polariton modes in a metallic photonic crystal.* Physica Status Solidi B-Basic Solid State Physics, 243(10):pp. 2344–2348, Aug 2006. 8th International Workshop on Nonlinear Optics and Excitation Kinetics In Semiconductors (NOEKS 8), Munster, Germany, Feb 20-24, 2006.

[250] S. Zou, N. Janel and G. Schatz. *Silver nanoparticle array structures that produce remarkably narrow plasmon lineshapes.* Journal of Chemical Physics, 120(23):pp. 10871–10875, Jun 15 2004.

[251] S. Zou and G. Schatz. *Silver nanoparticle array structures that produce giant enhancements in electromagnetic fields.* Chemical Physics Letters, 403(1-3):pp. 62–67, Feb 14 2005.

[252] B. Auguie and W. L. Barnes. *Collective resonances in gold nanoparticle arrays.* Physical Review Letters, 101(14), Oct 3 2008.

[253] S. H. Fan. *Sharp asymmetric line shapes in side-coupled waveguide-cavity systems.* Applied Physics Letters, 80(6):pp. 908–910, Feb 11 2002.

[254] A. Christ, S. Tikhodeev, N. Gippius, J. Kuhl and H. Giessen. *Waveguide-plasmon polaritons: Strong coupling of photonic and electronic resonances in a metallic photonic crystal slab.* Physical Review Letters, 91(18), Oct 31 2003.

[255] A. Christ, T. Zentgraf, J. Kuhl, S. Tikhodeev, N. Gippius and H. Giessen. *Optical properties of planar metallic photonic crystal structures: Experiment and theory.* Physical Review B, 70(12), Sep 2004.

[256] F. Neubrech, D. Weber, D. Enders, T. Nagao and A. Pucci. *Antenna Sensing of Surface Phonon Polaritons.* Journal of Physical Chemistry C, 114(16):pp. 7299–7301, Apr 29 2010.

[257] N. Gippius, S. Tikhodeev and T. Ishihara. *Optical properties of photonic crystal slabs with an asymmetrical unit cell.* Physical Review B, 72(4), Jul 2005.

[258] L. Sherry, S. Chang, G. Schatz, R. Van Duyne, B. Wiley and Y. Xia. *Localized surface plasmon resonance spectroscopy of single silver nanocubes.* Nano Letters, 5(10):pp. 2034–2038, Oct 2005.

[259] F. Hao, Y. Sonnefraud, P. V. Dorpe, S. A. Maier, N. J. Halas and P. Nordlander. *Symmetry breaking in plasmonic nanocavities: Subradiant lspr sensing and a tunable fano resonance.* Nano Letters, 8(11):pp. 3983–3988, 2008.

[260] M. W. Knight, Y. Wu, J. B. Lassiter, P. Nordlander and N. J. Halas. *Substrates Matter: Influence of an Adjacent Dielectric on an Individual Plasmonic Nanoparticle.* Nano Letters, 9(5):pp. 2188–2192, May 2009.

[261] I. M. Pryce, K. Aydin, Y. A. Kelaita, R. M. Briggs and H. A. Atwater. *Highly Strained Compliant Optical Metamaterials with Large Frequency Tunability.* Nano Letters, 10(10):pp. 4222–4227, Oct 2010.

[262] S. Zhang, K. Bao, N. J. Halas, H. Xu and P. Nordlander. *Substrate-Induced Fano Resonances of a Plasmonic: Nanocube: A Route to Increased-Sensitivity Localized Surface Plasmon Resonance Sensors Revealed.* Nano Letters, 11(4):pp. 1657–1663, Apr 2011.

[263] S. Zhang, D. A. Genov, Y. Wang, M. Liu and X. Zhang. *Plasmon-induced transparency in metamaterials.* Physical Review Letters, 101(4):p. 047401, Jul 2008.

[264] N. Liu, T. Weiss, M. Mesch, L. Langguth, U. Eigenthaler, M. Hirscher, C. Soennichsen and H. Giessen. *Planar Metamaterial Analogue of Electromagnetically Induced Transparency for Plasmonic Sensing.* Nano Letters, 10(4):pp. 1103–1107, Apr 2010.

[265] H. Xu, Y. Lu, Y. Lee and B. S. Ham. *Studies of electromagnetically induced transparency in metamaterials.* Optics Express, 18(17):pp. 17736–17747, Aug 16 2010.

[266] C. Alzar, M. Martinez and P. Nussenzveig. *Classical analog of electromagnetically induced transparency.* American Journal of Physics, 70(1):pp. 37–41, Jan 2002.

[267] M. Fleischhauer, A. Imamoglu and J. Marangos. *Electromagnetically induced transparency: Optics in coherent media.* Reviews of Modern Physics, 77(2):pp. 633–673, Apr 2005.

[268] M. Klein, T. Tritschler, M. Wegener and S. Linden. *Lineshape of harmonic generation by metallic nanoparticles and metallic photonic crystal slabs.* Physical Review B, 72(11), Sep 2005.

[269] S. Fan, W. Suh and J. Joannopoulos. *Temporal coupled-mode theory for the Fano resonance in optical resonators.* Journal of the Optical Society of America A-Optics, Image Science and Vision, 20(3):pp. 569–572, Mar 2003.

[270] M. Tomita, K. Totsuka, R. Hanamura and T. Matsumoto. *Tunable Fano interference effect in coupled-microsphere resonator-induced transparency.* Journal of the Optical Society of America B-Optical Physics, 26(4):pp. 813–818, Apr 2009.

[271] Y. Xu, Y. Li, R. K. Lee and A. Yariv. *Scattering-theory analysis of waveguide-resonator coupling.* Physical Review E, 62(5, Part B):pp. 7389–7404, Nov 2000.

[272] A. E. Miroshnichenko. *Instabilities and quasi-localized states in nonlinear Fano-like systems.* Physics Letters A, 373(39):pp. 3586–3590, Sep 21 2009.

[273] F. Hao, P. Nordlander, Y. Sonnefraud, P. V. Dorpe and S. A. Maier. *Tunability of subradiant dipolar and fano-type plasmon resonances in metallic ring/disk cavities: Implications for nanoscale optical sensing.* ACS Nano, 3(3):pp. 643–652, 2009.

[274] Y. Sonnefraud, N. Verellen, H. Sobhani, G. A. Vandenbosch, V. V. Moshchalkov, P. Van Dorpe, P. Nordlander and S. A. Maier. *Experimental realization of subradiant, superradiant, and fano resonances in ring/disk plasmonic nanocavities.* ACS Nano, 4(3):pp. 1664–1670, 2010.

[275] C. Cohen-Tannoudji, J. Dupont-Roc and G. Grynberg. *Atom-Photon Interactions: Basic Processes and Applications.* Wiley-VCH Verlag GmbH & Co. KGaA, Weinheim, 2004.

[276] J. A. Hutchison, D. M. O'Carroll, T. Schwartz, C. Genet and T. W. Ebbesen. *Absorption-Induced Transparency.* Angewandte Chemie-International Edition, 50(9):pp. 2085–2089, 2011.

[277] F. J. G. de Abajo. *Colloquium: Light scattering by particle and hole arrays.* Reviews of Modern Physics, 79(4):pp. 1267–1290, Oct-Dec 2007.

[278] G. Vecchi, V. Giannini and J. G. Rivas. *Surface modes in plasmonic crystals induced by diffractive coupling of nanoantennas.* Physical Review B, 80(20), Nov 2009.

[279] G. Vecchi, V. Giannini and J. G. Rivas. *Shaping the Fluorescent Emission by Lattice Resonances in Plasmonic Crystals of Nanoantennas.* Physical Review Letters, 102(14), Apr 10 2009.

[280] V. Giannini, G. Vecchi and J. G. Rivas. *Lighting Up Multipolar Surface Plasmon Polaritons by Collective Resonances in Arrays of Nanoantennas.* Physical Review Letters, 105(26), Dec 20 2010.

[281] W. Zhou and T. W. Odom. *Tunable subradiant lattice plasmons by out-of-plane dipolar interactions.* Nature Nanotechnology, 6(7):pp. 423–427, Jul 2011.

[282] Z.-J. Yang, Z.-S. Zhang, L.-H. Zhang, Q.-Q. Li, Z.-H. Hao and Q.-Q. Wang. *Fano resonances in dipole-quadrupole plasmon coupling nanorod dimers.* Optics Letters, 36(9):pp. 1542–1544, May 2011.

[283] N. J. Halas, S. Lal, W.-S. Chang, S. Link and P. Nordlander. *Plasmons in Strongly Coupled Metallic Nanostructures.* Chemical Reviews, 111(6, SI):pp. 3913–3961, Jun 2011.

[284] M. Hentschel, M. Saliba, R. Vogelgesang, H. Giessen, A. P. Alivisatos and N. Liu. *Transition from isolated to collective modes in plasmonic oligomers.* Nano Letters, 10(7):pp. 2721–2726, 2010.

[285] D. Dregely, M. Hentschel and H. Giessen. *Excitation and tuning of higher-order fano resonances in plasmonic oligomer clusters.* ACS Nano, 5(10):pp. 8202–8211, 2011.

[286] P. Alonso-Gonzalez, M. Schnell, P. Sarriugarte, H. Sobhani, C. Wu, N. Arju, A. Khanikaev, F. Golmar, P. Albella, L. Arzubiaga, F. Casanova, L. E. Hueso, P. Nordlander, G. Shvets and R. Hillenbrand. *Real-space mapping of fano interference in plasmonic metamolecules.* Nano Letters, 11(9):pp. 3922–3926, 2011.

[287] M. Hentschel, D. Dregely, R. Vogelgesang, H. Giessen and N. Liu. *Plasmonic oligomers: The role of individual particles in collective behavior.* ACS Nano, 5(3):pp. 2042–2050, 2011.

[288] J. B. Lassiter, H. Sobhani, M. W. Knight, W. S. Mielczarek, P. Nordlander and N. J. Halas. *Designing and deconstructing the fano lineshape in plasmonic nanoclusters.* Nano Letters, 12(2):pp. 1058–1062, 2012.